Title
Development of Functional Materials with Nanoscale Architectures for Applications in Energy Storage and Energy Conservation

Author
Yan, Yan

Publication Date
2018

Peer reviewed|Thesis/dissertation

UNIVERSITY OF CALIFORNIA

Los Angeles

Development of Functional Materials with Nanoscale Architectures for Applications in Energy Storage and Energy Conservation

A dissertation submitted in partial satisfaction of the

requirements for the degree Doctor of Philosophy

in Chemistry

by

Yan Yan

2018

ABSTRACT OF THE DISSERTATION

Development of Functional Materials with Nanoscale Architectures

for Applications in Energy Storage and Energy Conservation

by

Yan Yan

Doctor of Philosophy in Chemistry

University of California, Los Angeles, 2018

Professor Sarah H. Tolbert, Chair

Developing novel functional materials for applications in energy storage and conservation is essential to solving today's problems of meeting growing energy demands with minimal environmental impact. The first part of this dissertation describes pseudocapacitive Li-ion electrodes for fast charge storage. Pseudocapacitance, a charge-transfer process that is not diffusion-limited by definition, can be achieved by utilizing short diffusion lengths in nanostructures. In this section, three distinct transitional metal oxides with nanoscale architecture, Nb_2O_5, MoO_2, and $LiMn_2O_4$, are examined. We focus on correlating charge storage mechanisms with structural properties, and exploring different aspects of pseudocapacitive charge storage with each system. First, we developed a core/shell Nb_2O_5/Nb_4N_5 composite via partial nitridation, achieving specific capacity over 500 C/g within 90 seconds. Our use of the nitride shell provides

excellent electronic pathways that connect Nb_2O_5 nanoparticles and improve the interfacial electrical conductivity. The charge storage mechanism was found to depend on the thickness of the nitride shell. For MoO_2, we developed an interconnected porous network that provides facile electrical and ionic pathways for fast charge storage. We also used it as a model system to understand the effects of structural variations on charge storage behavior. Phase transition suppression was found to be associated with highly capacitive systems, and a strong correlation between charge storage properties and crystallite size was established. Last, we developed needle-like nanostructures with selectively engineered surface facets to overcome its capacity loss due to surface Mn dissolution. This unique structure allowed for a higher capacity and less surface Mn dissolution due to a dominant presence of dissolution-resistant facets.

The second part of this dissertation studies thermal transport in mesoporous SiO_2. SiO_2 is widely used in many thermal insulating applications due to its facile synthesis and easy-to-control of structure. Porous amorphous SiO_2 has strong boundary scattering effects that lead to significantly low thermal conductivity. In this section, we examined the effect of porosity, pore size, and framework texture (i.e., continuous or nanoparticulate) on thermal conductivity in mesoporous SiO_2 thin films. Sol-gel and nanoparticle-based mesoporous SiO_2 thin films were synthesized by evaporation-induced self-assembly using tetraethyl orthosilicate and pre-made SiO_2 nanoparticles as the framework precursors, respectively, and a variety of template reagents. The thermal conductivity was measured by time-domain thermoreflectance at room temperature in vacuum. A porosity weighted simple effective medium approximation was employed to explain trends in thermal conductivity. The results give new insight into thermal transport in nanostructured amorphous materials, and suggest design rules of the nanoscale architecture to control the thermal conductivity of mesoporous materials for a wide range of applications.

The dissertation of Yan Yan is approved.

Alexander Michael Spokoyny

Bruce S. Dunn

Sarah H. Tolbert, Committee Chair

University of California, Los Angeles

2018

To my family

TABLE OF CONTENTS

LIST OF FIGURES

Chapter 2. Core/shell Nb_2O_5/Nb_4N_5-rGO Composites as a Novel High Rate Li-ion Pseudocapacitive Material

Chapter 4 Tuning the Porous Structure in PMMA Templated Mesoporous MoO_2 for Pseudocapacitive Li-ion Electrodes

Chapter 7. Effect of Pore Size on Thermal Conductivity in Nanoparticle and Sol-gel Based mesoporous SiO_2 Films

LIST OF TABLES

LIST OF SCHEMES

ACKNOWLEDGEMENTS

Five years ago, I embarked on this journey to pursue a PhD in materials chemistry out of pure passion for science. Little did I know what an arduous and exciting adventure it would become. This work would not have been possible without tremendous support from many amazing people. First, I must thank my advisor, Professor Sarah Tolbert. I am grateful for her guidance, support and encouragement during the last five years. I appreciate all the brainstorming, trouble shooting, or just simple personal chatting time with her given how busy she is. I learned from her not only essential scientific knowledge and technical skills, but also important life lessons and career advice. She will always be my role model as a strong female professional. I would also like to thank my committee members for their guidance and advice: Professor Xiangfeng Duan, Professor Alex Spokoyny and Professor Bruce Dunn. I would like to additionally thank Professor Yung-Ya Lin as he continuously provided me with great advice ever since I first arrived at UCLA through the CSST program.

Today's science problems are so complicated that they often require many different skills and knowledge sets. I could not have completed all my projects without the contribution from my collaborators. I would like to thank Dr. John Cook, Dr. Eric Detsi, Dr. Ben Lesel and Terri Lin from the Tolbert Lab as well as Dr. Chun-hai (Matt) Lai, Dr. Hyung-Seok (Jimmy) Kim, Dr. Jesse Ko and Jonathan Lau from the Dunn lab for guidance and help in electrochemical techniques and measurements, data analysis and extensive discussions. I would like to thank Dr. Michal Marszewski, Tiphaine Galy from the Pilon Lab and Man Li, Joon Sang Kang from the Hu Lab for optical and thermal measurement in the insulating SiO_2 films projects. Thanks to Dr. Shauna Robbennolt who took some awesome TEM images for several of the projects involved in this thesis, and was always ready to help with any question about nanocrystal synthesis. Thanks to

Sophia King who helped to make a lot of samples and did structural measurement and analysis for porous SiO_2 films. In the Materials Instrumentation Center (MIC) I would like to thank Dr. Ignacio Martinez for help with SEM, XPS and DSC, and Dr. Saeed Khan for help with XRD. I would also like to acknowledge Professor Yongjie Hu, Professor Laurent Pilon, and Professor Bruce Dunn for their advice and guidance on the projects we have collaborated on and reviewing several of my manuscripts.

I would also like to thank the past and present members of the Tolbert Lab for various interesting and useful conversation, life advice, and exciting group events, including: Stephen Sasaki, Patrick Yee, Jialin Lei, Ty Karaba, Terri Lin, Erick Harr, K.J. Winchell, Tori Basile, Andrew Dawson, Yiyi Yao, Sophia King, Jeff Kurish, Shanlin Hu, Yutong Wu, Joe Mazzetti, Shreya Patel, Justin Ondry, Daisy Robinson, Dr. Iris Rauda, Dr. Jesse Hierso, Dr. Rachel Huber, Dr. Amy Ferreira, Dr. Laura Schelhas, Dr. Abraham Buditama, Dr. Shauna Robbennolt, Dr. Robert Thompson, Dr. Benjamin Lesel, Dr. Hyeyeon Kang, Dr. Eric Detsi, Dr. John Cook and Dr. Sabrina Fischer. I had the privilege to learn from some awesome senior members in the group. Dr. John Cook taught me everything I need to know as a first year- from synthesis to characterization, from how to seek collaboration to how to write a manuscript. Dr. Laura Saldarriaga taught me how to use ellipsometeric porosimetry, and cheered me up a lot during my undergrad and first year with her passion and dancing. Dr. Jessie Hierso taught me PMMA synthesis. I also had the pleasure to work with some outstanding undergraduate researchers: Sooji Hong, Yongjiang Liu, Mengshan Ye, Vivian Wall and Matthew Chin. They offered a fresh eye to old and new research projects, and inspired me to become a good mentor and leader.

Last but not the least, I would like to thank my loving family for their endless support. They were my first and best teachers. My dad, an analytical chemist back then, sparkled my interest in

science by performing “magic” with pH indicator solutions and acid-base reactions. My mom cultivated my interest in English by having English tutoring groups hosted in our living room every Sunday. Overall, it was thanks to them that I got exposed to libraries and sophisticated equipment as a child. More importantly, I learned from my parents about dedication, independence, self-learning and persistence. Although we have been parted by the Pacific Ocean for the last five years, I know they always have my back and I love them very much. I would also like to thank my second family, the Lesels. Hanging out every Friday night with great food, movies and board games have become a wonderful routine away from the stress of graduate school. I am so fortunate to have a mushy family to turn to whenever I need help and support. Special thanks goes to my best friend, colleague, and husband, Dr. Ben Lesel. We met during graduate school, and have developed a strong bond through collaborating and hanging out. I cannot imagine a better partner who is always there when I need him, who understands my struggles and my nerdy jokes, and who shares many interests and takes on adventures with me. I appreciate how we supported each other through the last four years, and I look forward to our next chapters in life together.

Previous Publications and Contributions of Co-Authors

Chapter 2 is a version of Yan Yan, Chun-Han Lai, Shauna Robbennolt, Bruce Dunn, Sarah H. Tolbert, "Core/shell Nb_2O_5/Nb_4N_5-rGO Composites as a Novel High Rate Li-ion Pseudocapacitive Material." Chun-Han did electrochemical measurements. Shauna did TEM. I wrote the manuscript and Chun-Han, Professor Dunn, and Professor Tolbert helped edit. This manuscript will be submitted for publication shortly after this dissertation is filed.

Chapter 3 is a version of Yan Yan, Hyung-Seok Kim, John B. Cook, Shauna Robbennolt, Bruce Dunn, Sarah H. Tolbert, "Mesoporous MoO_2 thin films for pseudocapacitive Li^+ storage: Effect of Crystallinity and Porous Structure." Hyung-seok did the electrochemical measurements. John helped with initial synthesis and characterization. Shauna helped with the TEM. I wrote the manuscript, Hyung-Seok and Professor Tolbert helped edit. This manuscript will be submitted for publication shortly after this dissertation is filed.

Chapter 4 is a version of Yan Yan, Matthew A. Chin, Benjamin K. Lesel, Bruce Dunn, Sarah H. Tolbert, "Tuning the Porous Structure in PMMA Templated Mesoporous MoO_2 for Pseudocapacitive Li-ion Electrode." Matthew helped with materials synthesis and electrochemical measurements, and data processing. Benjamin helped with some kinetic analysis. I wrote the manuscript and Matthew and Ben helped edit. This manuscript will be submitted for publication shortly after this dissertation is filed.

Chapter 5 is a version of Benjamin K. Lesel, Yan Yan, Nathaniel Szeto, Jiaming Chen, Shauna Robbennolt and Sarah H. Tolbert, "Increasing the Capacity of Nano-Structured $LiMn_2O_4$ by Selective Crystallization of Dissolution Resistant Surface Sites." I synthesized the PMMA colloids as the template and performed electrochemical tests. Nathaniel Szeto and Jiaming Chen synthesized the nanostructured $LiMn_2O_4$ materials. Shauna Robbennolt helped with transition

electron microscopy (TEM) measurements. Ben and I wrote the manuscript and Professor Tolbert helped edit. This manuscript will be submitted for publication shortly after this dissertation is filed.

Chapter 6 is a version of Yan Yan, Man Li, Sophia King, Tiphaine Galy, Michal Marszewski, Joon Sang Kang, Laurent Pilon, Yongjie Hu, Sarah H. Tolbert, "Exploring the Effect of Porous Structure on Thermal Conductivity of Mesoporous SiO_2 Films." Man and Joon performed thermal conductivity measurements. Sophia helped with synthesis of the films, small angle X-ray scattering measurements and TEM. Tiphaine measured the porosity using UV-vis reflectance spectroscopy. I wrote the manuscript and Man, Sophia, Tiphaine, Michal, Professor Pilon, Professor Hu and Professor Tolbert helped edit. This manuscript will be submitted for publication shortly after this dissertation is filed.

Chapter 7 is a version of Yan Yan, Man Li, Sophia King, Tiphaine Galy, Laurent Pilon, Yongjie Hu, Sarah H. Tolbert, "Effect of Pore Size on Thermal Conductivity in Nanoparticle and Sol-gel Based mesoporous SiO_2 Films." Man performed thermal conductivity measurements. Sophia helped with synthesis of the films, small angle X-ray scattering measurements and TEM. Tiphaine measured the porosity using UV-vis reflectance spectroscopy. I wrote the manuscript and Man, Sophia, Tiphaine, Professor Pilon and Professor Tolbert helped edit. This manuscript will be submitted for publication shortly after this dissertation is filed.

The research presented in this dissertation was directed by Professor Sarah H. Tolbert and was supported by: U.S. Department of Energy (DOE), Office of Science, Basic Energy Sciences; DOE, Advanced Research Projects Agency-Energy (ARPA-E); California NanoSystems Institute (CNSI); University of California, Los Angeles Graduate Division; and Chinese Scholar Council (CSC). Much of the diffraction data presented here was collected at the Stanford Synchrotron Radiation Lightsource, a national user facility operated by Stanford University on behalf of the

U.S. Department of Energy, Office of Basic Science. All of the TEM images presented here were collected using instruments at the Electron Imaging Center for NanoMachines supported by NIH (1S10RR23057 to ZHZ) and CNSI at UCLA.

VITA

2010-2011	Xiyuan Fellow, Fudan's Undergraduate Research Opportunities Program (FDUROP), Fudan University
2011	Exchange Abroad Program, University of California, Santa Barbara
2012	Cross-disciplinary Scholars in Science and Technology (CSST) Program, UCLA
2012-2013	Wangdao Fellow, FDUROP, Fudan University
2012	Outstanding Model Student of Fudan University
2013	Bachelors of Science in Materials Chemistry, Fudan University
2014	Master of Science in Chemistry, UCLA
2013-2015	Chinese Scholar Council Fellowship
2014-2017	Student leader, CSST Program, UCLA
2015-2018	Teaching Assistant, Department of Chemistry, UCLA
2015-2018	High School Nanoscience Outreach Program, UCLA
2015-2018	Electrochemical Society (ECS) Student Chapter board member, UCLA
2016-2017	Chemistry and Biochemistry Graduate Student Association (CBGSA), Administrative Chair, board member, UCLA
2017	American Chemical Society Travel Award, UCLA
2017-2018	Tech Fellow, UCLA Technology Development Group

PUBLICATIONS AND PRESENTATIONS

1. Eric Detsi, Xavier Petrissans, **Yan Yan**, John Cook, Ziling Deng, Yu-Lun Liang, Bruce Dunn, Sarah Tolbert. Tuning Ligament Shape in Dealloyed Nanoporous Tin and the Impact of Nanoscale Morphology on Its Applications in Na-Ion Alloy Battery Anodes. *Phys. Rev. Materials.* 2: 055404 (2018)

2. Benjamin Lesel, John Cook, **Yan Yan**, Terri Lin, Sarah Tolbert. Using Nanoscale Domain Size to Control Charge Storage Kinetics in Pseudocapacitive Nanoporous $LiMn_2O_4$ Powders. *ACS Energy Lett.* 2 (10): 2293-2298 (2017)

3. John Cook, Hyung-Seok Kim, **Yan Yan**, Jesse Ko, Bruce Dunn, Sarah Tolbert. Mesoporous MoS_2 as a transition metal dichalcogenide exhibiting pseudocapacitive Li and Na-ion charge storage. *Adv. Energy Mater.* 6: 1501937 (2016)

4. Justin C. Ondry, Shauna Robbennolt, Hyeyeon Kang, **Yan Yan**, and Sarah H. Tolbert. "A Room Temperature, Solution Phase Method for the Synthesis of Mesoporous Metal Chalcogenide Nanocrystal Based Thin Films with Precisely Controlled Grain Sizes" *Chem. Mater.* 28, 6105-6117 (2016)

5. Hao Chen, Linfeng Hu, Min Chen, **Yan Yan**, Limin Wu. Nickel–Cobalt Layered Double Hydroxide Nanosheets for High-performance Supercapacitor Electrode Materials. *Adv. Functional Mater.* 24(7), 934-942 (2014)

6. Hao Chen, Linfeng Hu, **Yan Yan**, Renchao Che, Min Chen, Limin Wu. One-Step Fabrication of Ultrathin Porous Nickel Hydroxide-Manganese Dioxide Hybrid Nanosheets for Supercapacitor Electrodes with Excellent Capacitive Performance. *Adv. Energy Mater.* 3(12), 1636-1646 (2013)

7. "Exploring the Effect of Nanoscale Architecture on Thermal Conductivity of Nanoporous SiO_2 Films" poster and oral presentation at the 10th International Mesoporous Materials Symposium, Los Angeles, CA, September 2018

8. "Increasing the Capacity of Nanostructured $LiMn_2O_4$ by Selective Crystallization of Dissolution Resistant Surface Sites" Oral presentation at the 233rd Electrochemical Society meeting, Seattle, WA, May 2018

9. **"**Core/shell Nb_2O_5/Nb_4N_5-rGO Composites as a Novel High Power Li-ion Pseudocapacitive Anode Material" Oral and Poster presentation at the 253rd American Chemical Society meeting, San Francisco, CA, April 2017

10. **"**Nb_4N_5/Nb_2O_5/r-GO Composites As Anode Materials for High Power Lithium Ion Batteries" Oral presentation at the 229th ECS meeting, San Diego, CA, May 2016

CHAPTER 1

Introduction

The demand for sustainable and clean energy sources has been growing rapidly. Increasing environmental concerns, raised from the consumption of fossil fuels and the expansion of the world population, and the mushrooming interest in portable electronics, hybrid vehicles, and smart homes have driven the development of advanced energy storage and conservation materials and devices. The primary aim of this work is to develop and characterize novel nanostructured materials for application in (1) high power Li-ion pseudocapacitive electrodes and (2) thermally insulating films. A fundamental understanding of correlations between structures and properties are sought in these systems. This work demonstrates various methods of incorporating novel architectures into traditional materials to achieve new properties and better performance, as well as serve as a platform to understand the underlying chemistry.

In the first part of this dissertation (Chapters 2-5), electrode materials for pseudocapacitive energy storage, which have the potential for next-generation energy storage devices, are discussed. Currently, Li-ion batteries in electric vehicles are hindered by long charging times. These limitations largely derive from the active electrode materials. Pseudocapacitive materials have emerging as a new type of high power density energy storage material by bridging the gap between traditional Li-ion batteries and electrical double layer capacitors.[1–3] On one hand, batteries offer high energy density by utilizing reversible redox reactions, but their long Li^+ solid-state diffusion lengths result in long charging times.[4] On the other hand, electrical double layer capacitors offer high power density via non-faradaic adsorption/desorption at the electrode/electrolyte interface,

but since no redox reactions are involved, the energy density is low.[5] Pseudocapacitive materials combine the advantages of both charging mechanisms by reducing Li^+ diffusion lengths while maintaining energy densities similar to those achieved by redox-based charge storage.[6–8]

In literature, the term pseudocapacitance primarily refers to surface redox processes; however, intercalation reactions at the "near surface" that are not diffusion-limited can also be defined as pseudocapacitive. Surface pseudocapacitance relies largely on high surface area, which is not always easy to achieve. The thermal process required for crystallization makes the formation of very small nanocrystals in certain materials extremely difficult. However, "near surface" intercalation pseudocapacitance can be developed in most traditional battery materials through nanostructuring. The fundamental difference between surface and intercalation pseudocapacitance is that intercalaction pseudocapacitance has deeper ion penetration into the active material while realizing capacitor-like behaviors. This ion penetration depth, or critical size under which a material displays pseudocapacitance, is highly dependent on material composition and morphology. For example, when the particle size of TiO_2 nanoparticles is reduced from 30nm to 7nm, the capacitive contribution to the total charge increases from 15% to 55%.[9] However, another material, Nb_2O_5 nanoscrystals, showed >80% pseudoapacitive charge at 40 nm.[10,11] In order for pseudocapacitance to occur, several conditions must exist in the electrode: (1) good electrical conductivity throughout the electrode, (2) short ion diffusion lengths, and (3) no phase changes upon Li insertion and deinsertion.

Incorporating porous nanostructure into conventional electrode materials is one of the easiest ways to satisfy these conditions. Nanostructures boast high surface area and small particle size, allowing for ample charge storage sites, short ion-diffusion pathways, and good electrolyte accessibility, which are crucial to fast charge storage. They also provide flexible structures to

accommodate any volume change accompanying cycling, allowing for a long cycle life. The aim of this section is to study how nanoscale architecture is related to pseudocapacitive energy storage mechanisms and electrochemical performance. Solution-phase routes offer precise control and tunability of the desired nanostructures and the compositions, which are used to synthesize the electrode materials in the following chapters. The following three nanostructured metal oxide systems explore different aspects of pseudocapacitive charge storage with regard to their synthetic parameters.

Chapter 2 aims to improve the power density of a pseudocapacitive material Nb_2O_5 by designing a core/shell oxide/nitride structure. Nb_2O_5 is a well-studied pseudocapacitive material that exhibits fast intercalation/deintercalation kinetics due to the facile two-dimensional Li^+ transport pathways within the structure of its orthorhombic phase.[10–13]. However, its high-rate performance is hindered by low electrical conductivity. We explored a novel architecture - an oxide/nitride core/shell composite with the oxide providing pseudocapacitance and the nitride acting as a conductive network. The composite was prepared via hydrothermal synthesis followed by high temperature nitridation. The nitride shell thickness is controlled by varying the nitridation time. We conducted electrochemical tests with thin film electrodes to understand the fundamental charging mechanism and found that the charging behaviors of the composite change as a function of nitride thickness. A nitride shell with an optimal thickness allows fast kinetics without blocking Li^+ intercalation. As the nitride content increases, the charging mechanism is gradually dominated by electrical double layer capacitance with the nitride layer blocking Li^+ intercalation into Nb_2O_5. The best electrochemical performance was achieved in Nb_2O_5(81%)/Nb_4N_5(19%)-rGO and is attributed to the enhanced electrical conductivity from the Nb_4N_5 and the excellent interfacial contact between the oxide and the nitride. Good charging performance is achieved in optimized

slurry electrodes, with more than 500 C/g being charged within 90 seconds. The results indicate that metal oxide/metal nitride composites could provide a new design element for high power pseudocapacitive electrode materials.

Chapters 3 and 4 focus on developing pseudocapacitive behaviors in MoO_2 via incorporation of porous structure. Unlike Nb_2O_5, MoO_2 has good metallic conductivity, which makes it a promising fast charging material. Our previous work identified MoO_2 as an extrinsic pseudocapacitor material, with phase change suppression observed in 15 nm nanosized-MoO_2.[14] However, its kinetics was still not ideal compared to other pseudocapacitive materials, with only 50 mAh/g delivered at 20C and only 43% capacitive contribution to the total charge. The main reason is that MoO_2 is prone to surface oxidation, and the product, MoO_3, is electrically insulating. In this work, we avoid sluggish electrical conductivity due to the presence of MoO_3 by utilizing mesoporous nanostructures where electroactive MoO_2 grains are interconnected through a three-dimensional network, thus maintaining good electrical conductivity. We examined porous MoO_2 in two forms: thin films templated by block copolymer (Chapter 3) and powder templated by PMMA colloids (Chapter 4). Quantitative kinetic analyses were performed to understand the size dependencies of the charge storage mechanisms. Ex-situ X-ray diffraction experiments were used to find the critical size for pseudocapacitance based on phase change suppression.

In Chapter 5, we switch our focus from anode materials to cathode materials. While much progress has been made in anode materials, research on fast-charging cathodes is still scarce. This is due to the high temperature typically required to crystallize most cathode materials.[15,16] Previous research[17,18] as shown that Li_2MnO_4 is easy to nanostructure and that nanostructured Li_2MnO_4 displays excellent kinetics; however, the capacity of the nanosized Li_2MnO_4 is much lower than that of the bulk material due to the inactive surface. As the size decreases and the surface becomes

more dominating, the capacity lowers.[18] Additional capacity loss arose from surface manganese dissolution.[19-21] Here, we aimed to develop a method to improve the capacity of nano Li_2MnO_4 through selective facets engineering. we designed $LiMn_2O_4$ with different nanostructures: round-LMO (R-LMO) and needle-like LMO (N-LMO) using two different precursors, acetate and nitrate salts, respectively. We studied the effect of surface structure on the electrochemical performance and found that N-LMO displayed higher capacity than R-LMO despite similar kinetics. Unlike the R-LMO, which showed no surface preferences, N-LMO was found to have preferential (111) surface facets, which have been shown to be more resistant to surface manganese dissolution. XPS study on the Li counter electrodes also corroborated the less manganese dissolution in the case of N-LMO. This study provides exciting insights into the understanding of how surface structure affects electrochemical properties of nanostructured $LiMn_2O_4$ systems and presents a design rule for controlling morphology.

The second part of this dissertation focuses on understanding thermal transport properties in mesoporous SiO_2 films and developing SiO_2-based thermally insulating materials. Various applications of nanostructured materials in heat transfer and insulation fields[22–26] have made it essential to understand thermal transport at the nanoscale. Porous amorphous SiO_2 has attracted a lot of attention due to the strong boundary scattering effects, which leads to significantly reduced thermal conductivity.[27–30] Previous studies have shown that porous structures effectively decrease thermal conductivity in thin films, but most of these studies only focused on SiO_2 aerogels or sol-gel networks and sampled a limited range of pore sizes.[31–34] A thorough understanding of structural effects on thermal conductivity in porous amorphous materials remains underdeveloped. We aim to explore the effects of porous structure on thermal conductivity in porous amorphous SiO_2 in a systematic way, with a wider range of porosities and pore sizes.

In Chapter 6, we study the effects of porous structure on thermal conductivity in mesoporous amorphous SiO_2. Sol-gel and nanoparticle-based mesoporous amorphous SiO_2 thin films were synthesized by evaporation-induced self-assembly using tetraethyl orthosilicate and pre-made SiO_2 nanoparticles as the framework precursors, respectively, and block copolymers Pluronic P123 and Pluronic F127 as the templates. The porosity of the films ranged from 9 to 69%, the pore diameter ranged from 3 to 19 nm, the thickness ranged from 150 to 1000 nm, and the thermal conductivity ranged from 0.07 and 0.66 W/mK. The thermal conductivity decreased strongly with increasing porosity and was affected by the framework texture (i.e., continuous or nanoparticulate) and pore size. A porosity-weighted simple effective medium approximation was employed to explain the difference between the continuous and nanoparticulate frameworks. In the nanoparticle-based films, the minimum cross-section must be equal to or larger than the size of a SiO_2 nanoparticle. Since the size of nanoparticles is uniform throughout the network, the heat conduction has an equal probability of going along any jointed nanoparticle chains as it does in a parallel medium model. In contrast, the continuous sol-gel networks feature thin necks that can be readily reduced by changing pore size and porosity. The different cross-sectional areas lead to heat thermal transport behavior similar to that in a serial medium model. The thin necks in the sol-gel network create significant thermal resistance resulting in the low thermal conductivity in sol-gel based SiO_2 films at lower porosity.

Chapter 7 further elucidates the effect of pore size on thermal conductivity in nanoparticle-based and sol-gel based mesoporous SiO_2 films. Using a similar method to that in Chapter 6, nanoparticle-based SiO_2 films were templated with Pluronic surfactant and colloidal PMMA with pore sizes ranging from 10 – 70 nm. Sol-gel based SiO_2 films were templated with BrijC10, Pluronic surfactant, and PBO-PEO block copolymer with pore sizes ranging from 3 – 25 nm.

Although the wall thickness increases dramatically with pore size, we found that the thermal conductivities in the nanoparticle-based films are nearly the same at the same porosity despite different pore sizes. On the other hand, sol-gel based mesoporous SiO_2 films show decreasing thermal conductivity in the films with decreasing pore size. The different dependencies on pore size of the two systems is attributed to the nature of the frameworks. In the discontinuous nanoparticle-based framework, the characteristic length for phonon scattering is the size of individual pre-formed nanoparticles, and is therefore independent of pore size. In the continuous sol-gel network, the characteristic length for phonon scattering is the wall size, which is dependent on pore size and porosity. These studies together provide new insights into thermal transport in nanostructured materials, and suggest design rules of nanoscale architecture to control the thermal conductivity of mesoporous materials for a wide range of applications.

1.1 References

(1) Simon, P.; Gogotsi, Y.; Dunn, B. Materials Science. Where Do Batteries End and Supercapacitors Begin? *Science* **2014**, *343* (6176), 1210–1211.

(2) Augustyn, V.; Simon, P.; Dunn, B. Pseudocapacitive Oxide Materials for High-Rate Electrochemical Energy Storage. *Energy Environ. Sci.* **2014**, *7* (5), 1597–1614.

(3) Conway, B. E. *Electrochemical Supercapacitors: Scientific Fundamentals and Technological Applications*; Kluwer-Academic, 1999.

(4) Winter, M.; Brodd, R. J. What Are Batteries, Fuel Cells, and Supercapacitors? *Chem. Rev.* **2004**, *104* (10), 4245–4269.

(5) Simon, P.; Gogotsi, Y. Materials for Electrochemical Capacitors. *Nat. Mater.* **2008**, *7* (11), 845–854.

(6) Conway, B. E.; Pell, W. G. Double-Layer and Pseudocapacitance Types of Electrochemical

Capacitors and Their Applications to the Development of Hybrid Devices. *J. Solid State Electrochem.* **2003**, *7* (9), 637–644.

(7) Conway, B. E. E.; Birss, V.; Wojtowicz, J. The Role and Utilization of Pseudocapacitance for Energy Storage by Supercapacitors. *J. Power Sources* **1997**, *66* (1–2), 1–14.

(8) Conway, B. E. TECHNICAL PAPERS' ELECTROCHEMICAL SCIENCE AND TECHNOLOGY Transition from "Supercapacitor" to "Battery" Behavior in Electrochemical Energy Storage. *Electrochem. Sci. Technol.* **1991**, *138* (6), 1539–1549.

(9) Wang, J.; Polleux, J.; Lim, J.; Dunn, B. Pseudocapacitive Contributions to Electrochemical Energy Storage in TiO_2 (Anatase) Nanoparticles. *J. Phys. Chem. C* **2007**, *111* (40), 14925–14931.

(10) Augustyn, V.; Come, J.; Lowe, M. a; Kim, J. W.; Taberna, P.-L.; Tolbert, S. H.; Abruña, H. D.; Simon, P.; Dunn, B. High-Rate Electrochemical Energy Storage through Li+ Intercalation Pseudocapacitance. *Nat. Mater.* **2013**, *12* (6), 518–522.

(11) Kim, J. W.; Augustyn, V.; Dunn, B. The Effect of Crystallinity on the Rapid Pseudocapacitive Response of Nb_2O_5. *Adv. Energy Mater.* **2012**, *2* (1), 141–148.

(12) Brezesinski, K.; Wang, J.; Haetge, J.; Reitz, C.; Steinmueller, S. O.; Tolbert, S. H.; Smarsly, B. M.; Dunn, B.; Brezesinski, T. Pseudocapacitive Contributions to Charge Storage in Highly Ordered Mesoporous Group v Transition Metal Oxides with Iso-Oriented Layered Nanocrystalline Domains. *J. Am. Chem. Soc.* **2010**, *132* (20), 6982–6990.

(13) Come, J.; Augustyn, V.; Kim, J. W.; Rozier, P.; Taberna, P.-L.; Gogotsi, P.; Long, J. W.; Dunn, B.; Simon, P. Electrochemical Kinetics of Nanostructured Nb2O5 Electrodes. *J. Electrochem. Soc.* **2014**, *161* (5), A718–A725.

(14) Kim, H.-S.; Cook, J. B.; Tolbert, S. H.; Dunn, B. The Development of Pseudocapacitive

Properties in Nanosized-MoO2. *J. Electrochem. Soc.* **2015**, *162* (5), A5083–A5090.

(15) Okubo, M.; Hosono, E.; Kim, J.; Enomoto, M.; Kojima, N.; Kudo, T.; Zhou, H.; Honma, I. Nanosize Effect on High-Rate Li-Ion Intercalation in $LiCoO_2$ Electrode. *J. Am. Chem. Soc.* **2007**, *129* (23), 7444–7452.

(16) Liu, H.; Strobridge, F. C.; Borkiewicz, O. J.; Wiaderek, K. M.; Chapman, K. W.; Chupas, P. J.; Grey, C. P. Capturing Metastable Structures during High-Rate Cycling of $LiFePO_4$ Nanoparticle Electrodes. *Science (80-.).* **2014**, *344* (6191), 1252817–1252817.

(17) Lesel, B. K.; Ko, J. S.; Dunn, B.; Tolbert, S. H. Mesoporous $Li_xMn_2O_4$ Thin Film Cathodes for Lithium-Ion Pseudocapacitors. *ACS Nano* **2016**, *10* (8), 7572–7581.

(18) Lesel, B. K.; Cook, J. B.; Yan, Y.; Lin, T. C.; Tolbert, S. H. Using Nanoscale Domain Size to Control Charge Storage Kinetics in Pseudocapacitive Nanoporous $LiMn_2O_4$ Powders. *ACS Energy Lett.* **2017**, *2* (10), 2293–2298.

(19) Amos, C. D.; Roldan, M. A.; Varela, M.; Goodenough, J. B.; Ferreira, P. J. Revealing the Reconstructed Surface of $LiMn_2O_4$. *Nano Lett.* **2016**, *16* (5), 2899–2906.

(20) Hirayama, M.; Ido, H.; Kim, K.; Cho, W. Dynamic Structural Changes at $LiMn_2O_4$/Electrolyte Interface. *J. Am. Chem. Soc.* **2010**, *132* (14), 15268–15276.

(21) Lu, J.; Zhan, C.; Wu, T.; Wen, J.; Lei, Y.; Kropf, A. J.; Wu, H.; Miller, D. J.; Elam, J. W.; Sun, Y. K.; Qiu, X.; Amine, K. Effectively Suppressing Dissolution of Manganese from Spinel Lithium Manganate via a Nanoscale Surface-Doping Approach. *Nat. Commun.* **2014**, *5* (May), 1–8.

(22) Boukai, A. I.; Bunimovich, Y.; Tahir-Kheli, J.; Yu, J.-K.; Goddard Iii, W. A.; Heath, J. R. Silicon Nanowires as Efficient Thermoelectric Materials. In *Materials For Sustainable Energy: A Collection of Peer-Reviewed Research and Review Articles from Nature*

Publishing Group; World Scientific, 2011; pp 116–119.

(23) Dresselhaus, M. S.; Chen, G.; Tang, M. Y.; Yang, R. G.; Lee, H.; Wang, D. Z.; Ren, Z. F.; Fleurial, J.; Gogna, P. New Directions for Low-dimensional Thermoelectric Materials. *Adv. Mater.* **2007**, *19* (8), 1043–1053.

(24) Costescu, R. M.; Cahill, D. G.; Fabreguette, F. H.; Sechrist, Z. A.; George, S. M. Ultra-Low Thermal Conductivity in W/Al_2O_3 Nanolaminates. *Science (80-.).* **2004**, *303* (5660), 989–990.

(25) Hrubesh, L. W.; Pekala, R. W. Thermal Properties of Organic and Inorganic Aerogels. *J. Mater. Res.* **1994**, *9* (3), 731–738.

(26) Prasher, R. Thermal Interface Materials: Historical Perspective, Status, and Future Directions. *Proc. IEEE* **2006**, *94* (8), 1571–1586.

(27) Deng, Z.; Wang, J.; Wu, A.; Shen, J.; Zhou, B. High Strength SiO_2 Aerogel insulation1. *J. Non. Cryst. Solids* **1998**, *225*, 101–104.

(28) Hopkins, P. E.; Rakich, P. T.; Olsson, R. H.; El-Kady, I. F.; Phinney, L. M. Origin of Reduction in Phonon Thermal Conductivity of Microporous Solids. *Appl. Phys. Lett.* **2009**, *95* (16), 2007–2010.

(29) Hopkins, P. E.; Kaehr, B.; Phinney, L. M.; Koehler, T. P.; Grillet, A. M.; Dunphy, D.; Garcia, F.; Brinker, C. J. Measuring the Thermal Conductivity of Porous, Transparent SiO_2 Films With Time Domain Thermoreflectance. *J. Heat Transfer* **2011**, *133* (6), 61601.

(30) Larkin, J. M.; McGaughey, A. J. H. Thermal Conductivity Accumulation in Amorphous Silica and Amorphous Silicon. *Phys. Rev. B - Condens. Matter Mater. Phys.* **2014**, *89* (14), 1–12.

(31) Coquil, T.; Richman, E. K.; Hutchinson, N. J.; Tolbert, S. H.; Pilon, L. Thermal

Conductivity of Cubic and Hexagonal Mesoporous Silica Thin Films. *J. Appl. Phys.* **2009**, *106* (3), 1–11.

(32) Hu, C.; Morgen, M.; Ho, P. S.; Jain, A.; Gill, W. N.; Plawsky, J. L.; Wayner, P. C. Thermal Conductivity Study of Porous Low- *K* Dielectric Materials. *Appl. Phys. Lett.* **2000**, *77* (1), 145–147.

(33) Jain, A.; Rogojevic, S.; Ponoth, S.; Gill, W. N.; Plawsky, J. L.; Simonyi, E.; Chen, S. T.; Ho, P. S. Processing Dependent Thermal Conductivity of Nanoporous Silica Xerogel Films. *J. Appl. Phys.* **2002**, *91* (5), 3275–3281.

(34) Liu, J.; Gan, D.; Hu, C.; Kiene, M.; Ho, P. S.; Volksen, W.; Miller, R. D. Porosity Effect on the Dielectric Constant and Thermomechanical Properties of Organosilicate Films. *Appl. Phys. Lett.* **2002**, *81* (22), 4180–4182.

CHAPTER 2

Core/shell Nb_2O_5/Nb_4N_5-rGO Composites as a Novel High Rate Li-ion Pseudocapacitive Material

2.1 Introduction

The ever increasing popularity of portable electronic devices and electrical vehicles poses a high demand on today's energy storage devices. Supercapacitors are emerging as electrical energy devices that bridge between batteries and capacitors, offering higher power densities but lower energy densities than traditional batteries.[1–3] There are two types of charge storage mechanisms in supercapacitors, electric double layer capacitance (EDLC) and pseudocapacitance. EDLC is based on non-faradaic adsorption and desorption of charges on the interface between electrode and electrolyte; it generally has good power density and cycle life, but suffers from low energy density.[4–7] Pseudocapacitance, in comparison, occurs by charge transfer at or near the surface of a redox active material, offering the potential for energy densities approaching traditional batteries combined with higher power densities.[8–11] Higher energy densities in particular are found in materials where the pseudocapacitive region extends significant distances into a material in a process termed intercalation pseudocapacitance.[8,9,12–14] The extent of pseudocapacitive charge storage appears to be governed by a balance between ion diffusion rate and ion diffusion distance. For intercalation pseudocapacitance, there is the added structural consideration that ion intercalation should not induce a first order phase transition.[13,15,16] The interest for pseudocapacitive materials lies in achieving high capacities associated with the redox reactions while preserving the power density and cycle life of typical supercapacitors.

Nb_2O_5 is a promising material that shows very fast intercalation/deintercalation kinetics due to the facile two-dimensional Li^+ transport pathways within the structure in the orthorhombic phase.[13,15,17,18] Charge storage from the intercalation of lithium ions into Nb_2O_5 can be expressed as:

$$Nb_2O_5+xLi^++xe^-\leftrightarrow Li_xNb_2O_5$$

where the maximum capacity is 720 C/g with x = 2. However, it is also a large bandgap semiconductor, with a low bulk electrical conductivity of ~3.4 x 10^{-5} S/cm at 300 K.[19,20] The low electronic conductivity hinders its high-rate performance, especially for thick electrodes with high mass loadings.[15]

Numerous methods have been explored to improve the sluggish electron transport in Nb_2O_5. The most common approach is to build a carbon-Nb_2O_5 composite such as blending with carbon nanotubes,[21] growing on graphene,[22–24] and coating with carbon.[25–27] For example, a Nb_2O_5/carbon nanotube (CNT) nanocomposite can be made by physically mixing the components during slurry preparation.[21] The interpenetrating CNTs form a good network for fast electron transport and short Li^+ ion diffusion length, allowing a 300 C/g capacity at 50 mV/s scan rate, which is 60% of its value at 1 mV/s. However, the nature of the hetero-interface between carbonaceous materials and Nb_2O_5 leads to a lack of interfacial connectivity, which becomes especially important in long term cycling. In addition, due to high cost and difficulty in large scale production of high quality CNT and graphene,[28] great efforts are also directed to carbon-free coatings for achieving superior rate performance, and surface stability.[29,30]

One alternative for improving electrical conductivity is to convert some of the Nb_2O_5 into its conductive nitride analog, Nb_4N_5. Indeed, transition metal nitrides, such as TiN, VN and NbN are emerging as promising materials for supercapacitors due to their excellent electrical conductivity

which stands in sharp contrast to the inherently poor electron conductivity of many transition metal oxides.[31–38] Recently, Nb_4N_5 based aqueous supercapacitors reported good performance that was attributed to a combination of EDLC effects and proton absorption/desorption pseudocapacitance at the material surface.[39] Although a high aerial capacitance was achieved, the unique fast Li^+ intercalation pesudocapacitance of Nb_2O_5 is not utilized. Morover, most nitride studies were carried out in aqueous electrolytes, which limits the usable voltage window. Additionally, these electrodes can suffer from inevitable degradation due to electrochemical oxidation in the presence of water and oxygen.[39] While a few studies have used metal nitrides as the negative electrode in non-aqueous Li^+ batteries,[40–42] in most cases the metal nitride served as a conversion type electrode, in which Li^+ reacts with the metal nitride to form Li_3N and the corresponding metal. The intrinsic nature of conversion-type reactions limits their fast charging performance and cycle life due to complex structural and phase changes during cycling.

Herein, we report the fabrication of a core/shell Nb_2O_5/Nb_4N_5-reduced graphene oxide (rGO) composite structure and characterize it as a model metal oxide/metal nitride core/shell pseudocapacitive electrode material. Nb_2O_5 nanocrystals anchored to graphene sheets were first prepared using 2 wt% GO as a scaffold for growing uniform Nb_2O_5 nanoparticles. The materials were then converted to core/shell Nb_2O_5/Nb_4N_5-rGO by heating under flowing NH_3 and Ar (Scheme 2.1). Since the Nb_4N_5 is grown directly from Nb_2O_5, the interfacial ionic bonding ensures a robust structure and good electrical contact, which facilitate rapid charge transfer. The as-prepared core/shell Nb_2O_5/Nb_4N_5-rGO hybrid material exhibits excellent electrochemical kinetics attributed to the combination of the unique ionic conduction pathways in the orthorhombic Nb_2O_5 and interconnected electronic pathways through the Nb_4N_5 coating. In addition to studying the charge storage mechanism in this system using thin-film electrodes, traditional electrodes were

fabricated and demonstrated the potential for incorporating these core/shell materials in practical electrode structures.

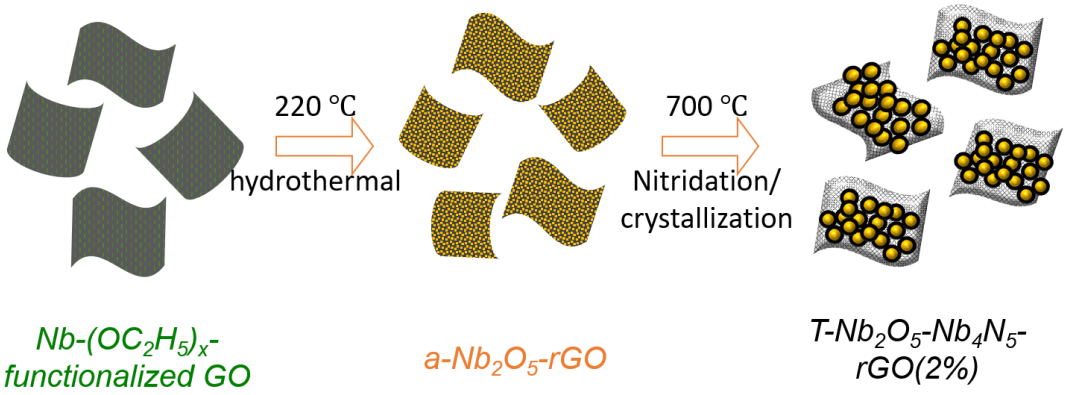

Scheme 2.1. Diagram illustrating the synthesis of Nb_2O_5/Nb_4N_5-rGO(2%) composite via hydrothermal reaction and nitridation.

2.2 Results

2.2.1 Materials characterization

Figure 2.1a shows as-synthesized Nb_2O_5 nanoparticles with an average size of 5 nm homogeneously scattered over a graphene sheet. The crystallization and nitridation of these Nb_2O_5 nanocrystals were completed simultaneously at 700 °C. This temperature allows the formation of electronically conductive tetragonal Nb_4N_5 (t-Nb_4N_5) phase and orthorhombic Nb_2O_5 (T-Nb_2O_5) without undesirable grain growth and aggregation.[45–47] After the thermal nitridation at 700 °C, the particle size increases to 20-30 nm, as shown in Figure 2.1b and Figure 2.2. Energy dispersive X-ray spectroscopy (EDAX) (Figure 2.3) maps out the elements in the nitridated sample, indicating a homogeneous distribution of Nb, O and N. Since this is a solid-gas reaction at high temperature, the rate determining step is the diffusion of the gas through each solid grain, a process that should be very homogeneous for our nanosized materials.[48,49] Upon reaction with ammonia, the surface first turns into nitride as NH_3 diffuses through the structure. The high resolution TEM (Figure 2.1c) reveals a core-shell structure with orthorhombic Nb_2O_5 comprising the core and tetragonal

Nb_4N_5 in a shell-like structure. There is also a 1-2 nm thin layer of amorphous oxide or oxy-nitride on the surface. The amorphous layer is likely formed after the nitridation was complete, when the sample is exposed to air.[39,50,51]

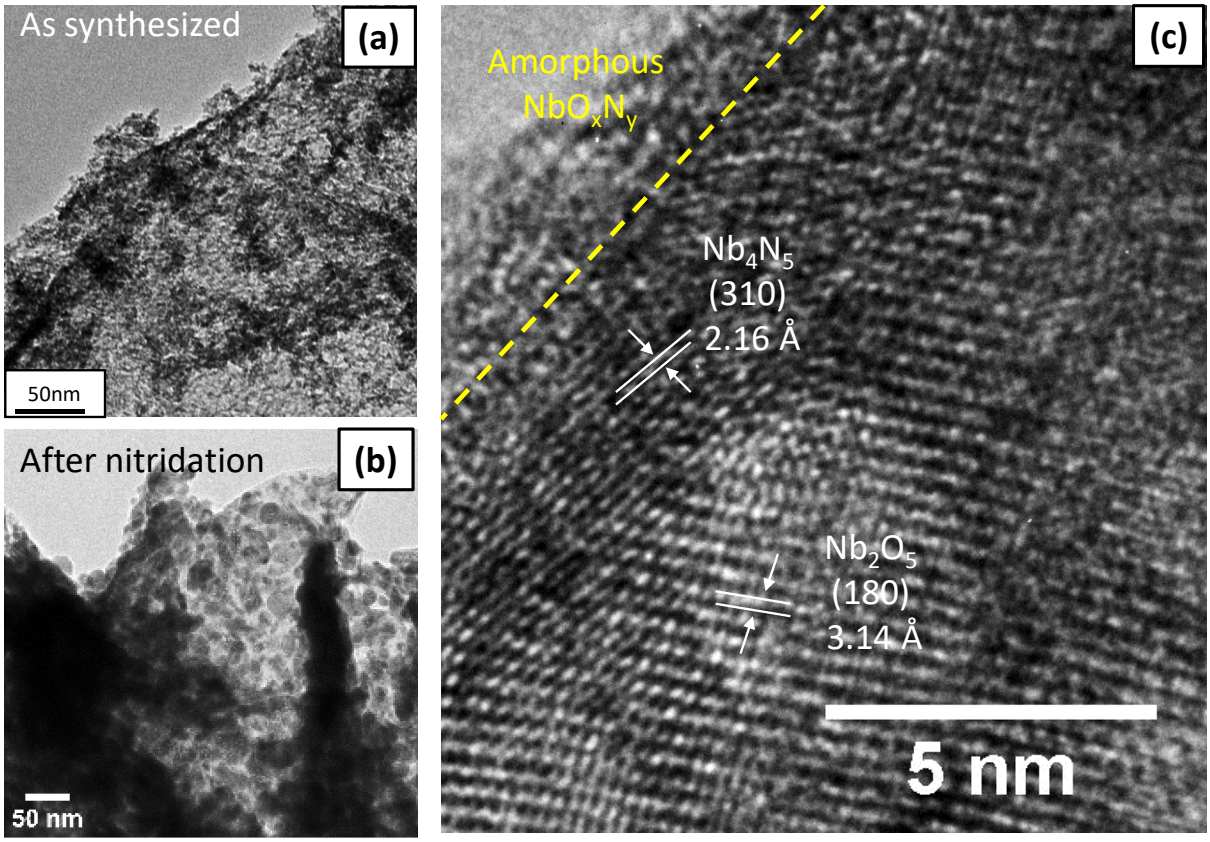

Figure 2.1. TEM images of (a) as synthesized a-Nb_2O_5-rGO and (b) nitridated T-Nb_2O_5/Nb_4N_5-rGO; (c) HRTEM image of Nb_2O_5/Nb_4N_5-rGO after 20 second nitridation. Lattice spacing of orthorhombic Nb_2O_5 and tetragonal Nb_4N_5 can be seen in a core-shell structure. A thin amorphous surface layer can also be observed.

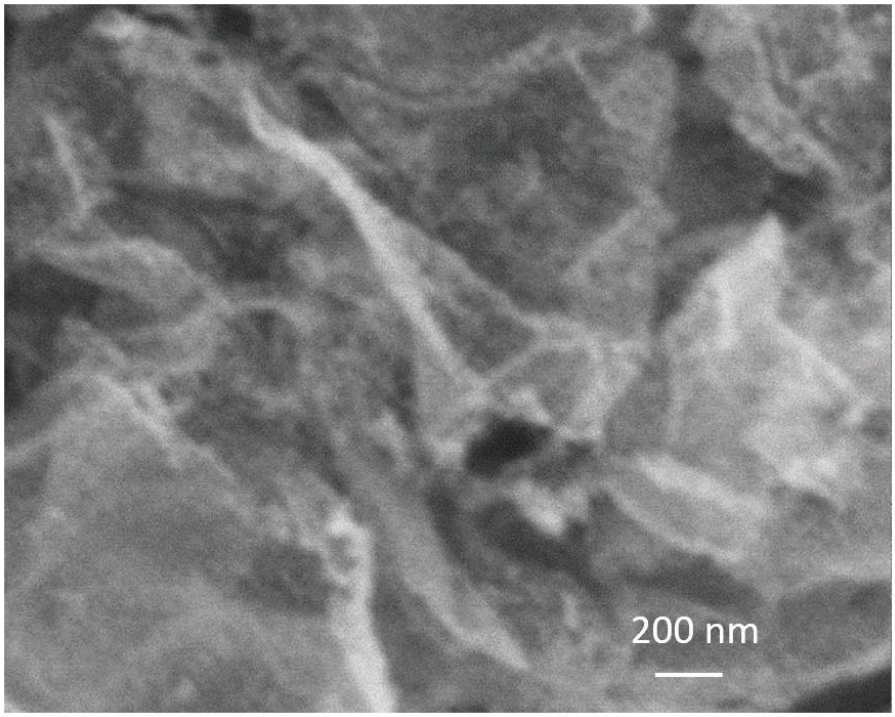

Figure 2.2. SEM of a Nb_2O_5/Nb_4N_5-rGO composite, showing 20-30 nm nanocrystals distributed on the rGO sheets.

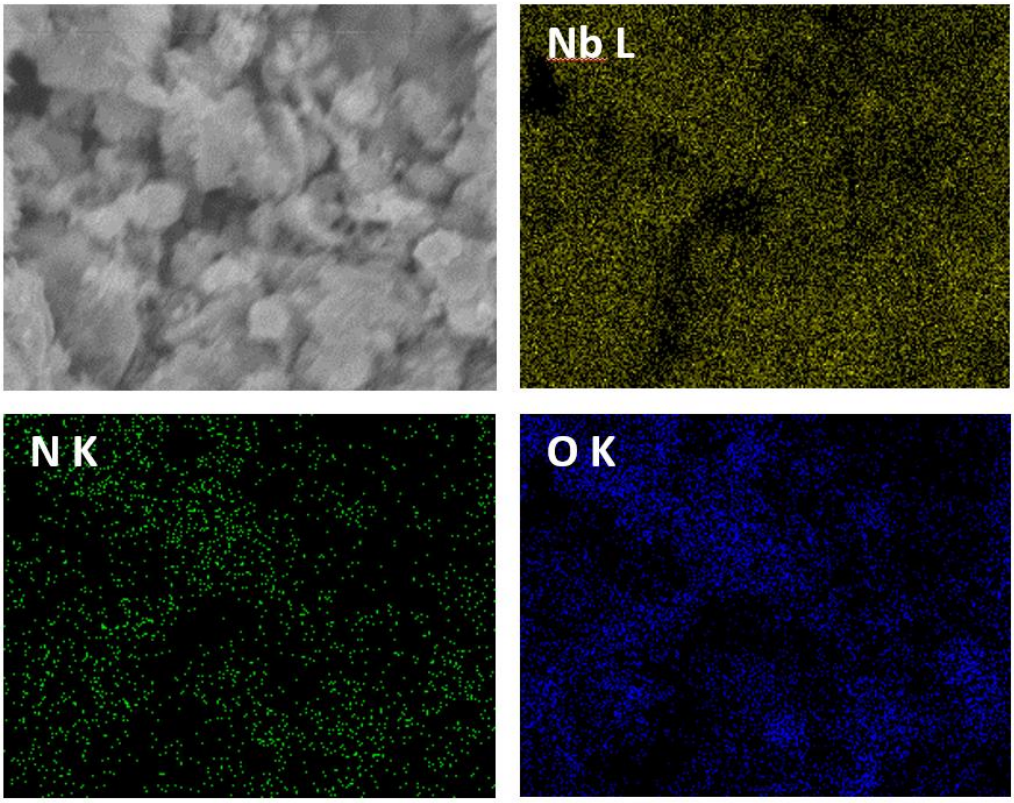

Figure 2.3. EDAX mapping of a Nb_2O_5/Nb_4N_5-rGO composite, displaying a homogeneous distribution of Nb, N and O.

The oxide/nitride ratio can be varied with the thermal nitridation process. Figure 2.4 shows the X-ray diffraction patterns of the samples nitridated for different time. Mass ratios of crystalline oxide/nitride were estimated from X-ray diffraction patterns using the reference intensity ratio (RIR) from the ICDD database.[52,53] It is noted the nanoparticles are very small compared to the X-ray penetration depth, which means that the X-rays will homogeneously sample the entire material. However, it is recognized that there are limitations to the RIR method, so here the oxide/nitride ratio should be only taken as a semi-quantitative measurement for relative comparison.[54] Table 2.1 shows the estimated T-Nb_2O_5 (orthorhombic)/t-Nb_4N_5 (tetragonal) weight ratio as a function of reaction time. With a quick 10 seconds soaking at 700 °C, a 6 wt% Nb_4N_5 shell formed on the

surface layer, while a 30 second soaking raised the nitride content to 51 wt%. The samples were completely nitridated when NH_3 flowed for 10 minutes.

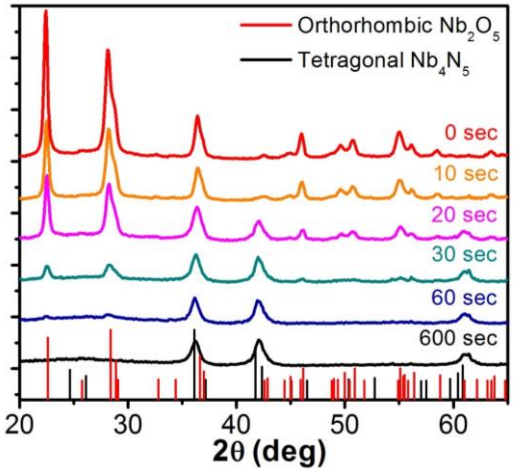

Figure 2.4. X-ray diffraction patterns for Nb_2O_5/Nb_4N_5-rGO(2%) composites prepared at 700 °C in flowing 50%/50% NH_3/Ar for different amounts of time, as indicated on the figure. Red and black lines correspond to orthorhombic Nb_2O_5 and tetragonal Nb_4N_5, respectively.

Table 2.1. Weight percentage of Nb_2O_5/Nb_4N_5 in the composites as a function of reaction time

Nitridation Time	Nb_2O_5/Nb_4N_5 (wt%)*
10 sec	94/6
20 sec	81/19
30 sec	49/51
60 sec	27/73
600 sec	0/100

*Determined form the integrated diffraction intensity.
*Each weight ratio reported here was averaged over five samples, with a relative error within 10%

X-ray photoelectron spectroscopy (XPS) measurements were performed to study the chemical composition and oxidation state of the composite. Figure 2.5a reveals that the Nb 3d peak is composed of 2 sets of the spin-orbit doublet corresponding to Nb $3d_{3/2}$ and Nb $3d_{5/2}$. The peaks at

206.9 eV and 209.7 eV are attributed to Nb^{5+} in Nb_2O_5, suggesting the surface is mostly oxidized, which agrees with the TEM observation. The little humps at 205.5 eV and 208.3 eV are assigned to Nb^{5+} in NbN_xO_y.[39,55,56] In the O 1s spectra (Figure 2.5b), the peaks at 529.7 eV and 531.8 eV correspond to O^{2-} in Nb_2O_5 and in NbN_xO_y, respectively. The high intensity of the O 1s peaks confirm the surface oxidation layer. To analyze the layer beneath the surface, Ar^+ etching was performed to remove the surface layer.[57] Figures 2.5d-2.5f display the spectra after Ar^+ etching. Figure 2.5d shows a much lower intensity of Nb^{5+} 3d peaks and the appearance of peaks at 203.3 eV and 206.1 eV, which correspond to Nb^{3+} 3d in Nb_4N_5. The large increase in the intensity of the N 1s peak at 397.2 eV (Figure 2.5f vs. Figure 2.5c), which is attributed to Nb-N in Nb_4N_5, also confirms the increase of Nb_4N_5, suggesting an inner layer of nitride under the surface oxide. The coexistence of both N and O signals is due to the nature of the core shell structure, which makes it difficult to expose regions of exclusively oxide or nitride. Nevertheless, the increased ratio of Nb^{3+}/Nb^{5+} and the increased intensity of N peak corroborates the proposed core-shell structure.

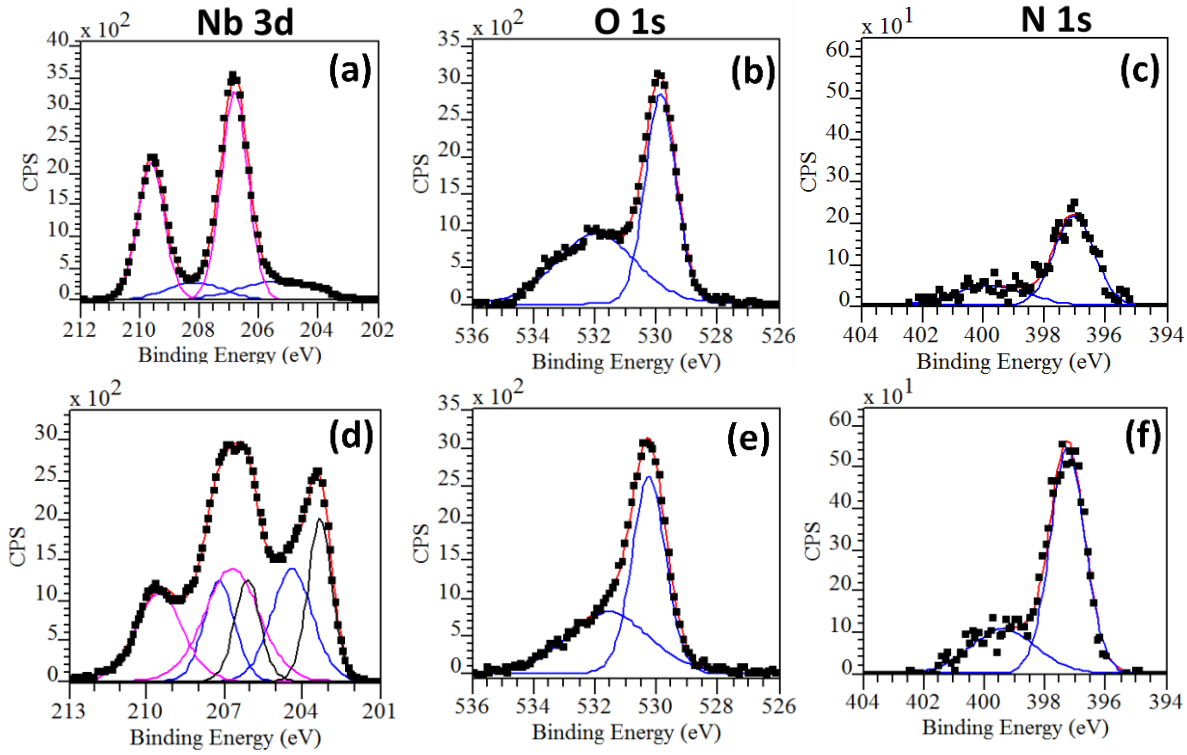

Figure 2.5. High-resolution X-ray photoelectron spectra of Nb 3d (a) and (d), O 1s (b) and (e), and N 1s (c) and (f) peaks of Nb_2O_5/Nb_4N_5-rGO samples before (a)-(c) and after (d)-(f) Ar-ion etching. Before etching, the samples surface is dominated by an amorphous niobium oxide or oxy-nitride layer. After etching, clean signatures of Nb_2O_5 and Nb_4N_5 are observed.

2.2.2 Charge storage studies with thin film electrodes

To explore the potential of using metal nitrides as a conductive coating for metal oxides and to understand the fundamental electrochemical properties of the Nb_2O_5/Nb_4N_5-rGO composite, electrochemical measurements were made on thin film electrodes. A typical mass loading was around 30 μg/cm^2. At this mass loading, no electrical additive nor binder are needed. Therefore, we can study the electrochemical properties of the composite without any complications from additives or electrode architecture. Figure 2.6a shows cyclic voltammograms collected at 5 mV/s for Nb_2O_5/Nb_4N_5-rGO composites with different crystalline oxide/nitride mass ratios. Clear redox peaks at 1.5 V (cathodic sweep) and 1.8 V (anodic sweep) are observed in the Nb_2O_5-rGO trace, which are the signature peaks for orthorhombic Nb_2O_5.[13,17,18] As the nitride percentage increases

to 19%, the signature peaks are still well retained. However, further increase in nitride percentage changes the CV shape – the redox feature starts to diminish, and the overall shape tends to resemble the rectangular box of a double layer capacitor. This response occurs because as the electrochemically inactive Nb_4N_5 shell gets thicker, it prevents effective Li^+ intercalation into the Nb_2O_5, resulting in more prominent double layer capacitance features. Eventually, the fully nitridated sample Nb_4N_5-rGO displays only a rectangular box-like shape with no redox peaks, which is typical of electrical double layer capacitance. This shape change is accompanied by much lower specific capacity since no redox activity is involved.

Rate capabilities of the Nb_2O_5/Nb_4N_5-rGO composite with different crystalline oxide/nitride mass ratios were studied by cyclic voltammetry at 10-200 mV/s (Figure 2.6b). Nb_2O_5-rGO has a lithium capacity of 458 C/g at 10 mV/s, which decreases to 218 C/g at 200 mV/s. As some of the oxide converted to nitride, the electrical conductivity of the composite increased. A 6% nitride composite improved the capacity retention at fast rates with storage of 273 C/g at 200 mV/s. Even better performance was evident with Nb_2O_5(81%)/Nb_4N_5(19%)-rGO which achieved 413 C/g at 10 mV/s and 340 C/g at 200 mV/s with more than 82% capacity retention. Nb_4N_5 has excellent electrical conductivity which improves the electron transport through the composite, leading to higher levels of charge storage at fast rates. However, due to the fact that Nb_4N_5 is electrochemically inactive in the voltage window of 1.2-3 V vs Li^+/Li, a small amount of capacity is sacrificed at slow rates. Interestingly, further increasing the Nb_4N_5/Nb_2O_5 ratio does not further improve kinetic behavior. For a Nb_2O_5(49%)/ Nb_4N_5(51%)-rGO composite, the capacity dropped to 320 C/g at 10 mV/s, and capacity retention at high rates is not as good as Nb_2O_5(81%)/Nb_4N_5(19%)-rGO. This is most likely because the thicker nitride layer blocks effective Li^+ intercalation into Nb_2O_5. Although Nb_4N_5 has a cation-defective NaCl-type lattice

structure which has a possible pathway for Li diffusion,[39,45] that pathway is highly dependent on vacancy ordering. As a result, even if pathways for Li ion diffusion through Nb_4N_5 exist, they will still slow down Li^+ transport in thick nitride layers compared to the facile pathway in the 2D layers of Nb_2O_5. For the fully nitridated sample, the capacity is only about 30 C/g, attributed only to electrical double layer capacitance.

These results show that different charging mechanisms are observed based on the nitride/oxide ratio. The thickness of the nitride layer affects the Li^+ conduction. A thin shell of nitride over Nb_2O_5 nanoparticles that allows Li^+ intercalation/deintercalation without much difficulty can provide high electrical conductivity and significantly improve charge storage kinetics. A thick layer of nitride over Nb_2O_5, however, blocks the effective Li^+ conduction into Nb_2O_5 despite the high electrical conductivity.

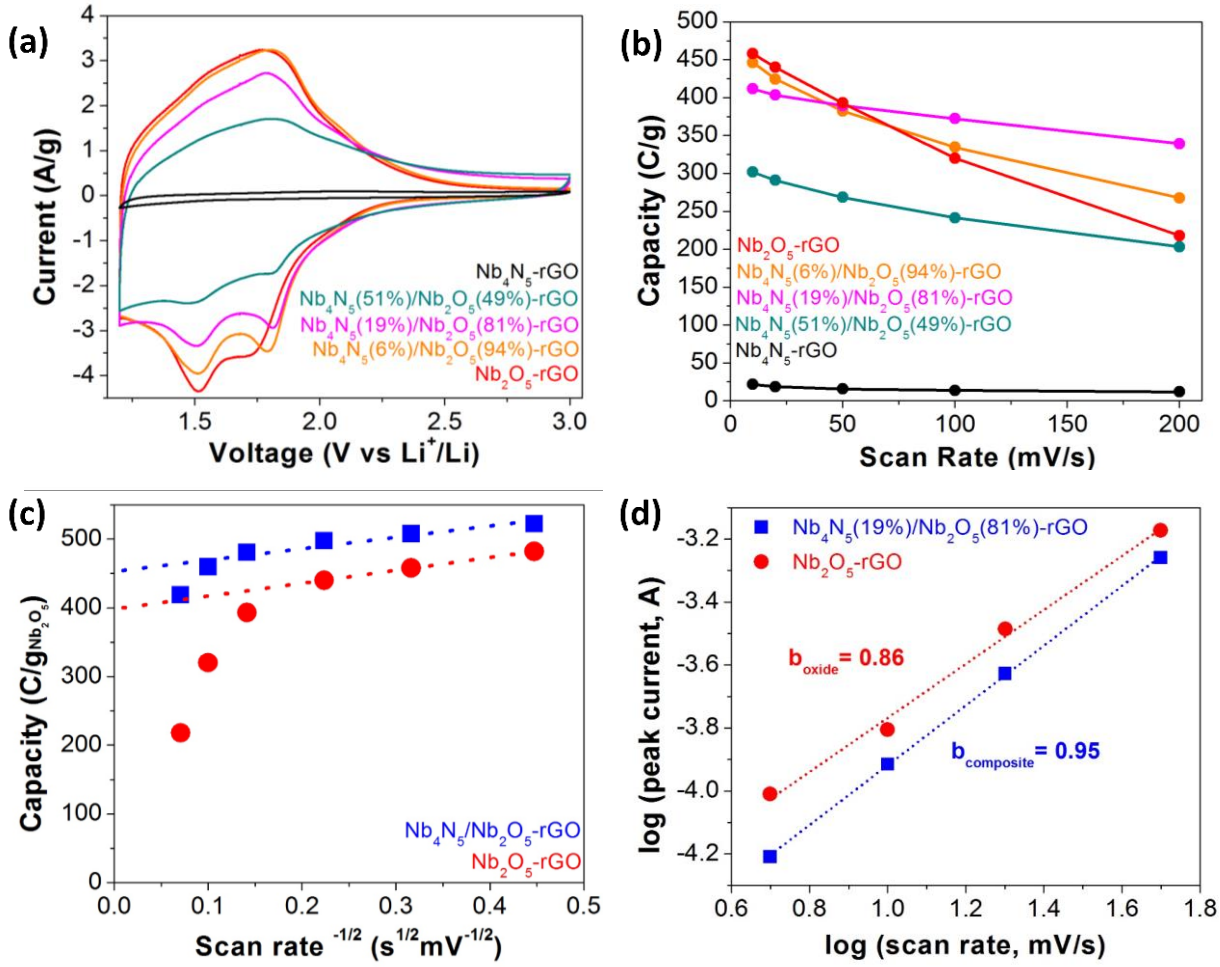

Figure 2.6. Electrochemical performance of Nb_2O_5/Nb_4N_5-rGO tested in a thin film configuration (~30 µg/cm^2 mass loading). (a) Cyclic voltammogram of the composites with different Nb_2O_5/Nb_4N_5 ratio at 5 mV/s; (b) capacity from CV as a function of scan rate plot of composites with different Nb_2O_5/Nb_4N_5 ratio. The 19% nitride composite shows the best combination of high capacity and excellent capacity retention and high sweep rate; (c) A plot of capacity vs scan rate$^{-1/2}$ plot from 5 to 200 mV/s for Nb_2O_5(81%)/Nb_4N_5(19%)-rGO and Nb_2O_5-rGO. Higher extrapolated capacitive contribution is obtained for the nitride containing sample. (d) The plot of log(peak current) versus log(scan rate) plotted from 5 to 50 mV/s for anodic peak for the same two samples used in part (c). The nitride containing sample shows a b-value very close to 1, indicating capacitive behavior.

To further understand how the integration of Nb_4N_5 into the composites leads to improved kinetics, the charge storage dependence on sweep rate was analyzed based on Trasatti's method.[58] Generally, the total stored charge, q, involves two types of contributions: capacitive charge storage and diffusion controlled charge storage. Trasatti associated this capacitive contribution with

surface redox reaction, but it can equally represent intercalation pseudocapacitance. The diffusion controlled contribution generally refers to battery-like intercalation. Capacitive charge storage is not dependent on scan rate while the slower intercalation is diffusion controlled and does depend on scan rate. Assuming semi-infinite diffusion, q is linearly related to the reciprocal of the square root of the scan rate (v), leading to the following equation:

$$q\,(v) = q_0 + k^*(v^{-1/2}) \quad (1)$$

where q_0 is the capacitive contribution to charge storage, k is a constant and $k*(v^{-1/2})$ represents the diffusion-controlled contribution to charge storage. Figure 2.6c shows q as a function of $v^{-1/2}$ for Nb_2O_5(81%)/Nb_4N_5(19%)-rGO and Nb_2O_5-rGO based on their cyclic voltammograms collected at sweep rates between 5 mV/s and 200 mV/s. The capacities are normalized by Nb_2O_5 weight only, since Nb_2O_5 is the only active component that contributes to the charge storage. Extrapolating the straight line to the y -axis intercept point allows us to determine the contribution from capacitive charge storage. The two extrapolated lines are almost parallel, suggesting the layer of nitride in Nb_2O_5(81%)/Nb_4N_5(19%)-rGO does not block facile Li^+ transport through the oxide-nitride interface. However, the y-intercept for the 19% nitride sample is 54 C/g higher than the pure oxide, indicating that a larger fraction of the total stored charge is capacitive. This comparison quantitatively shows that the nitride coating does not affect the availability of Nb_2O_5 sites nor does it block Li^+ intercalation into the Nb_2O_5 lattice, a fact that is consistent with the observed improved rates performance.

We can also analyze the charge storage kinetics by determining the dependence of peak currents on scan rates. Generally, the current (i) varies with the scan rate (v) according to the following equation:

$$i = av^b \quad (2)$$

where a and b are constants. The value of b can be between 0.5 and 1, with a b-value of 0.5 indicating a diffusion-controlled process and a b-value of 1 representing capacitive behavior .[13,18] Figure 2.6d presents a plot of log(i) versus log(*v*) from 5 to 50 mV/s for the main anodic peak in both the optimized Nb_2O_5(81%)/Nb_4N_5(19%)-rGO and the pure Nb_2O_5-rGO materials. The b-value for the anodic peaks in the optimized composite is 0.95 while that in the oxide sample is 0.86, indicating that the kinetics are dominated by capacitor-like behavior for both samples, with the nitride containing material exhibiting a stronger response.

2.2.3 Electrochemical properties of slurry electrodes

The electrochemical properties of core/shell Nb_2O_5/Nb_4N_5-rGO particles fabricated into practical electrode structures provide insight regarding the performance of these materials in potential device applications. Figure 2.7a shows cyclic voltammograms of Nb_4N_5(19%)/Nb_2O_5(81%)-rGO in the voltage window of 1.2-3 V vs Li/Li^+ at scan rates between 1 mV/s and 20 mV/s. The responses are characterized by the broad cathodic and anodic peaks which are the redox signatures of orthorhombic Nb_2O_5. Figure 2.7b uses the CV data like those in Figure 2.7a to determine the rate of charge storage for both Nb_2O_5(81%)/Nb_4N_5(19%)-rGO and Nb_2O_5-rGO. Nb_2O_5(81%)/Nb_4N_5(19%)-rGO exhibits much faster kinetics than Nb_2O_5-rGO as 500 C/g, or about 80% of the original capacity, is stored within 90 seconds. The excellent charging rate demonstrated by the optimized Nb_2O_5(81%)/Nb_4N_5(19%)-rGO composite electrode can be attributed to the homogeneous coverage of the conductive nitride shell as well as the increased conductivity between core/shell nanoparticles.

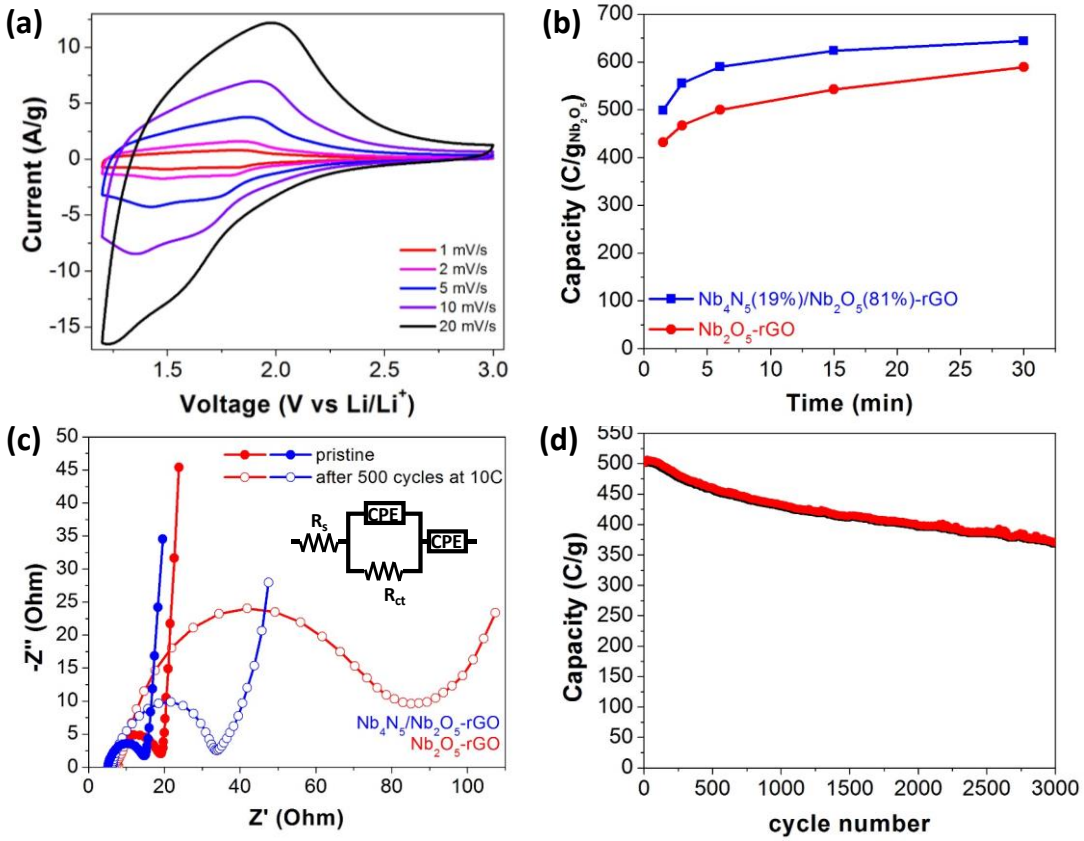

Figure 2.7. Electrochemical performance of T- Nb_2O_5/ Nb_4N_5-rGO tested in traditional slurry electrodes (~1 mg/cm^2 mass loading). (a) Cyclic voltammograms of Nb_2O_5(81%)/Nb_4N_5(19%)-rGO at different scan rates; (b) capacity for Nb_2O_5(81%)/Nb_4N_5(19%)-rGO and Nb_2O_5/rGO as a function of charging time; (c) Impedance spectra of Nb_2O_5(81%)/Nb_4N_5(19%)-rGO and Nb_2O_5/rGO before and after 500 cycles at 10C. Both samples show reasonable low charge transfer resistance before cycling, but that low resistance is much better retained in the nitride containing sample; (d) Cycle life of Nb_2O_5(81%)/Nb_4N_5(19%)-rGO at 10C. Good capacity retention is observed over 3000 cycles.

Electrochemical impedance spectroscopy (EIS) furthers our understanding of the conductivity difference between Nb_2O_5(81%)/Nb_4N_5(19%)-rGO and pure Nb_2O_5-rGO. A Nyquist plot (Figure 2.7c) consists of a semicircle in the high frequency regime and an oblique straight line at lower frequency. The data can be simulated with an equivalent circuit model as shown in the inset. Serial resistance (R_s) represents the impedance contributed by the film resistance and the contact resistance. The diameter of the semicircle is associated with charge transfer resistance (R_{ct}). For the pristine electrodes, the charge transfer resistance (R_{ct}) values are 10.2 and 13.8 Ω for Nb_2O_5

(81%)/Nb_4N_5(19%)-rGO and Nb_2O_5-rGO, respectively, indicating good electrical conduction in both samples. After 500 cycles at 10 C, the charge transfer resistance in Nb_2O_5-rGO increased to 63.8 Ω while that of the composite only increased to 27.2 Ω. The increased resistance is attributed primarily to solid-electrolyte interphase (SEI) formation during cycling. The presence of the Nb_4N_5 shell, which covers the Nb_2O_5 homogeneously, diminishes the contact between the electrolyte and the Nb_2O_5 and thus minimizes SEI formation. In addition, the connectivity between nanoparticles maintains good electrical conductivity throughout the electrode despite the SEI formation. In the case of Nb_2O_5-rGO, however, SEI formation on the surface of Nb_2O_5 can prevent efficient electrical contact between Nb_2O_5 and carbon additives.

Long term galvanostatic cycling of the composite sample at a rate of 10 C (Figure 2.7d) yields an impressive 73 % retention after 3000 cycles. To check the structural integrity after cycling, Nb_2O_5(81%)/Nb_4N_5(19%)-rGO was examined by XPS (Figure 2.8a) and XRD (Figure 2.8b), which indicated excellent retention of surface composition and crystal structure before and after 500 cycles at 10 C. The robust cycling performance of the composite is attributed to the high rate charge storage properties of Nb_2O_5 as well as the intimate connection between the interconnected constituents, Nb_4N_5 and rGO.

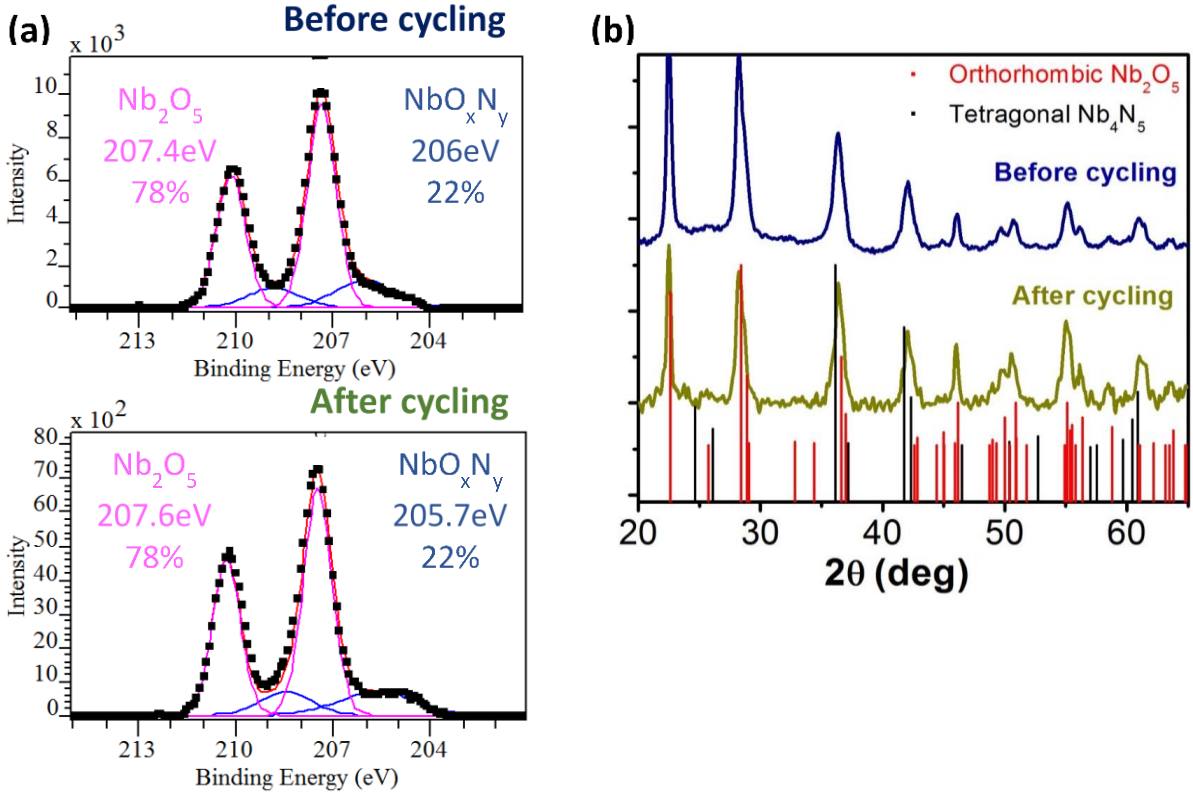

Figure 2.8. (a) XPS spectra of the Nb 3d core level and (b) XRD powder patterns for the Nb_2O_5(81%)/Nb_4N_5(19%)-rGO before and after cycling. The surface composition and crystal structure are the same before and after 500 cycles at 10C, indicating that the structural integrity is well maintained during cycling.

2.3. Conclusions

We have demonstrated that Nb_2O_5/Nb_4N_5-rGO particles can be synthesized by partial nitridation of Nb_2O_5 in NH_3, and that the nitride/oxide ratio can be well controlled by reaction time. The core/shell structure provides excellent electronic pathways that connect Nb_2O_5 nanoparticles. The fundamental charge storage mechanism is studied using a series of composites with different nitride/oxide ratios. The composites show progressively more EDLC-like behavior with increasing ratio of nitride to oxide, resulting in a significantly lower capacity. The optimal 20% nitride shell enhanced the electrical conductivity of the system without blocking Li^+ transport into the Nb_2O_5. The combination of a robust electrical network of Nb_4N_5 and fast Li^+ conduction in Nb_2O_5 leads to overall fast kinetics. More than 80% of capacity can be accessed within a 10

second charging time in thin film configurations, and more than 500 C/g can be obtained within 90 seconds in a typical slurry electrode. Impedance spectra suggest that the fast kinetics originate from the good electrical contact between Nb_4N_5 and Nb_2O_5 and that the shell may possibly limit SEI formation. Overall, we have demonstrated an in-situ process for creating a core/shell structure for an oxide/nitride composite that is capable of fast kinetics and good cycling performance. We foresee that these unique structures are promising alternatives to carbon composites for electrical conductivity enhancement, especially for application in high rate charge storage devices.

2.4. Experimental Methods

2.4.1 Synthesis of graphene oxide

Graphene oxide (GO) was synthesized by using modified Hummer's method.[57] In the synthesis, 2 g graphite powders (Alfa Alser, 2-15 μm, ≥ 99.9995 %) were dispersed in 40 mL H_2SO_4/H_3PO_4 (Sigma-Aldrich) at a 9:1 volume ratio. After stirring for 2 hr in an ice bath, 6 g $KMnO_4$ (Sigma-Aldrich, ≥ 99%) was added to the solution, which triggered an exothermal reaction and increased the temperature to around 40 °C. The solution was kept at 50 °C for the next 2 hr until a viscous grey paste was observed. After cooling down naturally, 360 mL cold DI-water was poured into the solution, followed by treating with 3 mL H_2O_2 (Sigma-Aldrich, 30 wt%) with 1 hr ultrasonication. The bright-yellow solution was washed thoroughly with 5 M HCl and re-dispersed in DI-water to form a 5 g/L GO suspension.

2.4.2 Synthesis of Nb_2O_5-rGO

Nb_2O_5-anchored rGO was synthesized by using a hydrothermal method.[58] 960 mg $NbCl_5$ (Sigma-Aldrich, ≥ 99.9%) was first dissolved in 15 mL isopropanol in an ice bath by vigorous stirring. The precursor solution was then added to a 10 mL GO isopropanol solution (5 g/L), followed by 30-min ultrasonication to achieve homogeneous mixing. The mixture was aged for 1

day without further agitation and transferred to a 40 mL Teflon liner in a sealed Parr bomb at 220 °C for 12 hours. The as-synthesized Nb_2O_5-anchored reduced-GO (Nb_2O_5-rGO) formed a black porous monolith with the clear solvent. The powders were washed thoroughly with isopropanol and dried in an oven at 70 °C. The content of rGO is determined by TGA. (figure S1)

2.4.3 Synthesis of Nb_2O_5/Nb_4N_5-rGO composite

The as synthesized Nb_2O_5-rGO powders were partially converted to core/shell Nb_2O_5/Nb_4N_5-rGO through a solid-gas reaction with NH_3 gas. The reaction was carried out in a tube furnace under Ar flow at a low flow rate of 30 mL/min with a ramp of 10 °C/min. Once the sample reached 700 °C, NH_3 gas was turned on to maintain a flow of NH_3/Ar (NH_3 50 vol%:Ar 50 vol%, Air Gas) for a chosen amount of time. The system was cooled to room temperature under flowing Ar.

2.4.4 Materials characterization

Transmission electron microscopy (TEM) was performed using an FEI Technai T12 transmission electron microscope operating at 120 kV. High resolution TEM (HRTEM) micrographs were collected using an FEI Titan S/TEM operating at 300 kV in transmission mode. Scanning electron microscopy (SEM) and elemental mapping images were obtained using a JEOL model 6700F electron microscope with an energy dispersive X-ray spectroscopy (EDAX) attachment. X-ray diffraction (XRD) patterns were collected with a PANalytical X'Pert Pro diffractometer operating with Cu Kα ($\lambda = 1.5418$ Å) using a 0.05° step size, an accelerating voltage of 40 kV, and a current of 40 mA. X-ray photoelectron spectroscopy (XPS) analysis was performed using a Kratos Axis Ultra DLD with a monochromatic Al K-α radiation source. The charge neutralizer filament was used to control charging of the sample, a 20 eV pass energy was used with a 0.1 eV step size, and scans were calibrated using the C 1s peak shifted to 284.8 eV. Thermogravimetric analysis (TGA) was carried out using a SDT Q-600 TA instrument. The

sample was first heated to 200 °C at 5 °C/min and soaked isothermally for 2 hours in Ar. It was then heated to 450 °C at 5 °C/min and soaked isothermally for 2 hours in Ar. Lastly the sample was heated to 900 °C at 5 °C/min and soaked for one hour in O_2.

2.4.5 Electrochemical characterization

Two types of electrodes with different mass loadings were fabricated and characterized. Thin-film electrodes without added carbon or binder enabled us to determine intrinsic electrochemical properties of core/shell Nb_2O_5/Nb_4N_5-rGO. Each thin-film electrode was prepared by drop-casting 30 μg active materials onto a plasma-cleaned stainless steel sheet. Thick electrodes comprised of Nb_2O_5/Nb_4N_5-rGO powder, acetylene carbon black, and polyvinylidene fluoride (PVDF) in a weight ratio 80:10:10 were doctor-bladed onto stainless steel foils with 1~1.2 mg/cm^2 material loading. The electrodes were transferred to a vacuum oven at 110 ℃ for complete drying. Thin-film samples were tested using a three-electrode flooded cell with 1M $LiClO_4$ in EC/DMC (1:1 in volume) electrolyte using lithium foils as counter and reference electrodes. The slurry electrodes were characterized in a two-electrode Swagelok cell with a lithium counter electrode and a glass fiber separator soaked in the same electrolyte. Cyclic voltammetry (CV), galvanostatic charge-discharge measurements and electrochemical impedance spectroscopy were carried out on a VMP potentialstat/galvanostat (Bio-Logic). Cyclic voltammetry was performed between 1.2 V and 3 V vs. Li/Li$^+$. The impedance measurements were performed between 900 kHz and 100 mHz using a 10 mV amplitude and no bias. All the electrochemical data were reproduced 3-5 times with a relative error within 4%.

2.5 References

(1) Simon, P.; Gogotsi, Y. Materials for Electrochemical Capacitors. *Nat. Mater.* **2008**, *7* (11), 845–854.

(2) Conway, B. E. *Electrochemical Supercapacitors: Scientific Fundamentals and Technological Applications*; Kluwer-Academic, 1999.

(3) Simon, P.; Gogotsi, Y.; Dunn, B. Materials Science. Where Do Batteries End and Supercapacitors Begin? *Science* **2014**, *343* (6176), 1210–1211.

(4) Zhu, Y.; Murali, S.; Stoller, M. D.; Ganesh, K. J.; Cai, W.; Ferreira, P. J.; Pirkle, A.; Wallace, R. M.; Cychosz, K. A.; Thommes, M.; Su, D.; Stach, E. A.; Ruoff, R. S. Carbon-Based Supercapacitors. *Science (80-.).* **2011**, *332* (6037), 1537–1541.

(5) El-Kady, M. F.; Strong, V.; Dubin, S.; Kaner, R. B. Laser Scribing of High-Performance and Flexible Graphene-Based Electrochemical Capacitors. *Science (80-.).* **2012**, *335* (6074), 1326–1330.

(6) An, K. H.; Kim, W. S.; Park, Y. S.; Moon, J.-M.; Bae, D. J.; Lim, S. C.; Lee, Y. S.; Lee, Y. H. Origin of the Open Circuit Voltage of Plastic Solar Cells. *Adv. Funct. Mater.* **2001**, *11* (5), 387–392.

(7) Lee, S. W.; Yabuuchi, N.; Gallant, B. M.; Chen, S.; Kim, B.-S.; Hammond, P. T.; Shao-Horn, Y. High-Power Lithium Batteries from Functionalized Carbon-Nanotube Electrodes. *Nat. Nanotechnol.* **2010**, *5* (7), 531–537.

(8) Conway, B. E.; Pell, W. G. Double-Layer and Pseudocapacitance Types of Electrochemical Capacitors and Their Applications to the Development of Hybrid Devices. *J. Solid State Electrochem.* **2003**, *7* (9), 637–644.

(9) Conway, B. E. E.; Birss, V.; Wojtowicz, J. The Role and Utilization of Pseudocapacitance for Energy Storage by Supercapacitors. *J. Power Sources* **1997**, *66* (1–2), 1–14.

(10) Shi, Y.; Pan, L.; Liu, B.; Wang, Y.; Cui, Y.; Bao, Z.; Yu, G. Nanostructured Conductive Polypyrrole Hydrogels as High-Performance, Flexible Supercapacitor Electrodes. *J. Mater.*

Chem. A **2014**, *2* (17), 6086.

(11) Augustyn, V.; Simon, P.; Dunn, B. Pseudocapacitive Oxide Materials for High-Rate Electrochemical Energy Storage. *Energy Environ. Sci.* **2014**, *7* (5), 1597.

(12) Rauda, I. E.; Augustyn, V.; Dunn, B.; Tolbert, S. H. Enhancing Pseudocapacitive Charge Storage in Polymer Templated Mesoporous Materials. *Acc. Chem. Res.* **2013**, *46* (5), 1113–1124.

(13) Augustyn, V.; Come, J.; Lowe, M. a; Kim, J. W.; Taberna, P.-L.; Tolbert, S. H.; Abruña, H. D.; Simon, P.; Dunn, B. High-Rate Electrochemical Energy Storage through Li+ Intercalation Pseudocapacitance. *Nat. Mater.* **2013**, *12* (6), 518–522.

(14) Cook, J. B.; Kim, H. S.; Yan, Y.; Ko, J. S.; Robbennolt, S.; Dunn, B.; Tolbert, S. H. Mesoporous MoS2 as a Transition Metal Dichalcogenide Exhibiting Pseudocapacitive Li and Na-Ion Charge Storage. *Adv. Energy Mater.* **2016**.

(15) Come, J.; Augustyn, V.; Kim, J. W.; Rozier, P.; Taberna, P.-L.; Gogotsi, P.; Long, J. W.; Dunn, B.; Simon, P. Electrochemical Kinetics of Nanostructured Nb_2O_5 Electrodes. *J. Electrochem. Soc.* **2014**, *161* (5), A718–A725.

(16) Kim, H.-S.; Cook, J. B.; Tolbert, S. H.; Dunn, B. The Development of Pseudocapacitive Properties in Nanosized-MoO_2. *J. Electrochem. Soc.* **2015**, *162* (5), A5083–A5090.

(17) Kim, J. W.; Augustyn, V.; Dunn, B. The Effect of Crystallinity on the Rapid Pseudocapacitive Response of Nb_2O_5. *Adv. Energy Mater.* **2012**, *2* (1), 141–148.

(18) Brezesinski, K.; Wang, J.; Haetge, J.; Reitz, C.; Steinmueller, S. O.; Tolbert, S. H.; Smarsly, B. M.; Dunn, B.; Brezesinski, T. Pseudocapacitive Contributions to Charge Storage in Highly Ordered Mesoporous Group v Transition Metal Oxides with Iso-Oriented Layered Nanocrystalline Domains. *J. Am. Chem. Soc.* **2010**, *132* (20), 6982–6990.

(19) de Filho, D. A. B.; Franco, D. W.; Filho, P. P. A.; Alves, O. L. Niobia Films: Surface Morphology, Surface Analysis, Photoelectrochemical Properties and Crystallization Process. *J. Mater. Sci.* **1998**, *33* (10), 2607–2616.

(20) Cava, R. J.; Batlogg, B.; Krajewski, J. J.; Poulsen, H. F.; Gammel, P.; Peck, W. F.; Rupp, L. W. Electrical and Magnetic Properties of Nb2O5-δ Crystallographic Shear Structures. *Phys. Rev. B* **1991**, *44* (13), 6973–6981.

(21) Wang, X.; Li, G.; Chen, Z.; Augustyn, V.; Ma, X.; Wang, G.; Dunn, B.; Lu, Y. High-Performance Supercapacitors Based on Nanocomposites of Nb2O5 Nanocrystals and Carbon Nanotubes. *Adv. Energy Mater.* **2011**, *1* (6), 1089–1093.

(22) Kong, L.; Zhang, C.; Zhang, S.; Wang, J.; Cai, R.; Lv, C.; Qiao, W.; Ling, L.; Long, D. High-Power and High-Energy Asymmetric Supercapacitors Based on Li + -Intercalation into a T-Nb 2 O 5 /graphene Pseudocapacitive Electrode. *J. Mater. Chem. A* **2014**, *2* (42), 17962–17970.

(23) Kong, L.; Zhang, C.; Wang, J.; Qiao, W.; Ling, L.; Long, D. Free-Standing T - Nb 2 O 5 / Graphene Composite Papers with Ultrahigh Gravimetric / Volumetric Capacitance for Li-Ion Intercalation. *ACS Nano* **2015**, No. Xx, 11200–11208.

(24) Arunkumar, P. . b; Ashish, A. G. .; Babu, B. .; Sarang, S. .; Suresh, A. .; Sharma, C. H. .; Thalakulam, M. .; Shaijumon, M. M. . Nb2O5/graphene Nanocomposites for Electrochemical Energy Storage. *RSC Adv.* **2015**, *5* (74), 59997–60004.

(25) Eunho Lim, Haegyeom Kim, Changshin Jo, r Jinyoung Chun, Kyojin Ku, S. K.; Hyung Ik Lee, In-Sik Nam, S. Y.; , Kisuk Kang, and J. L. Advanced Hybrid Supercapacitor Based on a Mesoporous Niobium Pentoxide/Carbon as High- Performance Anode. *ACS Nano* **2014**, *8* (9), 8968–8978.

(26) Lim, E.; Kim, H.; Jo, C.; Chun, J.; Ku, K.; Kim, S.; Lee, H. I.; Nam, I.-S.; Yoon, S.; Kang, K.; Lee, J. Advanced Hybrid Supercapacitor Based on a Mesoporous Niobium Pentoxide/carbon as High-Performance Anode. *ACS Nano* **2014**, *8* (9), 8968–8978.

(27) Li, G.; Wang, X.; Ma, X. Nb2O5-Carbon Core-Shell Nanocomposite as Anode Material for Lithium Ion Battery. *J. Energy Chem.* **2013**, *22* (3), 357–362.

(28) De Volder,Michael F. L. Sameh H. Tawfick, R. H. B. and; Hart, A. J.; De Volder, M. F. L.; Tawfick, S. H.; Baughman, R. H.; Hart, A. J. Carbon Nanotubes : Present and Future Commercial Applications. *Science (80-.).* **2013**, *339* (6119), 535–539.

(29) Liu, J.; Tang, S.; Lu, Y.; Cai, G.; Liang, S.; Wang, W.; Chen, X. Synthesis of Mo2N Nanolayer Coated MoO2 Hollow Nanostructures as High-Performance Anode Materials for Lithium-Ion Batteries. *Energy Environ. Sci.* **2013**, *6* (9), 2691.

(30) Wang, Y. Q.; Gu, L.; Guo, Y. G.; Li, H.; He, X. Q.; Tsukimoto, S.; Ikuhara, Y.; Wan, L. J. Rutile-TiO 2 Nanocoating for a High-Rate Li 4Ti 5O 12 Anode of a Lithium-Ion Battery. *J. Am. Chem. Soc.* **2012**, *134* (18), 7874–7879.

(31) Choi, D.; Kumta, P. N. Chemically Synthesized Nanostructured VN for Pseudocapacitor Application. *Electrochem. Solid-State Lett.* **2005**, *8* (8), A418.

(32) Choi, D.; Kumta, P. N. Nanocrystalline TiN Derived by a Two-Step Halide Approach for Electrochemical Capacitors. *J. Electrochem. Soc.* **2006**, *153* (12), A2298.

(33) Cui, G.; Gu, L.; Thomas, A.; Fu, L.; van Aken, P. a; Antonietti, M.; Maier, J. A Carbon/titanium Vanadium Nitride Composite for Lithium Storage. *Chemphyschem* **2010**, *11* (15), 3219–3223.

(34) Choi, D.; Blomgren, G. E.; Kumta, P. N. Fast and Reversible Surface Redox Reaction in Nanocrystalline Vanadium Nitride Supercapacitors. *Adv. Mater.* **2006**, *18* (9), 1178–1182.

(35) Zhou, X.; Chen, H.; Shu, D.; He, C.; Nan, J. Study on the Electrochemical Behavior of Vanadium Nitride as a Promising Supercapacitor Material. *J. Phys. Chem. Solids* **2009**, *70* (2), 495–500.

(36) Cheng, F.; He, C.; Shu, D.; Chen, H.; Zhang, J.; Tang, S.; Finlow, D. E. Preparation of Nanocrystalline VN by the Melamine Reduction of V2O5 Xerogel and Its Supercapacitive Behavior. *Mater. Chem. Phys.* **2011**, *131* (1–2), 268–273.

(37) Lu, X.; Yu, M.; Zhai, T.; Wang, G.; Xie, S.; Liu, T.; Liang, C.; Tong, Y.; Li, Y. High Energy Density Asymmetric Quasi-Solid-State Supercapacitor Based on Porous Vanadium Nitride Nanowire Anode. *Nano Lett.* **2013**, *13* (6), 2628–2633.

(38) Lu, X.; Wang, G.; Zhai, T.; Yu, M.; Xie, S.; Ling, Y.; Liang, C.; Tong, Y.; Li, Y. Stabilized TiN Nanowire Arrays for High-Performance and Flexible Supercapacitors. *Nano Lett.* **2012**, *12* (10), 5376–5381.

(39) Cui, H.; Zhu, G.; Liu, X.; Liu, F.; Xie, Y.; Yang, C. Niobium Nitride Nb 4 N 5 as a New High-Performance Electrode Material for Supercapacitors. *Adv. Sci.* **2015**, *2* (12), 1500126.

(40) Park, H.-C.; Lee, K.-H.; Lee, Y.-W.; Kim, S.-J.; Kim, D.-M.; Kim, M.-C.; Park, K.-W. Mesoporous Molybdenum Nitride Nanobelts as an Anode with Improved Electrochemical Properties in Lithium Ion Batteries. *J. Power Sources* **2014**, *269*, 534–541.

(41) Wang, P.; Wang, R.; Lang, J.; Zhang, X.; Chen, Z.; Yan, X. Porous Niobium Nitride as a Capacitive Anode Material for Advanced Li-Ion Hybrid Capacitors with Superior Cycling Stability. *J. Mater. Chem. A* **2016**, *4*, 9760–9766.

(42) Dong, C.; Wang, X.; Liu, X.; Yuan, X.; Dong, W.; Cui, H.; Duan, Y.; Huang, F. In Situ Grown Nb $_4$ N $_5$ Nanocrystal on Nitrogen-Doped Graphene as a Novel Anode for Lithium Ion Battery. *RSC Adv.* **2016**, *6* (84), 81290–81295.

(43) Marchand, R.; Tessier, F.; DiSalvo, F. J. New Routes to Transition Metal Nitrides: And Characterization of New Phases. *J. Mater. Chem.* **1999**, *9* (1), 297–304.

(44) Oya, G. I.; Onodera, Y. Transition Temperatures and Crystal Structures of Single-Crystal and Polycrystalline NbNx Films. *J. Appl. Phys.* **1974**, *45* (3), 1389–1397.

(45) A, E. S. S.; Terao, N. New Phases of Niobium Nitride. *J. Less-Common Met.* **1970**, *23* (1971), 159–169.

(46) Matylitskaya, V. a.; Bock, W.; Thoma, K.; Kolbesen, B. O. Oxidation and Nitridation of Niobium Films by Rapid Thermal Processing. *Microchim. Acta* **2006**, *156* (1–2), 33–37.

(47) Schwartz, V.; Oyama, S. T. Study of Niobium Oxynitride : Synthesis , Characterization , and Reactivity. **1997**, *4756* (15), 3052–3059.

(48) Zhou, X.; Shang, C.; Gu, L.; Dong, S.; Chen, X.; Han, P.; Li, L.; Yao, J.; Liu, Z.; Xu, H.; Zhu, Y.; Cui, G. Mesoporous Coaxial Titanium Nitride-Vanadium Nitride Fibers of Core-Shell Structures for High-Performance Supercapacitors. *ACS Appl. Mater. Interfaces* **2011**, *3* (8), 3058–3063.

(49) Gao, B.; Xiao, X.; Su, J.; Zhang, X.; Peng, X.; Fu, J.; Chu, P. K. Synthesis of Mesoporous Niobium Nitride Nanobelt Arrays and Their Capacitive Properties. *Appl. Surf. Sci.* **2016**, No. 383, 57–63.

(50) Hubbard, C. R.; Snyder, R. L. RIR -Measurement and Use in Quantitative XRD. *Powder Diffr.* **1988**, *3* (2), 74–77.

(51) Snyder, R. L. The Use of Reference Intensity Ratios in X-Ray Quantitative Analysis. *Powder Diffr.* **1992**, *7* (4), 186–193.

(52) Hillier, S. Accurate Quantitative Analysis of Clay and Other Minerals in Sandstones by XRD: Comparison of a Rietveld and a Reference Intensity Ratio (RIR) Method and the

Importance of Sample Preparation. *Clay Miner.* **2000**, *35* (1), 291–291.

(53) Alfonso, J. E.; Buitrago, J.; Torres, J.; Marco, J. F.; Santos, B. Influence of Fabrication Parameters on Crystallization, Microstructure, and Surface Composition of NbN Thin Films Deposited by Rf Magnetron Sputtering. *J. Mater. Sci.* **2010**, *45* (20), 5528–5533.

(54) Thiede, T. B.; Parala, H.; Reuter, K.; Passing, G.; Kirchmeyer, S.; Hinz, J.; Lemberger, M.; Bauer, A. J.; Barreca, D.; Gasparotto, A.; Fischer, R. A. Deposition of Niobium Nitride Thin Films from Tert-Butylamido-Tris- (Diethylamido)-Niobium by a Modified Industrial MOCVD Reactor. *Chem. Vap. Depos.* **2009**, *15* (10–12), 334–341.

(55) Robinson, K. S.; Sherwood, P. M. A. X-Ray Photoelectron Spectroscopic Studies of the Surface of Sputter Ion Plated Films. *Surf. Interface Anal.* **1984**, *6* (6), 261–266.

(56) Fregonara, G.; Fregonara, G.; Trasatti, S.; Trasatti, S. "Inner" and "Outer" Active Surface Electrodes. *Electrochim. Acta* **1990**, *35* (1), 263–267.

(57) Marcano, D. C.; Kosynkin, D. V.; Berlin, J. M.; Sinitskii, A.; Sun, Z.; Slesarev, A.; Alemany, L. B.; Lu, W.; Tour, J. M. Improved Synthesis of Graphene Oxide. *ACS Nano* **2010**, *4* (8), 4806–4814.

(58) Lai, C. H.; Ashby, D.; Moz, M.; Gogotsi, Y.; Pilon, L.; Dunn, B. Designing Pseudocapacitance for Nb2O5/Carbide-Derived Carbon Electrodes and Hybrid Devices. *Langmuir* **2017**, *33* (37), 9407–9415.

CHAPTER 3

Mesoporous MoO_2 Thin Films for Pseudocapacitive Li^+ storage: Effect of Crystallinity and Porous Structure

3.1 Introduction

Pseudocapacitive charge storage is emerging as an exciting alternative technology to traditional Li-ion batteries due to their higher power density and longer cycle life, and can be found in many applications ranging from portable electronics to hybrid vehicles. The fundamental difference between pseudocapacitors and Li-ion batteries lies in the ionic diffusion process. Li-ion batteries generally involve faradaic (i.e. charge transfer) reactions with solid-state ionic diffusion (10^{-10} - 10^{-15} cm^2/s) through the bulk material, which intrinsically leads to slow charging and discharging times.[1,2] In contrast, pseudocapacitors involve faradaic reactions at or near the surface where the fundamental kinetic barriers associated with solid-state diffusion processes are avoided, making them capacitive in nature.[3–6] Another class of energy storage devices that utilize the capacitive mechanism are electrical double layer capacitors (EDLCs). EDLCs store energy by physically adsorbing ions at the interface between electrode and electrolyte. EDLCs store energy by physically adsorbed ions at the interface between electrode and electrolyte. They are intrinsically fast as no charge transfer is involved, however, the amount of energy stored is limited and highly dependent on surface area.[6,7] Overall, pseudocapacitors can potentially combine the energy density of batteries with the power density of EDLCs, and it is for this reason, they have been widely researched as a next-generation energy storage device.

Molybdenum dioxide (MoO_2) has been studied as a promising negative electrode material for l ithium ion batteries because of its low metallic resistivity (8.8×10^{-5} Ω cm at 300 K) , high capacity (840 mAh/g when cycled to 0 V vs. Li/Li^+), and high density (6.5 g/cm^3).[8,9] Li^+ ion-based charge storage in MoO_2 occurs by two different mechanisms: (1) Li^+ ion insertion/deinsertion between 1.0 to 3.0 V (vs. Li/Li^+), and (2) a conversion reaction below 1 V(vs. Li/Li^+).[10]

$$xLi + MoO_2 = Li_xMoO_2,\ 0 < x < 0.98,\ C = 210\ mAh/g \quad (1)$$

$$Li_{0.98}MoO_2 + 3.02Li = 2Li_2O + Mo,\ C = 630\ mAh/g \quad (2)$$

Although the conversion reaction in MoO_2 leads to a much higher theoretical capacity compared to the 1-electron insertion/deinsertion process, the conversion process is generally slow due to a large volume expansion during the conversion.[11,12] Furthermore, the transition from MoO_2 to Mo is kinetically hindered and destroys the parent crystalline atomic structure completely in an irreversible manner.[13,14]

On the other hand, the one-electron transfer intercalation process is much less kinetically hindered. Monoclinic MoO_2 (space group of P21/c(14)) has a tunnel structure framework possessing a rutile-type structure which consists of MoO_6 octahedra linkages that form one dimensional channels along the a-axis where Li-ions can be inserted and extracted reversibly.[15] Thus, the intercalation process is a more promising charge storage mechanism for pseudocapacitive energy storage.

Various structures and morphologies of MoO_2, such as nanorods,[8] nanobelts,[16] nanosheets,[17] nanowires,[18] nanotubes,[19,20]nanoparticles,[12,21] porous structure[22–24] and hierarchical architectures[25] have been reported using high temperature vapor deposition, thermal reduction, electrochemical deposition and hydrothermal synthesis. However, most of them are studied as a conversion-type electrode and are limited by the size dimension to be used as a fast charging electrode. MoO_2

nanoparticles used as intercalation hosts with diameters of 15-20 nm diameters were reported to show pseudocapacitive behavior with 120 mAh/g at 10C.[12] However, the high amount of surface MoO_3 coating results in poor electrical connection between individual nanoparticles, which hinders the charge storage at faster rates. Growing MoO_2 directly onto a conductive scaffold such as graphene[12,26] can limit the effect of surface oxide, nonetheless, it involves extra reagents and procedures and is not economically scalable.

Alternatively, a mesoporous network can alleviate the impact of surface oxide by utilizing an interconnected electrically conductive backbone. In fact, mesoporous structure has been widely incorporated in energy storage materials, such as TiO_2,[27] $LiCoO_2$,[28] $LiMn_2O_4$,[29] Nb_2O_5,[30] MoS_2.[31] It offers several advantages: (1) high capacity from the large amount of surface redox sites due to the high surface area; (2) short solid-state diffusion length for both ions and electrons due to the nanosized walls; and (3) efficient access to electrolyte through the mesopore channels. These qualities are beneficial to achieving pseudocapacitive energy storage. A template method allows precise control of porosity and pore size, which can affect the amount of surface sites as well as the solid diffusion length, and further impact the capacity and kinetics of a system.[32–37] Stucky *et al.* has previously synthesized mesoporous MoO_2 using SBA 15 as a hard template.[22,38] Ordered porous nanostructures and very high capacity were obtained when discharged to 0.1 V *vs.* Li/Li^+. Up to 1800 mAh/g capacity was achieved by utilizing Li^+ storage sites at the interface of $LixMoO_2$ nano-domains and forming Li-rich amorphous phase,[22] yet the kinetics of mesoporous MoO_2 have not been discussed.

Crystallinity also have a significant impact on charge storage. Previous researches[39,40] have shown that crystalline materials outperformed amorphous ones due to the extra capacity arising from intercalation pseudocapacitance in crystalline materials, whereas the capacity in amorphous

samples were limited to surface redox pseudocapacitance. Moreover, the intercalation pseudocapacitive contribution often occurs at short timescales where diffusion-controlled process is minimal. Different crystalline phases also provide different Li^+ transport pathways, which further influence the capacity and rate capability.[40] and High temperature calcination is a typical approach to enhance the crystallinity[41–43] and thus improve the electrochemical performance.

In this work we fabricate ordered mesoporous MoO_2 (mp-MoO_2) thin film electrodes to study the correlation between their pseudocapacitive behaviors and their crystallinity and porous structure. Thin film format is chosen to eliminate the need for carbon additives or binders in order to isolate the pseudocapacitive properties of nanostructured MoO_2. Evaporation induced self-assembly (EISA) of block copolymer templated sol-gel type precursors is a well-established method to synthesize a variety of ordered mesoporous materials with uniform, well-defined pore sizes.[39,44–48] This synthesis method leads to nanocrystalline domains which are directly connected to each other, allowing intercalation pseudocapacitance with little interfacial resistance. The ability to control the pore size and pore-size distribution further enables optimized electrolyte diffusion.[49] In this report, several mesoporous architectures were prepared under different heating condition to vary the crystallinity and porous structure. The nanosctructures are correlated to the pseudocapacitive properties using a detailed cyclic voltammetric analysis that quantitatively decouples capacitive-driven and diffusion-controlled contributions to overall charge storage. This analysis allows the understanding of how nanoscale architecture is related to pseudocapacitive energy storage.

3.2 Results and Discussion

3.2.1 Materials characterization

Ordered mesoporous MoO_2 thin films (mp-MoO_2) were synthesized through evaporation induced self-assembly (EISA) of molybdenum precursors and an amphiphilic block copolymer (poly(ethylene oxide-block-butylene oxide), PEO-b-PBO), followed by a heat treatment in N_2/H_2 (95 vol%/5 vol%) to remove the template and crystalize the structure. PEO-b-PEO was used because its high oxygen content allows the removal of template in the reducing atmosphere without forming MoO_3. Retaining the porous structure during the conversion from MoO_3 to MoO_2 can be challenging due to the big volume change (density = 4.69 g/cm³ for MoO_3 vs 6.79 g/cm³ for MoO_2) and structural evolution (orthorhombic to monoclinic). Therefore, a direct heat treatment to remove template and crystalize the structure at the same time can help maintain the mesoporous structure in mp-MoO_2.

To examine the porous structure, we have utilized scanning electron microscopy (SEM), transmission electron microscopy (TEM), small angle X-ray diffraction and porosimetry methods. Figures 3.1a – 3.1c shows the SEM image of calcined mp-MoO_2 that shows the surface of an ordered porous structure with ~10 nm pores and ~10 nm walls. As the calcination temperature increases, the wall thickness slightly increases due to the grain growth. Figures 3.2a – 3.2c show the toluene adsorption/desorption isotherms and the derived pore size distribution. The isotherms show a large hysteresis between adsorption and desorption of toluene, which is indicative of a mesoporous structure. The porosity calculated from the volumes adsorbed is 31%, 26% and 18%, respectively, for mp- MoO_2 calcined at 350 ℃, 600 ℃ and 700 ℃. Using the adsorption isotherm the average pore size of the mp-MoO_2 thin film is calculated to be 8.5 nm, 7.8 nm and 6.5 nm, respectively. The gradual reduction in porosity and pore size is due to the increasing temperature for calcination. The porous structure shrinks more at higher temperature. This value is in excellent agreement with the SEM data in Figure 3.1a – 3.1c. TEM image (Figure 3.1g) also corroborates

the porous structure in MoO_2 mesoporous thin film calcined at 600 ℃. Synchrotron-based grazing incidence small angle scattering (GISAX) (Figures 3.1h and 3.1j) shows X-ray diffraction arcs along the q_{xy} direction for mp-MoO_2-600 and mp-MoO_2-700, respectively, demonstrating that these thin films have ordered porosity in the plane of the substrate. The in-plane repeating distances calculated from q_{xy} (when $q_z \rightarrow 0$) in Figures 3.1h and 3.1j are 22 nm and 18 nm which matches the observation from SEM. These porous structure provides high surface area and electrolyte accessibility for high charge storage, and the nanoscale pore wall ensures short solid-state diffusion length.

The crystal structure mp-MoO_2 was analyzed using high-resolution TEM (HRTEM) and synchrotron-based grazing incidence wide angle X-ray scattering (GIWAX). In an HRTEM image (Figure 3.2a), the lattice spacing of monoclinic MoO_2 can be observed. Figure 3.2b shows the 1-D GIWAX patterns integrated from the 2-D images of mp-MoO_2-350, mp-MoO_2-600 and mp-MoO_2-700. They all match JCPDS No. 32-0671 for monoclinic MoO_2. The monoclinic phase is known to be a metallic conductor[15,23] due to the Mo-Mo pairing along the Mo atom chains. The unique structure also allows potential fast Li^+ conduction in octahedral interstitial sites in the "tunnels" between the Mo chains[50]. Although the three samples all display diffraction peaks for monoclinic phase, the sample prepared under higher temperature was more crystalline based on the diffraction intensities. Based on peak width, we can calculate the grain size for them to be 11 nm, 13 nm and 18 nm respectively. We believe the grain size plays an important role in determining pseudocapacitive charge storage behaviors as discussed later.

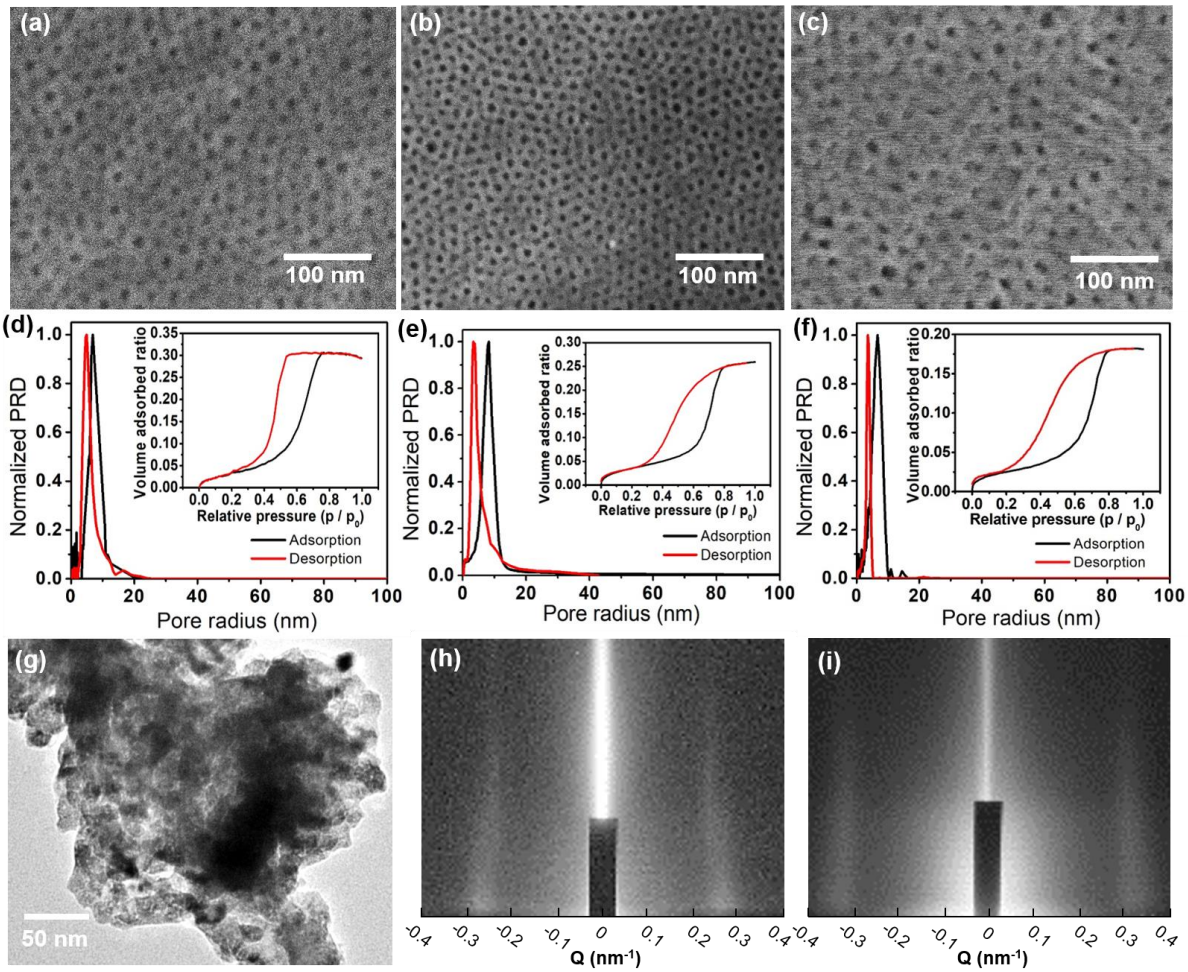

Figure 3.1. Structural characterization of mesoporous MoO_2 thin films. (a-c) SEM images of the surface of a MoO_2 mesoporous thin films calcined at (a) 350 ℃, (b) 600 ℃ and (c) 700 ℃. All structures are porous. (d-f) Toluene adsorption-desorption isotherms and corresponding pore size distribution data obtained from the isotherms for MoO_2 mesoporous thin films calcined at (d) 350 ℃, (e) 600 ℃ and (f) 700 ℃. As the calcination temperature increases, grain growth in the structure leads to lower porosity and smaller pore size. (g) TEM of mp-MoO_2-600. (h) and (i) Synchrotron grazing incidence small angle x-ray scattering image of MoO_2 calcined at (h) 600 ℃ and (i) 700 ℃. The in-plane repeat distance is 22 nm and 18nm, respectively.

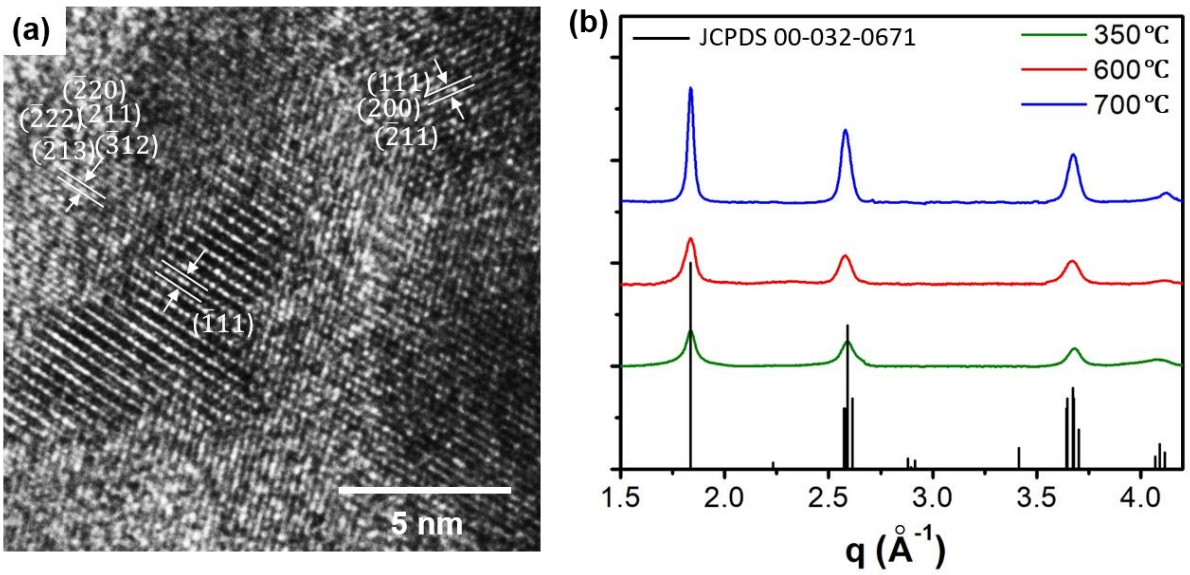

Figure 3.2. Crystal structure of mesoporous MoO_2 thin films. (a) HRTEM image of a 600 ℃ calcined MoO_2 mesoporous thin film. Lattice spacing of monoclinic MoO_2 can be observed. (b) Synchrotron grazing incidence wide angle x-ray scattering pattern of MoO_2 calcined at different temperatures. The peaks are assigned to monoclinic MoO_2 (JCPDS No. 032-0671).

X-ray photoelectron spectroscopy (XPS) measurements were performed to study the chemical composition and oxidation state of the material. Figure 3.3a shows high resolution XPS traces for Mo 3d scan. The Mo 3d peak is composed of 2 sets of the spin-orbit doublet corresponding to Mo $3d_{3/2}$ and Mo $3d_{5/2}$. The peaks at 229.8 eV and 233.0 eV are attributed to Mo^{4+} and those at 231.7 eV and 234.9 eV are attributed to Mo^{6+}. Since the probing depth of XPS is usually within 5 nm of the surface, this indicates the surface of MoO_2 is mostly MoO_3. Figure 3.3b shows XPS traces for Mo 3d after Ar etching, where the surface layer was removed. The Mo^{4+}/Mo^{6+} ratio calculated from the peak area changed from 0.29 to 2.2, revealing that the majority of the nanostructure backbone is composed of MoO_2. Despite the surface oxidation, the mesoporous framework consists of interconnected conductive MoO_2 grains and so the overall resistance through the network should be low.

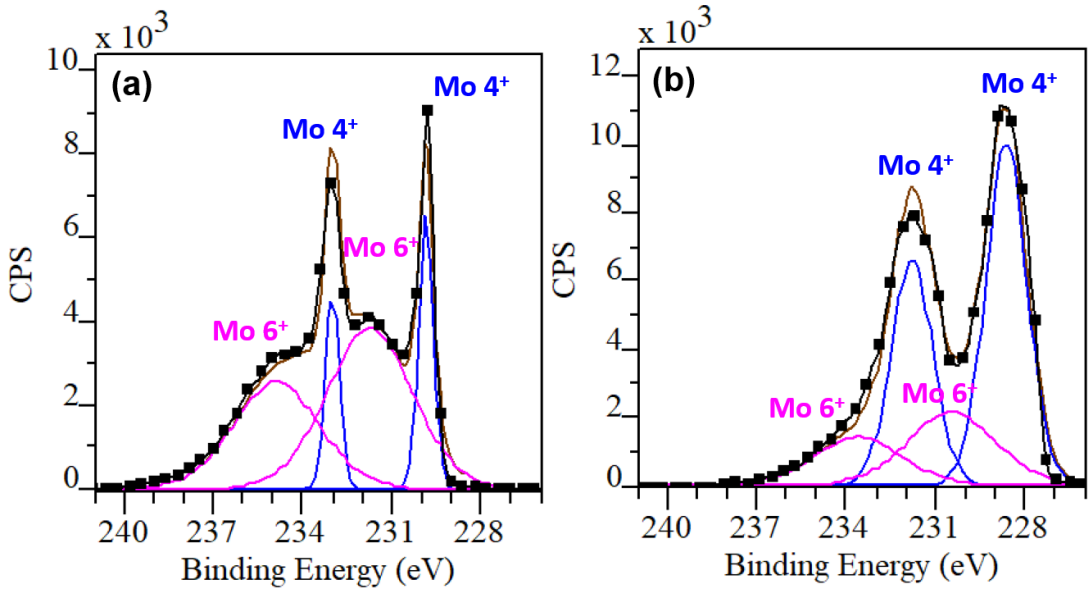

Figure 3.3. X-ray photoelectron spectra obtained to analyze the surface oxidation state of mesoporous MoO_2 (a) pristine and (b) after Ar ion etching.

3.2.2. Electrochemistry

Mp-MoO_2 films were cycled in a 3-neck flooded cell between 1.1 and 3 V *vs*. Li/Li^+ to realize the one-electron involved intercalation process. As the electrochemical activity highly depends on the crystallinity of the structure, three samples made at different temperatures were compared: 350 ℃, 600 ℃ and 700 ℃. Figure 3.4 shows the cyclic voltammograms (CV) of these electrodes under different scan rate varying from 1 mV/s to 100 mV/s. All three samples display the signature redox peaks at 1.27 V and 1.55 V (Li intercalation) and 1.34 V and 1.66 V *vs*. Li/Li^+ (Li extraction) for monoclinic MoO_2. Those peaks correspond to the phase transitions from the monoclinic (at low Li content) to orthorhombic and back to monoclinic (at high Li content)[15]. The peaks are sharper in the samples prepared at the higher temperature, indicating a more crystalline structure, where phase transitions take place over a smaller range of voltage. In general, as the scan rate increases, the shift between the anodic and cathodic pair of peaks increase as it gets more difficult

to efficiently access the active sites during the shorter time frame. Nevertheless, the higher temperature crystalized structure displays smaller peak shift and polarization effect. This suggests that the sample prepared under higher temperature has more structural periodicity, which allows better intercalation through the tunnel sites.

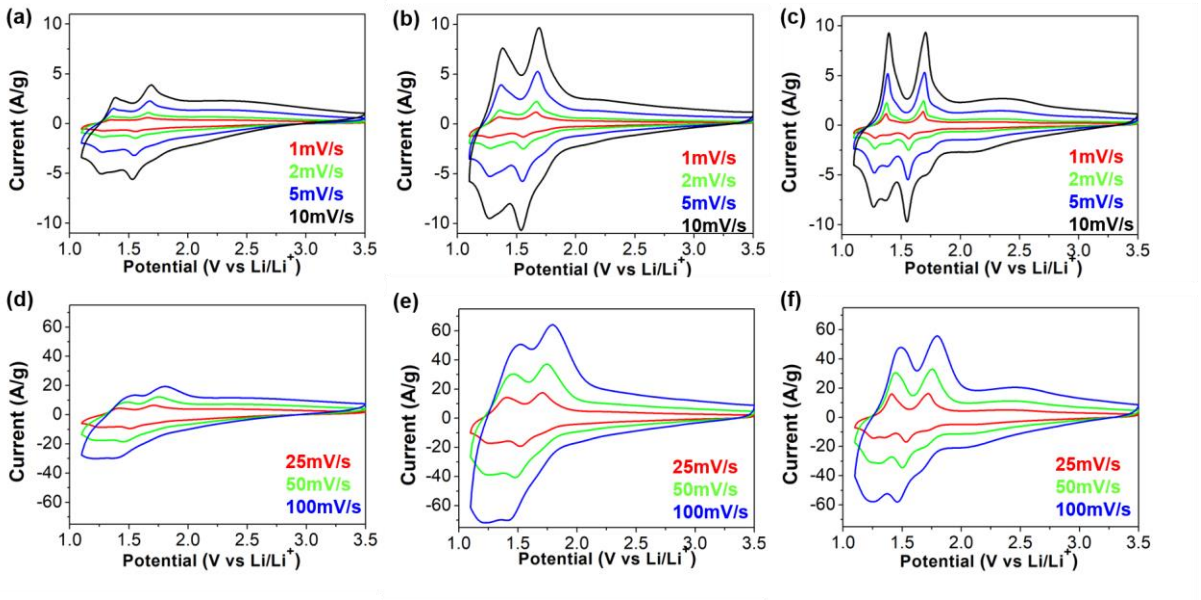

Figure 3.4. Cyclic voltammogram of mesoporous MoO_2 thin films calcined at different temperatures. (a) (d) mp-MoO_2-350 (b) (e) mp-MoO_2-600 and (c) (f) mp-MoO_2-700. CVs were taken at different scan rate. (a)-(c) 1 mV/s to 10 mV/s and (d)-(f) 25 mV/s to 100 mV/s. As the temperature increases, the redox charaterisitic peaks are more defined, the voltage separation is smaller.

The rate capabilities of mp-MoO_2-350, mp-MoO_2-600 and mp-MoO_2-700 were analyzed with cyclic voltammograms at different scan rates. Figure 3.5a and 3.5b plot the specific capacity in the three samples as a function of scan rate and charge time, respectively. The data indicates that mp-MoO_2-600 has the highest initial capacity, 253 mAh/g at 1 mV/s. Mp-MoO_2-700 has a similar initial capacity of 239 mAh/g. The capacities are higher than theoretical one-electron insertion capacity 209 mAh/g, which can be attributed to electrical double layer capacitance from the high surface area of mesoporous structure . Mp-MoO_2-350 has only 200 mAh/g at 1 mV/s, most likely because not all the redox sites are accessible due to the low crystallinity. Mp-MoO_2-350 also has

the worst rate capability due to the same reason. The defects or amorphous region in the structure prevent utilization of 1-D tunnel sites for intercalation. Mp-MoO_2-600 has the highest capacity retention at fast scan rates, with over 60% (164 mAh/g) of the initial capacity accessed within 24 seconds. This could be the result of an ideal nanostructure consisting of interconnected nanocrystals with short ion diffusion lengths and good electrolyte accessibility combined with high electrical conductivity in the connected backbone. Mp-MoO_2-700 has slightly worse kinetics and capacity. This is probably due to the larger grain size in Mp-MoO_2-700 which leads to slightly thicker wall for solid-state diffusion.

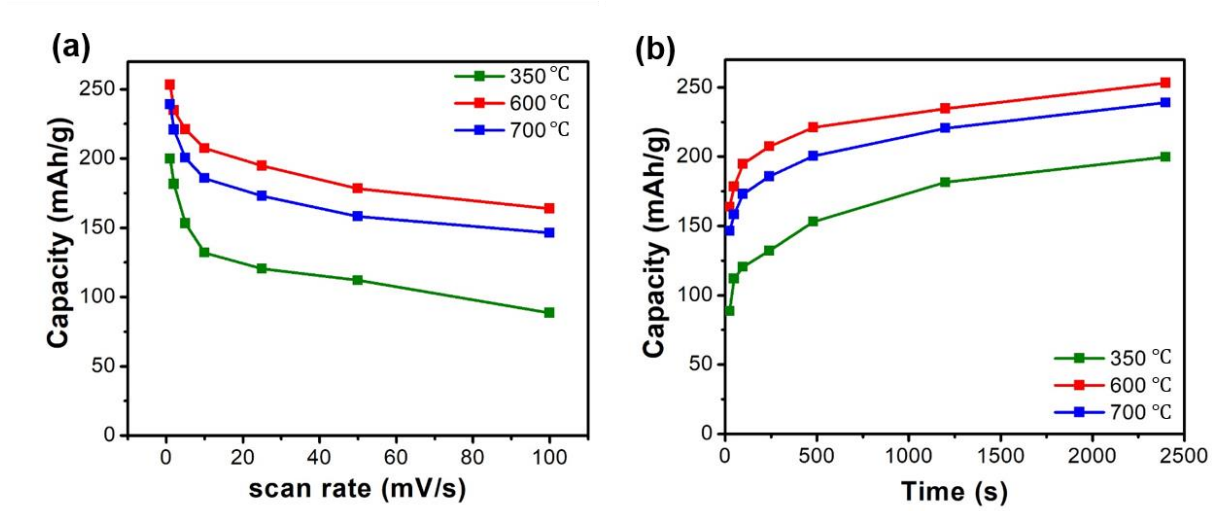

Figure 3.5. Rate capabilities of mesoporous MoO_2 thin films calcined at different temperatures. (a) specific capacity as a function of scan rate and (b) specific capacity as a function of scan time obtained from CV. Mp-MoO_2-600 displays best kinetic behavior with more than 60% capacity retention at 100 mV/s or within 24 seconds.

To better understand the effect of crystallinity on electrochemical performance of MoO_2, we analyzed the dependence of peak currents on scan rates. Generally, the current (i) varies with the scan rate (v) according to the following equation:

$$i = av^b \quad (3)$$

where a and b are constants. The value of b can be between 0.5 and 1, with a b-value of 0.5 indicating a diffusion-controlled process and a b-value of 1 representing capacitive behavior[30,51] at different scan rate. Figure 3.6a – 3.6c present plots of log(i) versus log(v) from 1 to 20 mV/s for the four redox peaks in each sample. Overall, mp-MoO_2-600 calcined sample has the highest b-value while mp-MoO_2-350 has the lowest. The low b-values in mp-MoO_2-350 can be attributed to the low crystallinity of the structure. Existence of defects or amorphous areas can block the efficient Li^+ intercalation through the 1D tunnel. Interestingly, mp-MoO_2-700 has lower b-values than mp-MoO_2-600 despite the higher crystallinity. This is most likely due to the larger grain size in mp-MoO_2-700, which increases the solid-state diffusion length and therefore causes a higher diffusion controlled capacity contribution. On the other hand, the mp-MoO_2-600 sample having better crystallinity than mp-MoO_2-350 and thinner walls than mp-MoO_2-700 showed the best electrochemical performances among the three samples.

The difference in level of pseudocapacitance in the three samples can also be analyzed with a different method in which the potential capacitive and diffusion-controlled regions are determined in the CV plots. The current response that is measured due to sweeping the voltage is considered to be comprised of both capacitive currents (which vary as k_1v) and diffusion-controlled current (which vary as $k_2v^{0.5}$), as shown in equation (4).

$$i = k_1v + k_2v^{0.5} \quad (4)$$

Here i is the current, and v is the scan rate.

Figure 3.6d – 6f show this kinetic analysis of each sample at a slow sweep rate of 1 mVs^{-1}. Analysis using equation (4) indicates that 71% of the current in mp-MoO_2-600, and therefore the capacity, is capacitive, in contrast to the 65% in mp-MoO_2-700 and 54% in mp-MoO_2-350. Particularly, the voltage regions near the cathodic peaks in the intercalation process are more

diffusion controlled than the extraction process. This suggests that the phase transition in the intercalation process is the rate-limiting step for MoO_2 cycling. Overall, both b-value and k_1k_2 kinetic analysis indicate that the mp-MoO_2-600 is the most capacitor-like, due to a combination of high crystallinity and small grain size. This capacitive behavior allows mp-MoO_2-600 to have the best kinetics at fast rates.

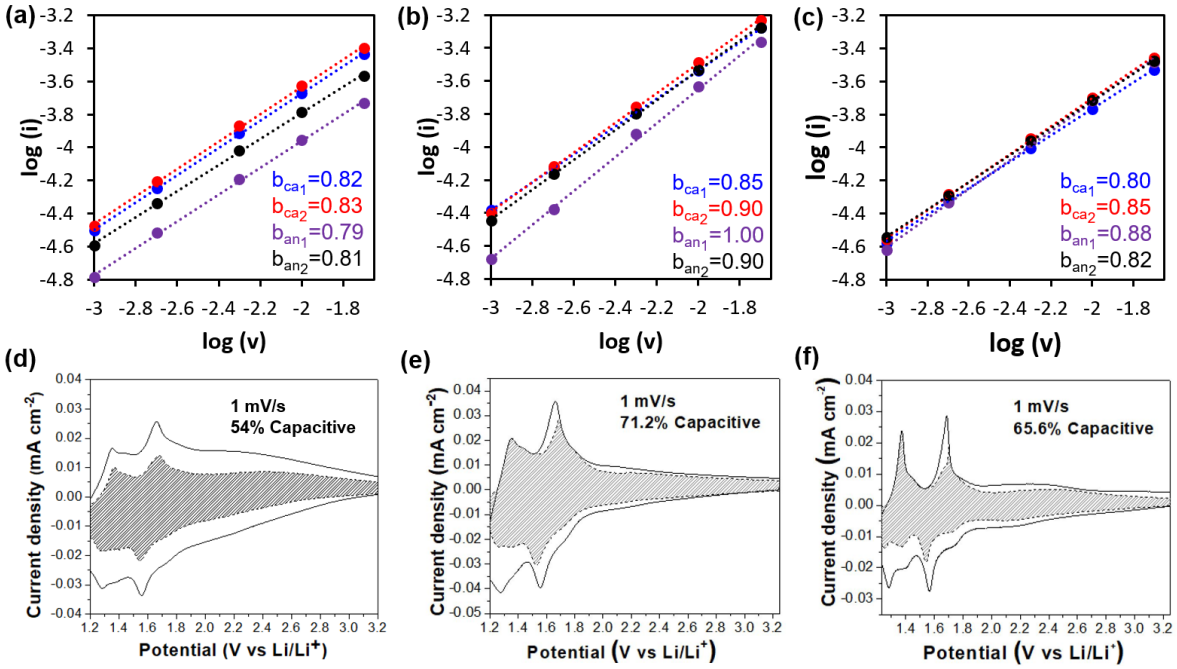

Figure 3.6. Analysis of pseudocapactive behaviors in mesoporous MoO_2 thin films calcined at different temperatures. (a)-(c) Plots of log(peak current) vs log(sweep rate) used to obtain b-values for MoO_2 redox peaks using CV scanned between voltage range 1.1 – 3.5 V vs Li/Li+ and scan rate 1-20 mV/s. (a) mp-MoO_2-350, (b) mp-MoO_2-600 and (c) mp-MoO_2-700. (d)-(f) Capacitive charge storage contributions for mp-MoO_2 cycled at 1 mV/s calculated using the method described in Equation (4) for (d) mp-MoO_2-350, (e) mp-MoO_2-600 and (f) mp-MoO_2-700. 600 °C calcined film has highest b-values and capacitive contribution, suggesting pseudocapacitive behavior.

3.3 Conclusions

We have demonstrated that ordered porous MoO_2 can be synthesized via a block copolymer template method. The porosity, pore size and crystallinity can be controlled with different heating conditions. GISAXS, SEM, TEM and porosimetry confirm ordered porous structure with ~30%

porosity and 15-20 nm pore size. GIWAXS reveal all three samples have monoclinic MoO_2 crystalline phase, which is known to be electrically conductive, and 10-20 nm grain size. The combination of these structural factors leads to the fast kinetics for Li^+ intercalation pseudocapacitance. Three samples prepared at different temperature are compared and their performance is correlated to the structure feature. Mp-MoO_2-600 has the optimal combination of high crystallinity and thin walls that provide short ion diffusion path. Over 60% (164 mAh/g) of the capacity can be accessed in only 24 seconds in mp-MoO_2-600 as a result of a high percentage capacitive charge storage. Kinetic analysis using cyclic voltammogram further confirms the dominant pseudocapacitive behavior in mp-MoO_2-600 with b values of 0.9-1 and a 71% pseudocapacitve contribution at 1 mV/s. Overall, we have demonstrated that mp-MoO_2 is a pseudocapative material with fast kinetics. We foresee that mp-MoO_2 can be scaled up with typical slurry loading and achieve good kinetics on account of electrically conductive interconnected network and ideal nano architecture for electrolyte accessibility and short ion diffusion length.

3.4 Experimental Methods

3.4.1 Materials

The following materials were obtained from commercial suppliers and used without further purification: molybdenum (V) chloride (99.6% metal basis, Alfa Aesar), poly(butylene oxide)-block-poly(ethylene oxide) (PBO(5000)-b-PEO(6500), Mn = 11500, PDI=1.06-1.15, Advanced Polymer Materials Inc).

3.4.2 Synthesis of MoO_2

In a typical synthesis, 0.015 g PEO-b-PBO was first dissolved in 2 mL ethanol. Then 0.2 g $MoCl_5$ was added. The resulting sol was stirred for 2 h prior to film deposition. Thin films were deposited via dip-coating on polar substrates such as silicon and platinum coated Si (3 nm Ti-150

nm Pt- 360 nm SiO_2- Si). Optimal conditions included 4% relative humidity and a constant withdrawal rate of 3 mm/s. The films were aged at 180 °C for 12 h prior to template removal to prevent loss of mesoscale order during the course of template removal and crystallization. Films were calcined using a 5 °C/min ramp to selected temperatures (350 °C, 600 °C and 700 °C) in 5%/95% H_2/N_2 reducing atmosphere to yield the crystalline, porous MoO_2.

3.4.3 Characterizations

Scanning Electron Microscopy (SEM) images were obtained using a model JEOL JSM-6700F field emission electron microscope with 5 kV accelerating voltage and secondary electron detector configuration. Transmission Electron Microscopy (TEM) images were obtained using a Tecnai T12 Quick Cryo-electron microscope at an accelerating voltage 120 kV and a Gatan 2k×2k CCD detector. Ellipsometric porosimetry was performed on a PS-1100 instrument from Semilab using toluene as the adsorbate. The instrument used a UV-visible CCD detector adapted to a grating spectrograph to analyze the signal reflected by the sample. The light source was a 75 W Hamamatsu Xenon lamp and the measurements were performed in the spectral range from 1.25–4.5 eV. Data analysis was performed using the associated Spectroscopic Ellipsometry Analyzer software with the assumption of cylindrical pores. Two-dimensional small-angle and wide angle X-ray scattering data were collected at the Stanford Synchrotron Lightsource (SSRL) using beamlines 1-5 and 11-3, respectively. Beamline 1-5 was operated at 10.000 KeV using the Rayonix-165 CCD detector. Beamline 11-3 was operated at 12.735 KeV using a MAR345 imaging plate (345 mm diameter). XPS analysis was performed using a Kratos Axis Ultra DLD with a monochromatic Al (Kα) radiation source. The charge neutralizer filament was used to control charging of the sample, a 20 eV pass energy was used with a 0.05 eV step size, and scans were calibrated using the C 1s peak shifted to 284.8 eV. The integrated area of the peaks was found

using the CasaXPS software, and atomic ratios were also found using this software. The atomic sensitivity factors used were from the Kratos library within the Casa software.

3.4.4 Electrochemistry measurements

The as prepared mp-MoO_2 thin films on Pt-coated silicon substrates were used as working electrodes. Electrochemical measurements of these thin film electrodes were carried out in a three-electrode cell with 1M $LiClO_4$ in propylene carbonate as electrolyte, lithium foils used as a counter and reference electrode. The mp-MoO_2 thin films were cycled between 1.1 to 3.0 V (vs. Li/Li^+) to investigate the capacity and kinetics of mp-MoO_2 using an Arbin BT-2000. The films were cycled in galvanostatic mode for the cyclability test with Li. All tests were performed in an argon or nitrogen filled glovebox. Inductively coupled plasma optical emission Spectrometry (ICP-OES) was used to determine thin film masses. The mp-MoO_2 thin films were dissolved in 2.9 M NH_4OH (28~30 wt%, Sigma-Aldrich) aqueous solution overnight at room temperature followed by HotBlock (SC100, Environmental Express) heating at 95 °C to nearly dryness. After adding 2% (v/v) HNO_3 aqueous solution and extracting the analytes at 95 °C for 3 h, the samples were cooled down and analyzed with Inductively Coupled Plasma Optical Emission Spectrometry (ICPE-9000, Shimadzu, Japan). The calculated areal loading from several films is 43 $\mu g/cm^2 \pm 2\ \mu g/cm^2$, which is used for the determination of the mass normalized capacities in this report.

3.5 References

(1) Park, M.; Zhang, X.; Chung, M.; Less, G. B.; Sastry, A. M. A Review of Conduction Phenomena in Li-Ion Batteries. *J. Power Sources* **2010**, *195* (24), 7904–7929.

(2) Balke, N.; Jesse, S.; Morozovska, a N.; Eliseev, E.; Chung, D. W.; Kim, Y.; Adamczyk, L.; García, R. E.; Dudney, N.; Kalinin, S. V. Nanoscale Mapping of Ion Diffusion in a Lithium-Ion Battery Cathode. *Nat. Nanotechnol.* **2010**, *5* (10), 749–754.

(3) Simon, P.; Gogotsi, Y.; Dunn, B. Materials Science. Where Do Batteries End and Supercapacitors Begin? *Science* **2014**, *343* (6176), 1210–1211.

(4) Conway, B. E. TECHNICAL PAPERS' ELECTROCHEMICAL SCIENCE AND TECHNOLOGY Transition from "Supercapacitor" to "Battery" Behavior in Electrochemical Energy Storage. *Electrochem. Sci. Technol.* **1991**, *138* (6), 1539–1549.

(5) Conway, B. E. E.; Birss, V.; Wojtowicz, J. The Role and Utilization of Pseudocapacitance for Energy Storage by Supercapacitors. *J. Power Sources* **1997**, *66* (1–2), 1–14.

(6) Conway, B. E.; Pell, W. G. Double-Layer and Pseudocapacitance Types of Electrochemical Capacitors and Their Applications to the Development of Hybrid Devices. *J. Solid State Electrochem.* **2003**, *7* (9), 637–644.

(7) Zhu, Y.; Murali, S.; Stoller, M. D.; Ganesh, K. J.; Cai, W.; Ferreira, P. J.; Pirkle, A.; Wallace, R. M.; Cychosz, K. A.; Thommes, M.; Su, D.; Stach, E. A.; Ruoff, R. S. Carbon-Based Supercapacitors. *Science (80-.).* **2011**, *332* (6037), 1537–1541.

(8) Guo, B.; Fang, X.; Li, B.; Shi, Y.; Ouyang, C.; Hu, Y. S.; Wang, Z.; Stucky, G. D.; Chen, L. Synthesis and Lithium Storage Mechanism of Ultrafine MoO_2 Nanorods. *Chem. Mater.* **2012**, *24* (3), 457–463.

(9) Shi, Y.; Guo, B.; Corr, S. a.; Shi, Q.; Hu, Y.-S.; Heier, K. R.; Chen, L.; Seshadri, R.; Stucky, G. D. Ordered Mesoporous Metallic MoO_2 Materials with Highly Reversible Lithium Storage Capacity. *Nano Lett.* **2009**, *9* (12), 4215–4220.

(10) Ku, J. H.; Jung, Y. S.; Lee, K. T.; Kim, C. H.; Oh, S. M. Thermoelectrochemically Activated MoO_2 Powder Electrode for Lithium Secondary Batteries. *J. Electrochem. Soc.* **2009**, *156* (8), A688.

(11) Chen, A.; Li, C.; Tang, R.; Yin, L.; Qi, Y. MoO_2-Ordered Mesoporous Carbon Hybrids as

Anode Materials with Highly Improved Rate Capability and Reversible Capacity for Lithium-Ion Battery. *Phys. Chem. Chem. Phys.* **2013**, *15* (32), 13601–13610.

(12) Kim, H.-S.; Cook, J. B.; Tolbert, S. H.; Dunn, B. The Development of Pseudocapacitive Properties in Nanosized-MoO_2. *J. Electrochem. Soc.* **2015**, *162* (5), A5083–A5090.

(13) Fang, X.; Hua, C.; Guo, X.; Hu, Y.; Wang, Z.; Gao, X.; Wu, F.; Wang, J.; Chen, L. Lithium Storage in Commercial MoS2 in Different Potential Ranges. *Electrochim. Acta* **2012**, *81*, 155–160.

(14) David, L.; Bhandavat, R.; Singh, G. MoS_2/graphene Composite Paper for Sodium-Ion Battery Electrodes. *ACS Nano* **2014**, *8* (2), 1759–1770.

(15) Dahn, J. R.; McKinnon, W. R. Structure and Electrochemistry of LixMoO_2. *Solid State Ionics* **1987**, *23* (1–2), 1–7.

(16) Yang, L.; Liu, L.; Zhu, Y.; Wang, X.; Wu, Y. Preparation of Carbon Coated MoO_2 Nanobelts and Their High Performance as Anode Materials for Lithium Ion Batteries. *J. Mater. Chem.* **2012**, *22* (26), 13148.

(17) Ni, J.; Zhao, Y.; Li, L.; Mai, L. Ultrathin MoO_2 Nanosheets for Superior Lithium Storage. *Nano Energy* **2015**, *11*, 129–135.

(18) Mai, L.; Yang, F.; Zhao, Y.; Xu, X.; Xu, L.; Hu, B.; Luo, Y.; Liu, H. Molybdenum Oxide Nanowires: Synthesis & Properties. *Mater. Today* **2011**, *14* (7–8), 346–353.

(19) Zhang, H. J.; Wang, K. X.; Wu, X. Y.; Jiang, Y. M.; Zhai, Y. B.; Wang, C.; Wei, X.; Chen, J. S. MoO_2/Mo_2C Heteronanotubes Function as High-Performance Li-Ion Battery Electrode. *Adv. Funct. Mater.* **2014**, *24* (22), 3399–3404.

(20) Zhang, H. J.; Shu, J.; Wang, K. X.; Chen, X. T.; Jiang, Y. M.; Wei, X.; Chen, J. S. Lithiation Mechanism of Hierarchical Porous MoO_2 Nanotubes Fabricated through One-Step

Carbothermal Reduction. *J. Mater. Chem. A* **2014**, *2* (1), 80–86.

(21) Sun, Y.; Hu, X.; Luo, W.; Huang, Y. Ultrafine MoO_2 Nanoparticles Embedded in a Carbon Matrix as a High-Capacity and Long-Life Anode for Lithium-Ion Batteries. *J. Mater. Chem.* **2012**, *22* (2), 425–431.

(22) Shon, J. K.; Lee, H. S.; Park, G. O.; Yoon, J.; Park, E.; Park, G. S.; Kong, S. S.; Jin, M.; Choi, J. M.; Chang, H.; Doo, S.; Kim, J. M.; Yoon, W. S.; Pak, C.; Kim, H.; Stucky, G. D. Discovery of Abnormal Lithium-Storage Sites in Molybdenum Dioxide Electrodes. *Nat. Commun.* **2016**, *7*, 1–9.

(23) Shi, Y.; Guo, B.; Corr, S. a.; Shi, Q.; Hu, Y.-S.; Heier, K. R.; Chen, L.; Seshadri, R.; Stucky, G. D. Ordered Mesoporous Metallic MoO_2 Materials with Highly Reversible Lithium Storage Capacity. *Nano Lett.* **2009**, *9* (12), 4215–4220.

(24) Fang, X.; Guo, B.; Shi, Y.; Li, B.; Hua, C.; Yao, C.; Zhang, Y.; Hu, Y. S.; Wang, Z.; Stucky, G. D.; Chen, L. Enhanced Li Storage Performance of Ordered Mesoporous MoO_2 via Tungsten Doping. *Nanoscale* **2012**, *4* (5), 1541–1544.

(25) Sun, Y.; Hu, X.; Yu, J. C.; Li, Q.; Luo, W.; Yuan, L.; Zhang, W.; Huang, Y. Morphosynthesis of a Hierarchical MoO_2 Nanoarchitecture as a Binder-Free Anode for Lithium-Ion Batteries. *Energy Environ. Sci.* **2011**, *4* (8), 2870.

(26) Fu, H.; Xu, Z.; Wang, T.; Li, K.; Shen, X.; Li, J.; Huang, J. Rate Behavior of MoO_2/graphene Oxide Lithium-Ion Battery Anodes from Electrochemical Contributions. *J. Electrochem. Soc.* **2018**, *165* (3), 0–8.

(27) Wang, J.; Polleux, J.; Lim, J.; Dunn, B. Pseudocapacitive Contributions to Electrochemical Energy Storage in TiO_2 (Anatase) Nanoparticles. *J. Phys. Chem. C* **2007**, *111* (40), 14925–14931.

(28) Okubo, M.; Hosono, E.; Kim, J.; Enomoto, M.; Kojima, N.; Kudo, T.; Zhou, H.; Honma, I. Nanosize Effect on High-Rate Li-Ion Intercalation in $LiCoO_2$ Electrode. *J. Am. Chem. Soc.* **2007**, *129* (23), 7444–7452.

(29) Lesel, B. K.; Ko, J. S.; Dunn, B.; Tolbert, S. H. Mesoporous $Li_xMn_2O_4$ Thin Film Cathodes for Lithium-Ion Pseudocapacitors. *ACS Nano* **2016**, *10* (8), 7572–7581.

(30) Brezesinski, K.; Wang, J.; Haetge, J.; Reitz, C.; Steinmueller, S. O.; Tolbert, S. H.; Smarsly, B. M.; Dunn, B.; Brezesinski, T. Pseudocapacitive Contributions to Charge Storage in Highly Ordered Mesoporous Group v Transition Metal Oxides with Iso-Oriented Layered Nanocrystalline Domains. *J. Am. Chem. Soc.* **2010**, *132* (20), 6982–6990.

(31) Cook, J. B.; Kim, H. S.; Yan, Y.; Ko, J. S.; Robbennolt, S.; Dunn, B.; Tolbert, S. H. Mesoporous MoS2 as a Transition Metal Dichalcogenide Exhibiting Pseudocapacitive Li and Na-Ion Charge Storage. *Adv. Energy Mater.* **2016**, 1–12.

(32) Brezesinski, K.; Haetge, J.; Wang, J.; Mascotto, S.; Reitz, C.; Rein, A.; Tolbert, S. H.; Perlich, J.; Dunn, B.; Brezesinski, T. Ordered Mesoporous α-Fe_2O_3 (Hematite) Thin-Film Electrodes for Application in High Rate Rechargeable Lithium Batteries. *Small* **2011**, *7* (3), 407–414.

(33) Largeot, C.; Portet, C.; Chmiola, J.; Taberna, P.; Gogotsi, Y.; Simon, P. Relation between the Ion Size and Pore Size for an Electric Double-Layer Capacitor. *J. Am. Chem. Soc.* **2008**, 2730–2731.

(34) Rauda, I. E.; Augustyn, V.; Dunn, B.; Tolbert, S. H. Enhancing Pseudocapacitive Charge Storage in Polymer Templated Mesoporous Materials. *Acc. Chem. Res.* **2013**, *46* (5), 1113–1124.

(35) Cook, J. B.; Kim, H. S.; Lin, T. C.; Robbennolt, S.; Detsi, E.; Dunn, B. S.; Tolbert, S. H.

Tuning Porosity and Surface Area in Mesoporous Silicon for Application in Li-Ion Battery Electrodes. *ACS Appl. Mater. Interfaces* **2017**, *9* (22), 19063–19073.

(36) Fuertes, a. B.; Lota, G.; Centeno, T. a.; Frackowiak, E. Templated Mesoporous Carbons for Supercapacitor Application. *Electrochim. Acta* **2005**, *50* (14), 2799–2805.

(37) Fuertes, A. B.; Pico, F.; Rojo, J. M. Influence of Pore Structure on Electric Double-Layer Capacitance of Template Mesoporous Carbons. *J. Power Sources* **2004**, *133* (2), 329–336.

(38) Shi, Y.; Guo, B.; Corr, S. a; Shi, Q.; Hu, Y.-S.; Heier, K. R.; Chen, L.; Seshadri, R.; Stucky, G. D. Ordered Mesoporous Metallic MoO_2 Materials with Highly Reversible Lithium Storage Capacity. *Nano Lett.* **2009**, *9* (12), 4215–4220.

(39) Brezesinski, T.; Wang, J.; Tolbert, S. H.; Dunn, B. Ordered Mesoporous Alpha-MoO_3 with Iso-Oriented Nanocrystalline Walls for Thin-Film Pseudocapacitors. *Nat. Mater.* **2010**, *9* (2), 146–151.

(40) Kim, J. W.; Augustyn, V.; Dunn, B. The Effect of Crystallinity on the Rapid Pseudocapacitive Response of Nb_2O_5. *Adv. Energy Mater.* **2012**, *2* (1), 141–148.

(41) Tian, G.; Fu, H.; Jing, L.; Tian, C. Synthesis and Photocatalytic Activity of Stable Nanocrystalline TiO_2 with High Crystallinity and Large Surface Area. *J. Hazard. Mater.* **2009**, *161* (2–3), 1122–1130.

(42) Tsung, C. K.; Fan, J.; Zheng, N.; Shi, Q.; Forman, A. J.; Wang, J.; Stucky, G. D. A General Route to Diverse Mesoporous Metal Oxide Submicrospheres with Highly Crystalline Frameworks. *Angew. Chemie - Int. Ed.* **2008**, *47* (45), 8682–8686.

(43) Liu, Y.; Zhang, X. Effect of Calcination Temperature on the Morphology and Electrochemical Properties of Co_3O_4 for Lithium-Ion Battery. *Electrochim. Acta* **2009**, *54* (17), 4180–4185.

(44) Richman, E. K.; Kang, C. B.; Brezesinski, T.; Tolbert, S. H. Ordered Mesoporous Silicon through Magnesium Reduction of Polymer Templated Silica Thin Films. *Nano Lett.* **2008**, *8* (9), 3075–3079.

(45) Brezesinski, T.; Groenewolt, M.; Pinna, N.; Amenitsch, H.; Antonietti, M.; Smarsly, B. Surfactant-Mediated Generation of Iso-Oriented Dense and Mesoporous Crystalline Metal-Oxide Layers. *Adv. Mater.* **2006**, *18* (14), 1827–1831.

(46) Brezesinski, T.; Wang, J.; Polleux, J.; Dunn, B.; Tolbert, S. H. Templated Nanocrystal-Based Porous TiO_2 Films for next-Generation Electrochemical Capacitors. *J. Am. Chem. Soc.* **2009**, *131* (5), 1802–1809.

(47) Buonsanti, R.; Pick, T. E.; Krins, N.; Richardson, T. J.; Helms, B. a; Milliron, D. J. Assembly of Ligand-Stripped Nanocrystals into Precisely Controlled Mesoporous Architectures. *Nano Lett.* **2012**, *12* (7), 3872–3877.

(48) Rauda, I. E.; Buonsanti, R.; Saldarriaga-Lopez, L. C.; Benjauthrit, K.; Schelhas, L. T.; Stefik, M.; Augustyn, V.; Ko, J.; Dunn, B.; Wiesner, U.; Milliron, D. J.; Tolbert, S. H. General Method for the Synthesis of Hierarchical Nanocrystal-Based Mesoporous Materials. *ACS Nano* **2012**, *6* (7), 6386–6399.

(49) Lu, Q.; Chen, J. G.; Xiao, J. Q. Nanostructured Electrodes for High-Performance Pseudocapacitors. *Angew. Chem. Int. Ed. Engl.* **2013**, *52* (7), 1882–1889.

(50) Cox, D. E.; Cava, R. J.; McWhan, D. B.; Murphy, D. W. A Neutron Powder Diffraction Study of the Lithium Insertion Compound $LiMoO_2$ from 4 - 440 K. *J. Phys. Chem. Solids* **1982**, *43* (8), 657–666.

(51) Augustyn, V.; Come, J.; Lowe, M. a; Kim, J. W.; Taberna, P.-L.; Tolbert, S. H.; Abruña, H. D.; Simon, P.; Dunn, B. High-Rate Electrochemical Energy Storage through Li+

Intercalation Pseudocapacitance. *Nat. Mater.* **2013**, *12* (6), 518–522.

CHAPTER 4

Tuning the Porous Structure in PMMA Templated Mesoporous MoO_2 for Pseudocapacitive Li-ion Electrodes

4.1 Introduction

Fast-charging energy storage devices are gaining research interest due to increasing demand for short charging times in applications such as electric vehicles and portable electronics. Traditional Li-ion batteries offer high energy density but are limited by intrinsically slow solid-state ion diffusion rates that lead to long charging times. [1–3] Electrical double layer capacitors (EDLCs), offer higher power density by utilizing non-faradaic ion adsorption at the interface of a high-surface-area electrode (i.e., carbon),[4–6] but the overall capacity in EDLCs is usually low. Since no redox reactions are involved, the amount of charge stored is limited by electrostatic repulsion.[7–9] Pseudocapacitors have the potential to combine the fast charging kinetics of EDLCs with the high energy density of batteries through faradaic reactions that are capacitive in nature.[10–13] Pseudocapacitance occurs by charge transfer at or near the surface of redox active materials where the electron and ion diffusion lengths are short.[11,14,15] The concept of pseudocapacitance also applies to materials that store charge via near surface lithium intercalation, as long as the electrochemical response is not dominated by diffusion limitations.[16–18]

Pseudocapacitive materials can be classified as either intrinsic or extrinsic.[14,19] Intrinsic pseudocapacitive materials,[14] such as $RuO_2 \cdot xH_2O$[20], MnO_2 [21] , and Nb_2O_5,[22,23] display pseudocapacitance for a wide range of particle sizes and morphologies. On the other hand, the electrochemical properties of extrinsic pseudocapacitive materials depend on particle size.[24,25]

Below a certain size, an extrinsic pseudocapacitive material displays capacitor-like behavior, but when above that size, phase transformations and solid-state ion diffusion limitations lead to kinetics typical of bulk battery electrode materials. Extrinsic pseudocapacitance can be achieved by developing nanostructures below the critical grain size of a given electrode material, leading to fast electrochemical kinetics. Specifically, pseudocapacitance arises in an extrinsic material when three key criteria are met:[14,17] (1) good electrical conductivity throughout the electrode, (2) short ion diffusion lengths, and (3) no phase changes upon Li insertion and deinsertion.

The critical size at which extrinsic pseudocapacitive materials start to display pseudocapacitive behavior is material specific. For example, bulk $LiCoO_2$ exhibits a voltage plateau at about 3.9 V vs Li/Li^+ during lithium insertion. This plateau is gradually reduced to a continuously sloping voltage profile as the particle size is reduced. At 6 nm, the voltage profile exhibits an almost linear discharge curve.[26] For TiO_2 nanoparticles, When their particle size is reduced from 30nm to 7nm, the capacitive contribution to the total charge increases from 15% to 55%. This increase is accompanied by a more sloping galvanostatic voltage profile as well as a smaller peak separation in its cyclic voltammogram (CV).[24] Indeed, the sloping voltage response is a good indication of solid-solution intercalation behavior, and thus suppression of standard first-order solid-solid phase transitions, and can thus be used to identify pseudocapacitive behaviors.

Molybdenum dioxide (MoO_2) is a promising extrinsic pseudocapacitive material because of its low metallic resistivity (8.8×10^{-5} Ω cm at 300 K).[27,28] The monoclinic phase possesses a distorted rutile structure that allows Li^+ conduction in octahedral interstitial sites in "tunnels" between Mo chains.[29] The Mo-Mo pairing along the Mo atom chains provides excellent electrical conductivity.[30,31] Because of these facts, monoclinic MoO_2 has traditionally been used as a high energy density conversion-type Li^+ battery electrode,[28,32–35] with a high theoretical capacity of 840

mAh/g. However, due to large volume expansion during the 4-electron reaction and sluggish phase transition from MoO_2 to Mo,[36] MoO_2 cycled as a conversion-type electrode often suffers from poor capacity retention and slow rate capability.[37–39] Sen *et al.*[40] and Kim *et al.*[41] have investigated MoO_2 as an intercalation anode and achieved better cycling stability compared to when cycled as a conversion electrode, but the big grain size (>100 nm) prevented them from realizing capacitor-like kinetic behavior.

In a recent publication,[42] we identified MoO_2 as an extrinsic pseudocapacitor material, with phase change suppression observed in nanoscale form. However, its kinetics was still not ideal compared to other pseudocapacitive materials, with only 50 mAh/g delivered at 20C. The capacitive contribution was only 43% in the 15 nm nanosized-MoO_2. The main reason is that MoO_2 is prone to surface oxidation, and the product, MoO_3, is electrically insulating. Many studies focus on developing carbon based composites or protective coatings to alleviate this problem with good success,[42–51] but these additives lower the specific capacity and complicate synthesis.

In this work, we avoid sluggish electrical conductivity due to the presence of MoO_3 by utilizing mesoporous nanostructures where electroactive MoO_2 grains are interconnected through a three-dimensional network, thus maintaining good electrical conductivity. Moreover, a porous structure allows for good electrolyte accessibility to all electroactive surfaces and limits the solid-state ion diffusion path lengths to the nanoscale pore wall thickness.[52–57] Our goal is to introduce the porous structure into MoO_2 powders and explore the correlation between electrochemical performance and structural variations. MoO_2 with different crystallite size is studied to explore the crossover from battery-like to pseudocapacitive behavior.

In this work, we fabricate mesoporous MoO_2 powders to study their pseudocapacitive properties. These mesoporous MoO_2 powders were synthesized via a freeze-drying process using

poly (methyl methacrylate) (PMMA) colloidal templates. Freeze drying is a well-established route for preparing powders with high surface area and porosity.[58–60] The sublimation of solvent under vacuum occurs with minimal force on the pore walls, therefore preventing the oxide network from collapsing. Compared to typical block copolymer templates, PMMA colloids are cheaper, more scalable, and more versatile, since they can be used in aqueous environments. Structural parameters such as pore volume, pore size, and crystal size were controlled to explore the interrelationships between electrochemical performance and nanoscale architecture. Detailed electrochemical kinetic analyses were used to quantify the amount of capacitive charge storage. The results can be used to understand how nanoscale architecture is related to pseudocapacitive energy storage, and to extrapolate design rules for other extrinsic pseudocapacitors.

4.2 Results and Discussion

4.2.1 Materials characterization

Porous MoO_2 powders studied in the report were prepared by a freeze-drying process using colloidal poly(methyl methacrylate) (PMMA) as a template and ammonium molybdate (MoPOM) as the inorganic precursor (Scheme 4.1). Several different PMMA colloidal sizes (20 nm, 60 nm, 100 nm) and various PMMA-to-MoPOM precursor ratios (m_{PMMA}/m_{Mo}=0.3, 3.2, 5) were used to vary the porosity and pore size. Porous MoO_2 powders were also calcined in Ar at different temperatures (600 ℃, 700 ℃, and 750 ℃) to obtain different crystallinities. Freeze-drying process was employed to achieve and retain homogeneous pore structure during solvent evaporation; when ambient evaporation was used, the PMMA colloids would agglomerate and crash out, creating a non-uniform pore structure with significant pore collapse.

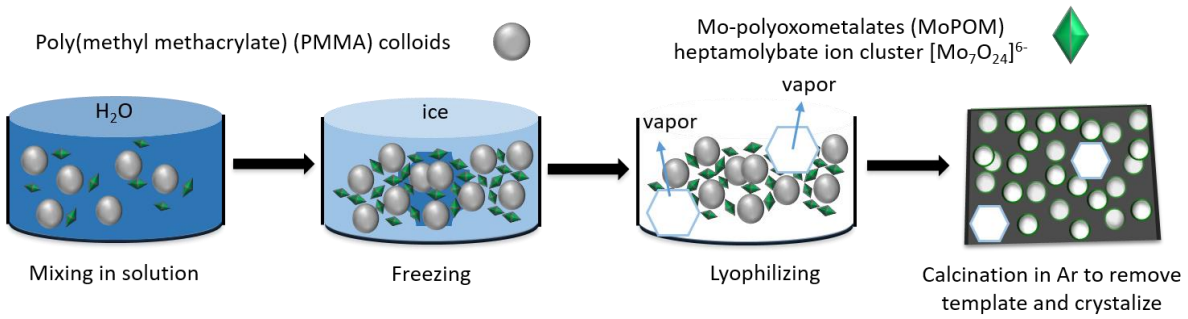

Scheme 4.1. Diagram illustrating the synthesis of colloidal PMMA-templated mesoporous MoO_2 via freeze-drying, followed by calcination to crystallize and remove template.

The morphology and structure of obtained porous MoO_2 powders were characterized using scanning electron microscopy (SEM), N_2 porosimetry, and X-ray diffraction (XRD). Figure 4.1 shows typical SEM images of porous MoO_2 powders prepared with different PMMA sizes and m_{PMMA}/m_{Mo} ratios. Figures 4.1a–4.1c show 700 °C calcined porous MoO_2 powders templated with PMMA of different sizes at ratio m_{PMMA}/m_{Mo} =3.2. It is observed that the pore size increases as the size of the colloids used increases and that the former matches approximately with the latter. The minimal pore collapse and shrinkage in the structure is attributed to the fast sublimation of solvent during the freeze-drying process, which "locks" the structure in place. It is also observed that the wall thickness slightly increases as the pore size increases. Figures 4.1b, 4.1d, and 4.1e show the structure of porous MoO_2 powders templated with 60 nm PMMA at different m_{PMMA}/m_{Mo} ratios. At a higher m_{PMMA}/m_{Mo} ratio, the high pore volume is accompanied by thin walls between pores. In some cases, the wall is too thin to retain the structural integrity under heating and collapsed (Figure 4.1d). At a lower m_{PMMA}/m_{Mo} ratio, the walls between pores are thicker. When m_{PMMA}/m_{Mo} was as low as 0.3, some non-porous particles with sizes of 20-80 nm are observed in SEM, indicating non-homogenous porous structure at that ratio. In the low magnification image (Figure 4.1f), macropores (>100 nm), from departure of solvent during the freeze-drying process are also observed between porous monoliths. Overall, these MoO_2 powders display interconnected

porous networks, which serve as excellent pathways for electrical and ionic conduction and ensure good electrochemical performance in the face of surface oxidation.

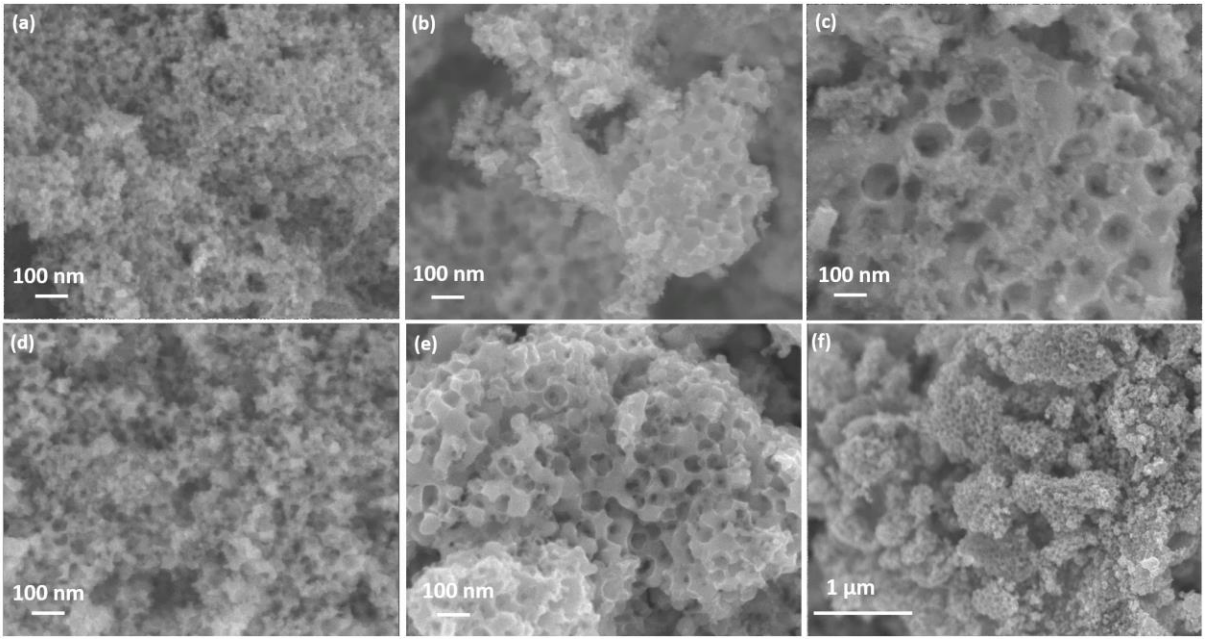

Figure 4.1. SEM images of 700 ℃ calcined porous MoO_2 powder prepared with PMMA colloids of different sizes at m_{PMMA}/m_{Mo} = 3.2 (a) – (c) and with 60 nm PMMA at different ratios (b), (d), (e). (a) 20 nm PMMA, (b) 60 nm PMMA, (c) 100 nm PMMA; (d) m_{PMMA}/m_{Mo} = 5, (e) m_{PMMA}/m_{Mo} = 0.3. The pore size increased with the colloidal size of the PMMA template and the wall thickness increased as a function of the PMMA/MoPOM ratio. (f) Low magnification SEM of porous MoO_2 powder, showing big gaps between porous monoliths.

The porous structure was further characterized by N_2 porosimetry. Figure 4.2a shows a representative nitrogen adsorption/desorption isotherm of porous MoO_2 powder. The isotherm was of type IV with H3 hysteresis loop according to the IUPAC classification,[61,62] indicating that the porous network consisted of macropores that were not completely filled. The average pore diameter was calculated from the desorption isotherm using the Barret−Joyner−Halenda (BJH) analysis (Figure 4.2b). The peak at 60 nm corresponds to the pore size from the PMMA template while the peak at 23 nm corresponds to the neck connecting mesopores. Since all samples contain a large fraction of macropores from the freeze-drying process, the porosity in all samples is

dominated by these big pores, which are beyond the accurately measurable range for N_2 porosimetry. By contrast, the surface area should be dominated by the smaller pores, so we used surface area to learn more about the smaller pores produced by the PMMA templates. Table 4.2 summarizes the structural properties of various samples. When the calcination temperature was increased from 600 to 750 ℃ for a set of samples with fixed PMMA size and mass ratio (60 nm PMMA, m_{PMMA}/m_{Mo} = 3.2), the surface area decreased by 25% while the porosity remained roughly the same. This is because surface area is more sensitive to changes in small pores, while larger pores predominantly affect the porosity. The grain growth accompanying heating at elevated temperatures caused the disappearance of some small pores, but had little effect on large pores. Similarly, the surface area of the 20 nm PMMA templated sample (Sample 7) was more than twice that of the 100 nm PMMA templated sample at the same inorganic to template ratio (Sample 6), due to the favorably small pore size from the 20 nm PMMA template. The porous structure is also very sensitive to changes in the m_{PMMA}/m_{Mo} ratio. The surface area of Sample 5 (m_{PMMA}/m_{Mo} =0.3) is only 32 m^2/g, compared to Sample 4 (m_{PMMA}/m_{Mo} = 5), which has a surface area of 130 m^2/g. Samples 4 and 5 also have a large difference in total pore volume, indicating that the templated pores also contribute to the total porosity. The presence of both mesopores and macropores is important to allow for efficient electrolyte access to all surface active sites.

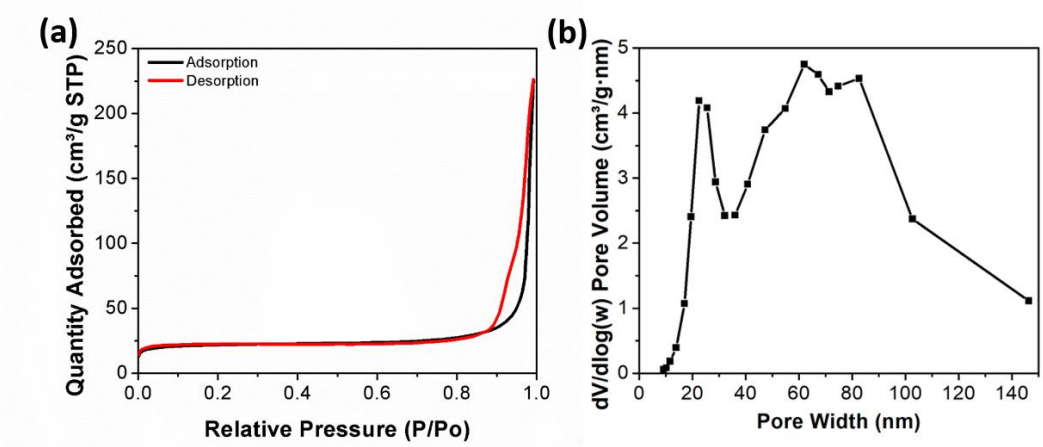

Figure 4.2. Nitrogen porosimetry to quantify the porous structure of mesoporous MoO_2. (a) Nitrogen adsorption/desorption isotherm of 700°C calcined MoO_2 templated with 60 nm PMMA at m_{PMMA}/m_{Mo} = 3.2 and (b) pore size distribution from BJH desorption. Macropores from the solvent evaporation had a large contribution to pore volume and pore size distribution.

Table 4.1. Synthetic conditions and structural characterization of all porous MoO_2 samples

No.	Average PMMA size (nm)	m_{PMMA}/m_{Mo} ratio	Crystallization temperature (°C)	Surface area (m^2/g)¶	Porosity (%) ¶	Pore volume (cm^3/g)¶	Average crystallite size (nm)
1	60	3.2	600	81	66	0.293	11
2	60	3.2	700	66.6	69	0.350	15
3	60	3.2	750	60.2	62	0.250	21
4	60	5	700	130	72	0.397	12
5	60	0.3	700	32	44	0.120	28
6	100	3.2	700	75	55	0.190	26
7	20	3.2	700	158	73	0.424	11

¶ Due to time and instrument constraints, porosimetry measurements for Samples 4-7 were conducted on materials pre-heated at 600 °C in Ar. The actual surface area, porosity and pore volume for 700 °C calcined samples would be slightly different (within 10%), but the relative trend among the samples still holds.

The crystal structure of porous MoO_2 was analyzed using XRD. All samples match JCPDS No. 32-0671 for monoclinic MoO_2 phase, with different peak widths and heights indicating different crystallinities and grain sizes. Crystallinity increases as a function of calcination temperature, as shown by the peak intensity in Figure 4.3a. At the same time, the average crystallite size, calculated from the Scherrer equation, increased from 11 nm to 21 nm. It is also noted that samples prepared under the same temperature but with different PMMA sizes and ratios have very different crystallite sizes. The crystallite size increased with decreasing m_{PMMA}/m_{Mo} ratio as well as increasing PMMA colloidal size, as shown in Figures 4.3b, 4.3c and Table 4.1. As expected, the increase in the crystallite size is correlated with the increase in wall thickness, based on observations from SEM images (Figure 4.1). It has been reported that small size can inhibit crystallization and other phase transition in MoO_2 and other metal oxides,[63,64] so it is reasonable that wall thickness, as determined by the template size and m_{PMMA}/m_{Mo} ratio, has an effect on the crystallization of MoO_2. When the wall thickness is too small in highly porous samples, it may requires a higher calcination temperature to effectively drive crystallization. The complex mixture of crystallinity and porous structure together plays an important role in electrochemical performances, which will be discussed in the following section.

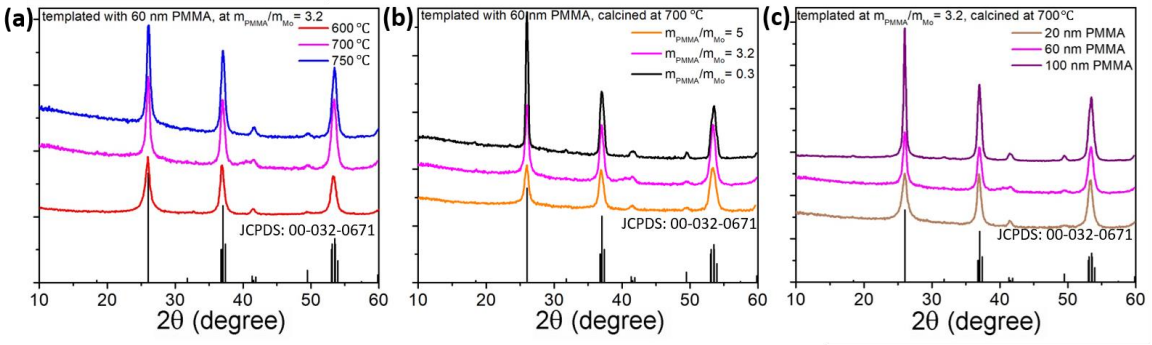

Figure 4.3. X-ray diffraction patterns for PMMA-templated porous MoO_2 under different synthetic conditions: (a) templated with 60nm PMMA at m_{PMMA}/m_{Mo} ratio = 3.2, calcined at different temperatures, (b) templated with 60nm PMMA at different m_{PMMA}/m_{Mo} ratios, calcined at 700 °C , (c) templated with different size PMMA MoO_2 at m_{PMMA}/m_{Mo} ratio = 3.2, calcined at 700 °C. The crystallinity and average crystallite size increased as a function of calcination temperature and PMMA size, and decreased with increasing m_{PMMA}/m_{Mo} ratio.

The surface chemical properties of porous MoO_2 were examined by X-ray photoelectron spectroscopy (XPS). Figure 4.4a shows representative high resolution XPS traces for Mo 3d core level. The Mo 3d peak is composed of 2 sets of the spin-orbit doublet corresponding to Mo $3d_{3/2}$ and Mo $3d_{5/2}$. The peaks at 229.8 eV and 233.0 eV are attributed to Mo^{4+}, those at 232.2 eV and 235.4 eV are attributed to Mo^{5+}, and those at 232.8 eV and 236.1 eV are attributed to Mo^{6+}. Since the probing depth of XPS is usually just a few nm from the surface, this indicates that the surface of our MoO_2 is mostly oxidized. Figure 4.4b shows representative XPS traces for Mo 3d after Ar etching, to remove the surface layer. The Mo^{4+}/Mo_{total} ratio calculated from the peak area changes from 8% to 44%, indicating that the majority of the nanostructure backbone is composed of MoO_2. The interconnected conductive MoO_2 framework should ensure a low overall resistance through the network to enable fast charging pseudocapacitive behavior despite the surface oxidation.

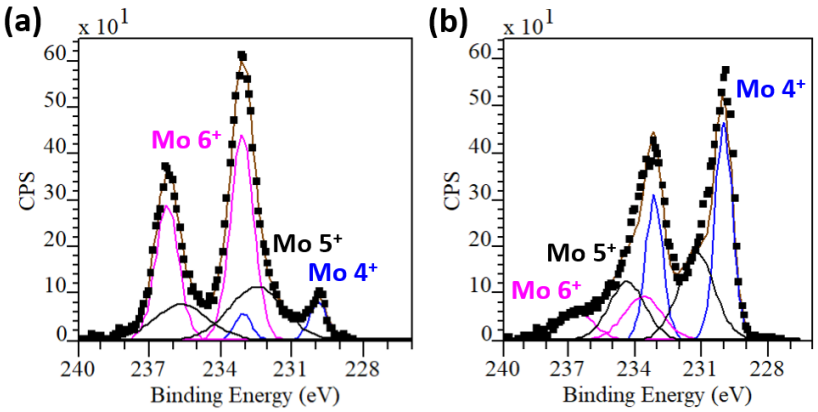

Figure 4.4. X-ray photoelectron spectra obtained to analyze the surface oxidation state of mesoporous MoO_2 (a) pristine and (b) after Ar ion etching. The surface was dominated by Mo^{6+} and beneath the surface layer, Mo^{4+} was the majority.

4.2.2 Electrochemistry

Porous MoO_2 powders were cycled in a typical Swagelok setting between 1.1 and 3 V *vs.* Li/Li^+ to realize the one-electron intercalation process, represented by the following equation:

$$xe^- + xLi + MoO_2 = Li_xMoO_2,\ 0 < x < 0.98,\ C_{theo} = 209.4\ mAh/g. \quad (1)$$

Galvanostatic cycling and cyclic voltammetry (CV) were carried out to investigate the electrochemical properties and their correlation to the structure. C-rate was defined using the theoretical capacity of 209.4 mAh/g.

Figures 4.5a and 4.5b show the galvanostatic charge and discharge traces between 1C and 50C for two representative samples– Samples 4 and 5– prepared with m_{PMMA}/m_{Mo} = 5 and 0.3, respectively, using 60 nm PMMA and calcined at 700 ℃. A clear correlation between crystallite size and the shape of galvanostatic curves is observed. For Sample 4 (m_{PMMA}/m_{Mo} = 5, 12 nm crystallite size), the galvanostatic traces display a voltage slope as a function of the capacity (the amount of Li inserted/extracted). This pseudolinear response is a symbol for pseudocapacitance, as it indicates a solid solution storage mechanism instead of a definite transition between two phases.[17,42] In comparison, the traces in Figure 4.5b for Sample 5 (28 nm crystallite size) display

the traditional stepped plateau features that typically indicate phase transition during charge storage in battery materials.[14,26] Phase change is often a rate-limiting step in battery electrodes because the nucleation and propagation of new phases are usually slow. It is often also accompanied by large structural volume change, which leads to deformation of electrode materials and poor cycle life.[65,66]

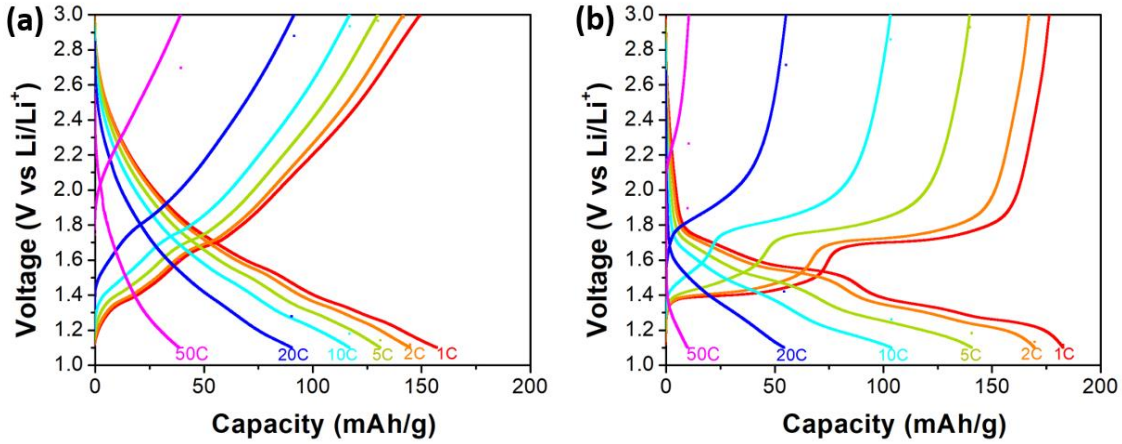

Figure 4.5. Typical galvanostatic charge/discharge curves cycled in the range of 1.1–3 V *vs.* Li/Li^+ for porous MoO_2 (a) templated with 60nm PMMA at m_{PMMA}/m_{Mo} ratio = 5, calcined at 700 ℃, (b) templated with 60nm PMMA at m_{PMMA}/m_{Mo} ratio = 0.3, calcined at 700 ℃. The slope-like voltage response in (a) indicates pseudocapacitive charging behavior with phase transition suppressed, while the stepped plateaus in (b) are typical of battery-like charge storage mechanism.

Using the galvanostatic charge/discharge curves like those shown in Figures 4.5a and 4.5b, we compared the rate performance of MoO_2 samples made at different conditions. Figure 4.6a compares MoO_2 samples templated with 60 nm PMMA at m_{PMMA}/m_{Mo} ratio = 3.2, calcined at different temperatures (Samples 1-3). Sample 2, calcined at 700 ℃, has the highest capacity and best capacity retention at fast rates. More than 100 mAh/g capacity is stored at 20 C (3 minutes). Sample 1, calcined at 600 ℃ has poor rate capability, mostly due to the low crystallinity. Sample 3, calcined at 750 ℃ has good crystallinity and similar surface area and porosity (Table 4.1), but worse capacity retention at fast rates, suggesting that its 21 nm grain size might be beyond the size

range for suppression of phase transitions and thus for pseudocapacitive behavior. Figure 4.6b compares samples templated with 60 nm PMMA at different m_{PMMA}/m_{Mo} ratios and calcined at 700 ℃ (Sample 2, 4 and 5). Sample 4 (m_{PMMA}/m_{Mo} = 5) has a similar rate performance as Sample 2, with 58% capacity retention at 20C. In comparison, Sample 5 (m_{PMMA}/m_{Mo} = 0.3) only has 26% capacity retention at 20C. This corresponds to the drastic differences observed earlier in the galvanostatic charge/discharge curves, with the slope feature in Sample 4 and the plateau feature in Sample 5. This difference in the kinetics results from different mechanisms for charge storage. The pseudocapacitive electrode can undergo fast Li^+ insertion/extract since no phase change occurs upon Li intercalation.

Figure 4.6c compares samples templated with different size PMMA MoO_2 at m_{PMMA}/m_{Mo} ratio = 3.2, calcined at 700 ℃ (Sample 2, 6 and 7 corresponding to colloid sizes of 60 nm, 100 nm, and 20 nm, respectively). Both Sample 6 and 7 show relatively poor cycling results. For Sample 6, the large template size resulted in uneven and thick walls, which may have led to some long solid-state diffusion length of Li^+ intercalation. For Sample 7, the crystallinity is low due to the suppression of nucleation in the extremely thin walls that result from a very small colloid size. Overall, the best rate performance is found in samples made with intermediate sized colloids, which combine adequate crystallinity with a good porous structure.

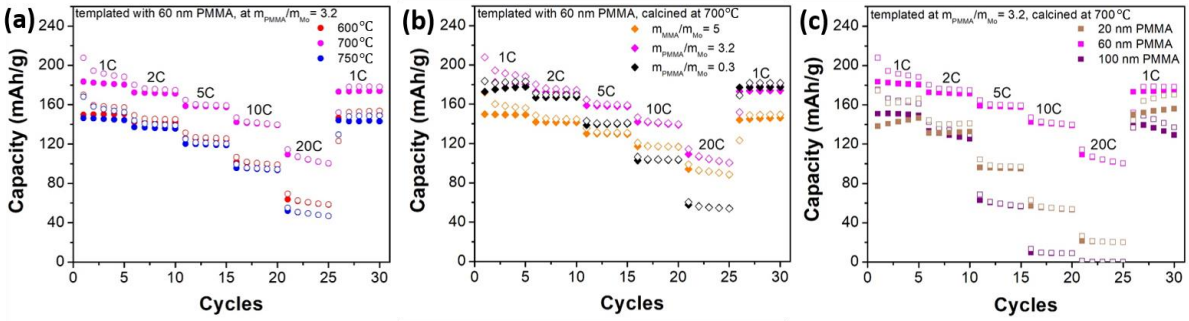

Figure 4.6. Specific capacity as a function of C-rate obtained from galvanostatic charge/discharge curves for MoO_2 made at different condition. (a) templated with 60 nm PMMA at m_{PMMA}/m_{Mo} ratio = 3.2, calcined at different temperatures, (b) templated with 60 nm PMMA at different m_{PMMA}/m_{Mo} ratios, calcined at 700 °C, (c) templated with different size PMMA MoO_2 at m_{PMMA}/m_{Mo} ratio = 3.2, calcined at 700 °C. Overall, MoO_2 templated with 60 nm PMMA at m_{PMMA}/m_{Mo} ratio = 3.2 and 5, calcined at 700 °C, had the best rate capability.

To better quantify these qualitative rate differences, we next turn to kinetic analysis using cyclic voltammograms (CV curves). Figures 4.7a and 4.7b show typical CV curves for porous MoO_2 powders (Samples 4 and 5, respectively) as a function of scan rate. The signature redox peaks at 1.25 V and 1.55 V (Li intercalation) and 1.38 V and 1.7 V *vs.* Li/Li^+ (Li extraction) for MoO_2 are observed. The peaks were less defined in Sample 4 (templated by 60 nm PMMA at m_{PMMA}/m_{Mo} = 5, calcined at 700 °C, 12 nm average crystallite size) than those in Sample 5 (same colloid size and calcination temperature, but with m_{PMMA}/m_{Mo} = 0.3, resulting in a 28 nm average crystallite size). The small size of Sample 4 may make it harder to facilitate two-phase coexistence, giving rise to a broader range of transition voltages instead of one finite voltage. The large peak separation between the oxidation and reduction peak pair in Sample 5 indicates a sluggish electron transfer rate. In contrast, the peak separation between the reduction/oxidation peak pair, as well as their shifts with increasing sweep rates were smaller in Sample 4. These features indicate a smaller polarization in Sample 4 due to the short electron and ion conduction pathway through the thin walls.

To gain greater insights into the reaction kinetics, we analyzed the dependence of peak currents on scan rates at all four MoO_2 redox peaks. Generally, the current (i) obeys a power-law relationship to the scan rate (v) according to the following equation:

$$i = av^b \quad (2)$$

where a and b are constants. The b-value can be determined from the slope of log (i) versus log (v) plots. . A b-value of 0.5 indicates a diffusion-controlled process like those found in traditional batteries and a b-value of 1 represents capacitive behavior.[16,67] Intermediate values correspond to intermediate behavior and can also reflect a distribution of length scales within the sample. The b-values for Samples 4 and 5 were calculated using Equation (2) and labeled next to the corresponding peaks in the CV plots in Figures 4.7a and 4.7b. For Sample 4 (12 nm crystallite size), all b-values were around 0.9, indicating the dominantly capacitive charge storage mechanisms. The fast rate performance of Sample 4 is in good agreement with this capacitive charge storage mechanism. On the other hand, the majority of peaks in Sample 5 (28nm crystallite size) display values between 0.57 and 0.7, suggesting a more diffusion-controlled charge storage mechanism, typical of battery materials. Among the other of samples, Samples 1 and 2 have b-values between 0.8 and 0.9 and Sample 3 has b-values around 0.75-0.8. Overall, the b-values increase with decreasing crystallite size, indicating that the solid-state diffusion lengths (i.e., wall thickness in the porous structure) plays a defining role in terms of charge storage mechanism.

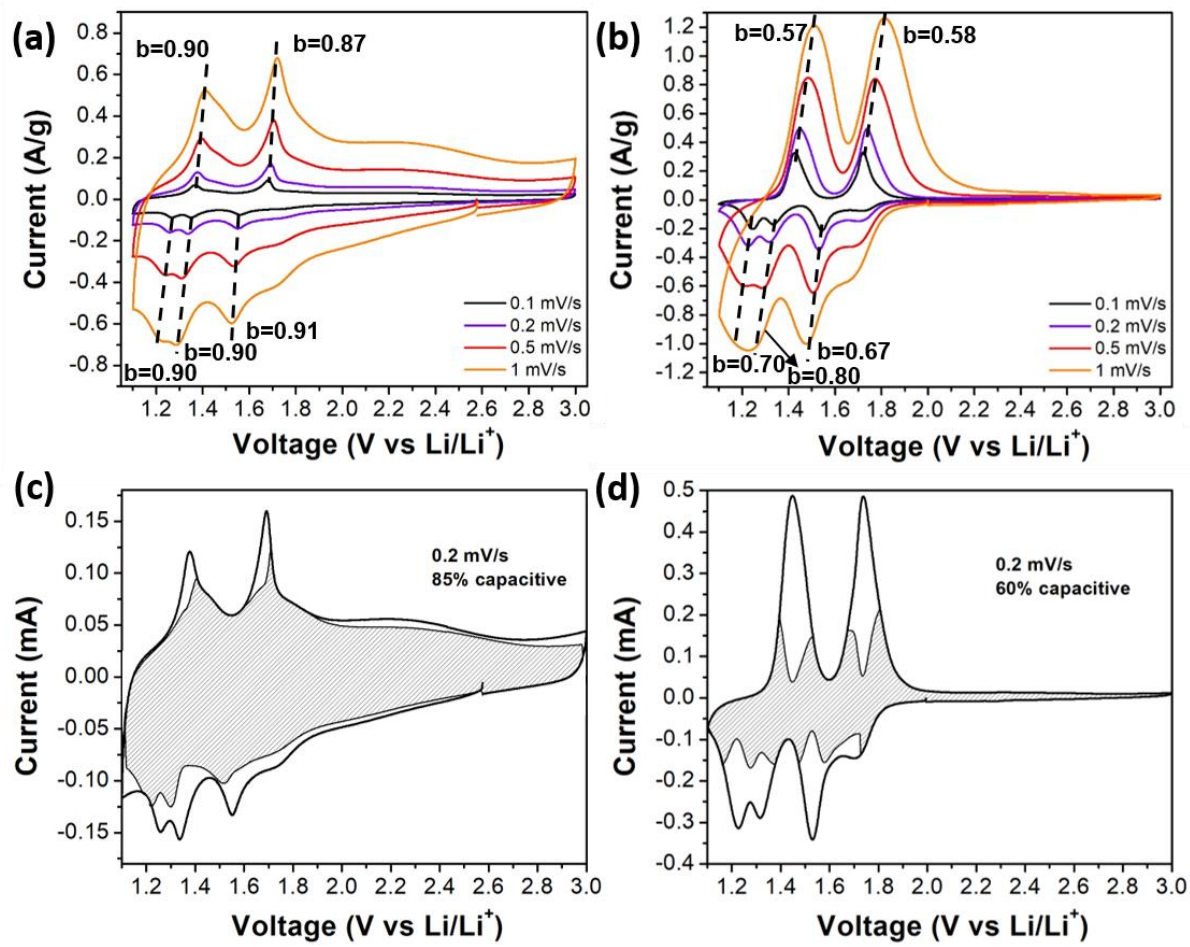

Figure 4.7. Kinetic analysis of pseudocapactive behaviors in porous MoO_2. (a) (b) Cyclic voltammograms with b values calculated from Equation (2) labeled on the redox peaks. (c) (d) Quantification of the capacitive and diffusion-controlled charge storage contributions for MoO_2 cycled at 0.2 mV/s calculated using the method described in Equation (3). (a) (c) are for sample templated with 60nm PMMA at m_{PMMA}/m_{Mo} ratio = 5, calcined at 700 ℃ (12 nm crystallite size) and (b) (d) are for sample prepared at m_{PMMA}/m_{Mo} ratio = 0.3 (28 nm crystallite size). Both analyses suggest the smaller sample stored charge largely through a capacitive mechanism and the larger one was dominated by diffusion.

A related kinetic analysis can be used to quantify the total fraction of the store charge that is capacitive. In this case, instead of allowing any exponent between 0.5 and 1, the current response at each swept voltage $i\ (V)$ is collected at several sweep rates (ν) and then decomposed into a pure diffusion-limited component (which vary as $k_2\nu^{0.5}$) and capacitive current responses (which vary as $k_1\nu$), as shown in Equation (3)

$$i\,(V) = k_1 \nu + k_2 \nu^{0.5}. \quad (3)$$

Here k_1 and k_2 are constants. The 0.2 mV/s CV sweeps for Samples 4 and 5 are shown in Figure 4.7. The shaded regions correspond to the capacitive contribution to the current responses at every voltage. The total integrated capacitive charge storage is about 85% in Sample 4 (12 nm crystallite size) and 60% in Sample 5 (28 nm crystallite size). This result matches well with b-values calculated from Equation (2), indicating dominantly pseudocapacitive behavior in MoO_2 with smaller grains. The regions around the redox peaks are less capacitive for both samples, indicating that either phase changes or longer diffusion distances corresponding to these peak potentials may limits the kinetics. However, Sample 4 has better capacitive character around the peaks, which corroborates the idea of phase change suppression and reduced diffusion distances in the smaller grain size system.

To confirm phase transition is suppressed in the smaller grains, ex-situ XRD measurements were conducted after the electrodes were charged to 1.1 V *vs.* Li/Li^+ followed by a potentiostatic hold. Figure 4.8 shows the ex-situ XRD patterns for Samples 3–5, labeled with their corresponding average crystallite sizes. The peaks in the orange trace (Sample 4, 12 nm crystallite size) correspond well to the reference MoO_2 pattern, indicating little change in structure upon Li intercalation. As the crystallite size increases, a larger peak shift is observed in the diffraction pattern. In the traces for Sample 3 (21 nm crystallite size) and Sample 5 (28 nm crystallite size), the diffraction peaks were shifted by a full degree, indicating the formation of orthorhombic Li_xMoO_2,[42,68] which results from the expected intercalation induced phase transition. These diffraction results also match with our previous study where we observed no phase transition in 15 nm MoO_2 nanocrystals while a full degree shift in microsized particles.[42]

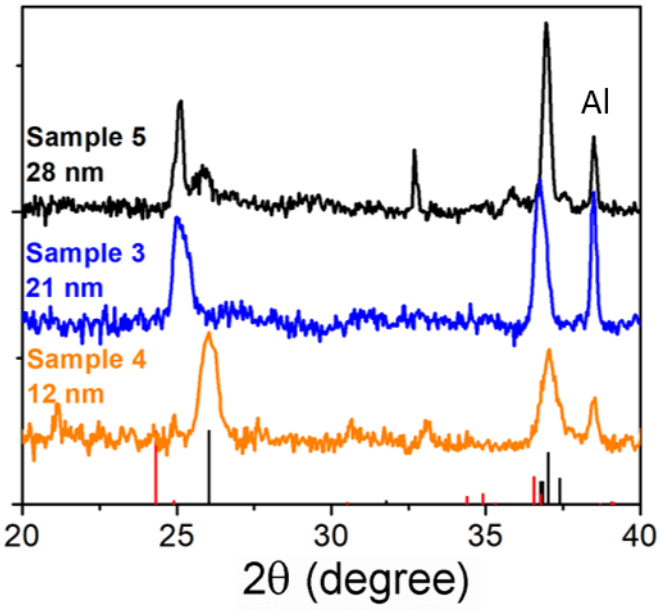

Figure 4.8. Ex-situ XRD patterns of Samples 3-5 after charging to 1.1 V *vs.* Li/Li^+ galvanostatically at C/10. The peak at 38.473 degree is attributed to the Al foil as the current collector. Black stick pattern is for monoclinic MoO_2 (JCPDS 00-032-0671) and red stick pattern is for monoclinic $Li_{0.98}MoO_2$ (JCPDS 01-084-0602). Samples 3 and 5 with 21 and 28 nm average crystallite sizes display phase transition.

Finally, we have investigated the cycling stability of porous MoO_2. Typically, highly capacitive systems have long cycle life, since minimal structural change occurs upon Li^+ insertion/extraction. In addition, the porous network provides flexibility to accommodate any volume change that may take place. As expected, Sample 4 (12 nm crystallite size, m_{PMMA}/m_{Mo} ratio = 5) shows excellent cycle life at 10C (Figure 4.9) with more than 93% capacity retained after 1000 cycles. In contrast, Sample 5 (28 nm crystallite size, m_{PMMA}/m_{Mo} ratio = 0.3) has 75% capacity retention. The extra capacity loss is likely due to structural degradation associated with the phase transition. Both cells are also highly reversible with nearly 100% coulombic efficiency. We attribute this excellent cycling behavior to the pseudocapacitive charging mechanism and the flexible porous network.

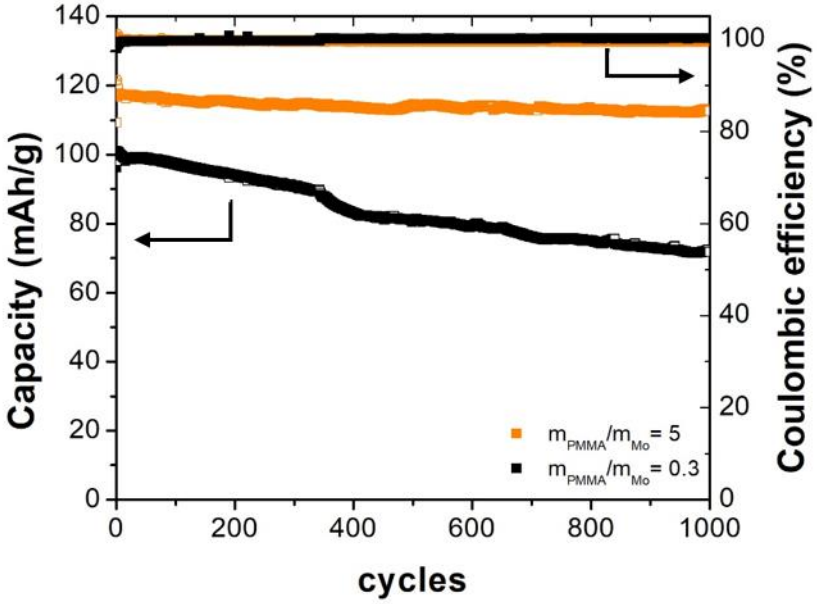

Figure 4.9. Long-term cycling stability of porous MoO_2. Specific capacity versus cycle numbers for sample templated with 60nm PMMA at m_{PMMA}/m_{Mo} ratio = 5 and 0.3, calcined at 700 ℃. The electrode was cycled galvanostatically at 10C for 1000 cycles and showed 93% and 73% of capacity is retained, respectively and coulombic efficiencies approaching 100% for both samples.

4.3 Conclusions

In this work, we have presented the synthesis, structural and electrochemical properties of PMMA-templated MoO_2 powders, which we are using as a new material for pseudocapacitive charge storage. Porous MoO_2 were successfully prepared via a freeze-drying process using PMMA colloids as a template. The structural variations were achieved by varying the template size, PMMA/MoPOM ratio, and crystallization temperature. The charge storage mechanism is affected by the interplay between crystallinity and nanoscale architecture. Samples with the best combination of small crystalline domain size but high crystallinity were shown to have the best performance. In specific, samples with a 12 nm crystallite size, calcined at moderately high termperature were shown to have a capacity of over 100 mAh/g at 20C, with 85% of its charge storage being capacitive, and 93% capacity retention after 1000 cycles. This excellent

electrochemical performance can be attributed to (1) small grain size that results in suppression of the standard lithium intercalation induced phase transition and short solid-state ion diffusion lengths; (2) a combined macroporous and mesoporous network that allows for efficient electrolyte access to Li^+ storage sites and accommodates any volume change; and (3) an interconnected MoO_2 backbone that provides long-range electrical conductivity regardless of any surface oxidation. By analyzing and comparing MoO_2 synthesized under different parameters, we have found that pseudocapacitive contribution increases with decreasing average crystallite size, accompanied by phase transition suppression. Based on our data, the critical size for the onset of pseudocapacitive behavior in MoO_2 appears to be greater than 12 nm and less than 21 nm. As such, these results have furthered our understanding of the relationship between charge storage mechanisms and nanoscale structures. Moreover, these easy to synthesize porous MoO_2 powders show high levels of pseudocapacitive behavior and thus have exciting potential for future applications in fast-charging energy storage devices.

4.4 Experimental methods

Materials: The following materials were obtained from commercial suppliers and used without further purification: ammonium molybdate (para) tetrahydrate $(NH_4)_6Mo_7O_{24}$ $4H_2O$ (MoPOM, 99%, Alfa Aesar), ammonium persulfate (98%, Alfa Aesar), ammonium lauryl sulfate (~30% in H_2O, Sigma Aldrich), methyl methacrylate (contains ≤30 ppm MEHQ as inhibitor, 99%, Sigma Aldrich).

Synthesis of poly(methyl methacrylate) (PMMA): The method is adapted from Wang et al[69,70] and He et al[71]. Ammonium persulfate (APS) was used as the initiator and ammonium lauryl sulfate (ALS) as the surfactant. APS, ALS, and deionized water were put into a three-neck round-bottom flask (250 ml) equipped with a magnetic stirrer, a reflux condenser, and a thermometer. After the

temperature was raised to 75 ˚C, the monomer methyl methacrylate (MMA) was added. For the 20 nm PMMA colloids, the monomer was added in a differential manner (continuous addition in very small drops) using a syringe pump for about 1 hour. Afterwards, the reaction temperature was kept at 80–85 ˚C for an additional hour before a cooling operation was applied. The concentration of reagents was varied to make different sizes of PMMA. The as-obtained PMMA colloidal aqueous solution was used without further purification. Table 4.2 gives the detailed synthesis conditions.

Table 4.2: Synthesis conditions for PMMA colloids of different sizes

Average PMMA colloid size	APS	ALS	MMA	Water
20 nm	0.08 g	2.29 mL	14 mL	84 mL
60 nm	0.08 g	0.61 mL	12.56 mL	165 mL
100 nm	0.08 g	0.03 mL	10 mL	165 mL

Synthesis of MoO_2: In a typical synthesis, ammonium molybdate (MoPOM) was dissolved in PMMA solution. Next, the mixed solution was added dropwise to liquid nitrogen. After the solution was completely frozen, the container was placed in a lyophilizer for at least 24 hours. The powder was then heated under Ar at 600 – 750 °C for 1-2 hours using a 10 °C/min ramp to yield porous MoO_2 with different crystallinities.

Structural characterization: Scanning electron microscopy (SEM) and elemental mapping images were obtained using a JEOL model 6700F electron microscope with an energy dispersive X-ray spectroscopy (EDAX) attachment. X-ray diffraction (XRD) patterns were collected with a PANalytical X'Pert Pro diffractometer operating with Cu Kα (λ = 1.5418 Å) using a 0.05° step size, an accelerating voltage of 45 kV, and a current of 40 mA. X-ray photoelectron spectroscopy (XPS) analysis was performed using a Kratos Axis Ultra DLD with a monochromatic Al K-α

radiation source. The charge neutralizer filament was used to control charging of the sample, a 20 eV pass energy was used with a 0.1 eV step size, and scans were calibrated using the C 1s peak shifted to 284.8 eV. The integrated area of the peaks and atomic ratios were found using CasaXPS software. The atomic sensitivity factors used were from the Kratos library within the Casa software. Nitrogen porosimetry was carried out using a Micromeritics TriStar II 3020 porosimeter. The surface area was then deduced from the adsorption branch of the isotherm at low relative pressures using the Brunauer-Emmett-Teller (BET) model. The pore diameter and pore volume were also derived from the adsorption branch of the isotherm using the Barret-Joyner-Halenda (BJH) model.

Electrochemistry: Slurry electrodes comprised of MoO_2 powder, acetylene carbon black, carbon fiber, and 5% polyacrylic acid (PAA) in EtOH in a weight ratio of 70:10:10:10 were doctor-bladed onto carbon-coated Al foils with 1~2 mg/cm^2 material loading. The electrodes were transferred to a vacuum oven at 80 °C for complete drying. The slurry electrodes were characterized in a two-electrode Swagelok cell with a lithium counter electrode and a glass fiber separator soaked in 1M $LiPF_6$ in 1:1 ethylene carbonate (EC):dimethylene carbonate (DMC) as electrolyte with 5% fluroethylene carbonate (FEC) additive. Cyclic voltammetry (CV) and galvanostatic charge-discharge measurements were carried out on a VMP potentioalstat/galvanostat (Bio-Logic). Cyclic voltammetry was performed between 1.1 V and 3 V *vs.* Li/Li$^+$. All of the electrochemical data were reproduced 3-5 times with a relative error within 4%.

Ex-situ XRD: Measurements were performed on MoO_2 slurry electrodes after electrochemical cycling. The MoO_2 electrodes were cycled galvanostatically at C/10-rate (C-rate is based on a theoretical capacity of 209.4 mAh/g) to 1.1 V *vs.* Li/Li$^+$, followed by a potentiostatic hold to reach equilibrium. The cycled working electrodes were then washed thoroughly with DMC and sealed

in a 64 μm polyimide pouch to prevent exposure to the environment. X-ray diffraction was performed in a Bruker Discover D8 in reflection geometry operating with Cu Kα (λ = 1.5418 Å) using a 0.035◦ step size, a voltage of 40 kV, and a current of 40 mA.

4.5 References

(1) Balke, N.; Jesse, S.; Morozovska, a N.; Eliseev, E.; Chung, D. W.; Kim, Y.; Adamczyk, L.; García, R. E.; Dudney, N.; Kalinin, S. V. Nanoscale Mapping of Ion Diffusion in a Lithium-Ion Battery Cathode. *Nat. Nanotechnol.* **2010**, *5* (10), 749–754.

(2) Winter, M.; Besenhard, J. O.; Spahr, M. E.; Novak, P. Insertion Electrode Materials for Rechargeable Lithium Batteries. *Adv. Mater.* **1998**, *10* (10), 725–763.

(3) Winter, M.; Brodd, R. J. What Are Batteries, Fuel Cells, and Supercapacitors? *Chem. Rev.* **2004**, *104* (10), 4245–4269.

(4) Choi, N.; Chen, Z.; Freunberger, S. A.; Ji, X.; Sun, Y.; Amine, K.; Yushin, G.; Nazar, L. F.; Cho, J.; Bruce, P. G. Challenges Facing Lithium Batteries and Electrical Double-layer Capacitors. *Angew. Chemie Int. Ed.* **2012**, *51* (40), 9994–10024.

(5) Ji, H.; Zhao, X.; Qiao, Z.; Jung, J.; Zhu, Y.; Lu, Y.; Zhang, L. L.; MacDonald, A. H.; Ruoff, R. S. Capacitance of Carbon-Based Electrical Double-Layer Capacitors. *Nat. Commun.* **2014**, *5*, 3317.

(6) Stoller, M. D.; Park, S.; Zhu, Y.; An, J.; Ruoff, R. S. Graphene-Based Ultracapacitors. *Nano Lett.* **2008**, *8* (10), 3498–3502.

(7) Simon, P.; Gogotsi, Y. Materials for Electrochemical Capacitors. *Nat. Mater.* **2008**, *7* (11), 845–854.

(8) Lee, S. W.; Yabuuchi, N.; Gallant, B. M.; Chen, S.; Kim, B.-S.; Hammond, P. T.; Shao-Horn, Y. High-Power Lithium Batteries from Functionalized Carbon-Nanotube Electrodes.

Nat. Nanotechnol. **2010**, *5* (7), 531–537.

(9) Conway, B. E. *Electrochemical Supercapacitors: Scientific Fundamentals and Technological Applications*; Kluwer-Academic, 1999.

(10) Conway, B. E. TECHNICAL PAPERS' ELECTROCHEMICAL SCIENCE AND TECHNOLOGY Transition from "Supercapacitor" to "Battery" Behavior in Electrochemical Energy Storage. *Electrochem. Sci. Technol.* **1991**, *138* (6), 1539–1549.

(11) Conway, B. E. E.; Birss, V.; Wojtowicz, J. The Role and Utilization of Pseudocapacitance for Energy Storage by Supercapacitors. *J. Power Sources* **1997**, *66* (1–2), 1–14.

(12) Conway, B. E.; Pell, W. G. Double-Layer and Pseudocapacitance Types of Electrochemical Capacitors and Their Applications to the Development of Hybrid Devices. *J. Solid State Electrochem.* **2003**, *7* (9), 637–644.

(13) Simon, P.; Gogotsi, Y.; Dunn, B. Materials Science. Where Do Batteries End and Supercapacitors Begin? *Science* **2014**, *343* (6176), 1210–1211.

(14) Augustyn, V.; Simon, P.; Dunn, B. Pseudocapacitive Oxide Materials for High-Rate Electrochemical Energy Storage. *Energy Environ. Sci.* **2014**, *7* (5), 1597.

(15) Boukhalfa, S.; Evanoff, K.; Yushin, G. Atomic Layer Deposition of Vanadium Oxide on Carbon Nanotubes for High-Power Supercapacitor Electrodes. *Energy Environ. Sci.* **2012**, *5* (5), 6872.

(16) Augustyn, V.; Come, J.; Lowe, M. a; Kim, J. W.; Taberna, P.-L.; Tolbert, S. H.; Abruña, H. D.; Simon, P.; Dunn, B. High-Rate Electrochemical Energy Storage through Li+ Intercalation Pseudocapacitance. *Nat. Mater.* **2013**, *12* (6), 518–522.

(17) Cook, J. B.; Kim, H.; Lin, T. C.; Lai, C.; Dunn, B.; Tolbert, S. H. Pseudocapacitive Charge Storage in Thick Composite MoS 2 Nanocrystal-Based Electrodes. **2016**.

(18) Lesel, B. K.; Ko, J. S.; Dunn, B.; Tolbert, S. H. Mesoporous $Li_xMn_2O_4$ Thin Film Cathodes for Lithium-Ion Pseudocapacitors. *ACS Nano* **2016**, *10* (8), 7572–7581.

(19) Come, J.; Augustyn, V.; Kim, J. W.; Rozier, P.; Taberna, P.-L.; Gogotsi, P.; Long, J. W.; Dunn, B.; Simon, P. Electrochemical Kinetics of Nanostructured Nb_2O_5 Electrodes. *J. Electrochem. Soc.* **2014**, *161* (5), A718–A725.

(20) Zheng, J. P.; Cygan, P. J.; Jow, T. R. Hydrous Ruthenium Oxide as an Electrode Material for Electrochemical Capacitors. **1995**, *142* (8), 9–13.

(21) Toupin, M.; Brousse, T.; Be, D. Charge Storage Mechanism of MnO_2 Electrode Used in Aqueous Electrochemical Capacitor. *Chem. Mater.* **2004**, No. 9, 3184–3190.

(22) Augustyn, V.; Kim, W.; Rozier, P.; Taberna, P.; Gogotsi, P.; Long, J. W.; Dunn, B.; Simon, P. Electrochemical Kinetics of Nanostructured Nb_2O_5 Electrodes. *J. Echem. Soc.* **2014**, *161* (5), 718–725.

(23) lim, Eunho; Kim, Haegyeom; Jo, Changshin; Chun, Jinyoung; Ku, Kyojin; Kim, Seongseop; Lee, Hyung; Nam, In-Sik; Yoon, Songhun; Kang, Kisuk; Lee, J. Advanced Hybrid Supercapacitor Based on a Mesoporous Niobium. *ACS Nano* **2014**, *8* (9), 8968–8978.

(24) Wang, J.; Polleux, J.; Lim, J.; Dunn, B. Pseudocapacitive Contributions to Electrochemical Energy Storage in TiO_2 (Anatase) Nanoparticles. *J. Phys. Chem. C* **2007**, *111* (40), 14925–14931.

(25) Lesel, B. K.; Cook, J. B.; Yan, Y.; Lin, T. C.; Tolbert, S. H. Using Nanoscale Domain Size to Control Charge Storage Kinetics in Pseudocapacitive Nanoporous $LiMn_2O_4$ Powders. *ACS Energy Lett.* **2017**, *2* (10), 2293–2298.

(26) Okubo, M.; Hosono, E.; Kim, J.; Enomoto, M.; Kojima, N.; Kudo, T.; Zhou, H.; Honma, I.

Nanosize Effect on High-Rate Li-Ion Intercalation in $LiCoO_2$ Electrode. *J. Am. Chem. Soc.* **2007**, *129* (23), 7444–7452.

(27) Guo, B.; Fang, X.; Li, B.; Shi, Y.; Ouyang, C.; Hu, Y. S.; Wang, Z.; Stucky, G. D.; Chen, L. Synthesis and Lithium Storage Mechanism of Ultrafine MoO_2 Nanorods. *Chem. Mater.* **2012**, *24* (3), 457–463.

(28) Shi, Y.; Guo, B.; Corr, S. a.; Shi, Q.; Hu, Y.-S.; Heier, K. R.; Chen, L.; Seshadri, R.; Stucky, G. D. Ordered Mesoporous Metallic MoO_2 Materials with Highly Reversible Lithium Storage Capacity. *Nano Lett.* **2009**, *9* (12), 4215–4220.

(29) Cox, D. E.; Cava, R. J.; McWhan, D. B.; Murphy, D. W. A Neutron Powder Diffraction Study of the Lithium Insertion Compound $LiMoO_2$ from 4 - 440 K. *J. Phys. Chem. Solids* **1982**, *43* (8), 657–666.

(30) Dahn, J. R.; McKinnon, W. R. Structure and Electrochemistry of Li_xMoO_2. *Solid State Ionics* **1987**, *23* (1–2), 1–7.

(31) Shi, Y.; Guo, B.; Corr, S. a.; Shi, Q.; Hu, Y.-S.; Heier, K. R.; Chen, L.; Seshadri, R.; Stucky, G. D. Ordered Mesoporous Metallic MoO_2 Materials with Highly Reversible Lithium Storage Capacity. *Nano Lett.* **2009**, *9* (12), 4215–4220.

(32) Yang, L.; Liu, L.; Zhu, Y.; Wang, X.; Wu, Y. Preparation of Carbon Coated MoO_2 Nanobelts and Their High Performance as Anode Materials for Lithium Ion Batteries. *J. Mater. Chem.* **2012**, *22* (26), 13148.

(33) Ni, J.; Zhao, Y.; Li, L.; Mai, L. Ultrathin MoO_2 Nanosheets for Superior Lithium Storage. *Nano Energy* **2015**, *11*, 129–135.

(34) Mai, L.; Yang, F.; Zhao, Y.; Xu, X.; Xu, L.; Hu, B.; Luo, Y.; Liu, H. Molybdenum Oxide Nanowires: Synthesis & Properties. *Mater. Today* **2011**, *14* (7–8), 346–353.

(35) Liu, Y.; Zhang, H.; Ouyang, P.; Li, Z. One-Pot Hydrothermal Synthesized MoO_2 with High Reversible Capacity for Anode Application in Lithium Ion Battery. *Electrochim. Acta* **2013**, *102*, 429–435.

(36) Chen, A.; Li, C.; Tang, R.; Yin, L.; Qi, Y. MoO_2-Ordered Mesoporous Carbon Hybrids as Anode Materials with Highly Improved Rate Capability and Reversible Capacity for Lithium-Ion Battery. *Phys. Chem. Chem. Phys.* **2013**, *15* (32), 13601–13610.

(37) Zhou, E.; Wang, C.; Shao, M.; Deng, X.; Xu, X. MoO2nanoparticles Grown on Carbon Fibers as Anode Materials for Lithium-Ion Batteries. *Ceram. Int.* **2017**, *43* (1), 760–765.

(38) Sun, Y.; Hu, X.; Yu, J. C.; Li, Q.; Luo, W.; Yuan, L.; Zhang, W.; Huang, Y. Morphosynthesis of a Hierarchical MoO_2 Nanoarchitecture as a Binder-Free Anode for Lithium-Ion Batteries. *Energy Environ. Sci.* **2011**, *4* (8), 2870.

(39) Wang, Z.; Chen, J. S.; Zhu, T.; Madhavi, S.; Lou, X. W. One-Pot Synthesis of Uniform Carbon-Coated MoO_2 Nanospheres for High-Rate Reversible Lithium Storage. *Chem. Commun. (Camb).* **2010**, *46* (37), 6906–6908.

(40) Kumar Sen, U.; Shaligram, A.; Mitra, S. Intercalation Anode Material for Lithium Ion Battery Based on Molybdenum Dioxide. *ACS Appl. Mater. Interfaces* **2014**, *6* (16), 14311–14319.

(41) Kim, A.; Park, E.; Lee, H.; Kim, H. Highly Reversible Insertion of Lithium into MoO_2 as an Anode Material for Lithium Ion Battery. *J. Alloys Compd.* **2016**, *681*, 301–306.

(42) Kim, H.-S.; Cook, J. B.; Tolbert, S. H.; Dunn, B. The Development of Pseudocapacitive Properties in Nanosized-MoO_2. *J. Electrochem. Soc.* **2015**, *162* (5), A5083–A5090.

(43) Sun, Y.; Hu, X.; Luo, W.; Huang, Y. Ultrafine MoO_2 Nanoparticles Embedded in a Carbon Matrix as a High-Capacity and Long-Life Anode for Lithium-Ion Batteries. *J. Mater. Chem.*

2012, *22* (2), 425–431.

(44) Li, X. yan; Xiao, Q. gui; Gao, Y. ying; Zhang, H. ling; Xu, H. bin; Zhang, Y. Hierarchical MoO_2/C Microspheres: Preparation and Application as Anode Materials for Lithium Ion Batteries. *J. Alloys Compd.* **2017**, *723*, 1113–1120.

(45) Zhao, C.; Yu, C.; Zhang, M.; Huang, H.; Li, S.; Han, X.; Liu, Z.; Yang, J.; Xiao, W.; Liang, J.; et al. Ultrafine MoO_2-Carbon Microstructures Enable Ultralong-Life Power-Type Sodium Ion Storage by Enhanced Pseudocapacitance. *Adv. Energy Mater.* **2017**, *7* (15).

(46) Seng, K. H.; Du, G. D.; Li, L.; Chen, Z. X.; Liu, H. K.; Guo, Z. P. Facile Synthesis of Graphene–molybdenum Dioxide and Its Lithium Storage Properties. *J. Mater. Chem.* **2012**, *22* (31), 16072.

(47) Liu, X.; Ji, W.; Liang, J.; Peng, L.; Hou, W. MoO_2@Carbon Hollow Microspheres with Tunable Interiors and Improved Lithium-Ion Battery Anode Properties. *Phys. Chem. Chem. Phys.* **2014**, *16*, 20570–20577.

(48) Ji, X.; Subramanya Herle, P.; Rho, Y.; Nazar, L. F. Carbon/MoO_2 Composite Based on Porous Semi-Graphitized Nanorod Assemblies from in Situ Reaction of Tri-Block Polymers. *Chem. Mater.* **2007**, *19* (3), 374–383.

(49) Zhou, L.; Wu, H. Bin; Wang, Z.; Lou, X. W. D. Interconnected MoO2 Nanocrystals with Carbon Nanocoating as High-Capacity Anode Materials for Lithium-Ion Batteries. *ACS Appl. Mater. Interfaces* **2011**, *3* (12), 4853–4857.

(50) Park, D.-Y.; Sun, Y.-K.; Myung, S.-T. Carbothermal Synthesis of molybdenum(IV) Oxide as a High Rate Anode for Rechargeable Lithium Batteries. *J. Power Sources* **2015**, *280*, 1–4.

(51) Fu, H.; Xu, Z.; Wang, T.; Li, K.; Shen, X.; Li, J.; Huang, J. Rate Behavior of MoO_2 graphene

Oxide Lithium-Ion Battery Anodes from Electrochemical Contributions. *J. Electrochem. Soc.* **2018**, *165* (3), 0–8.

(52) Brezesinski, K.; Haetge, J.; Wang, J.; Mascotto, S.; Reitz, C.; Rein, A.; Tolbert, S. H.; Perlich, J.; Dunn, B.; Brezesinski, T. Ordered Mesoporous α-Fe_2O_3 (Hematite) Thin-Film Electrodes for Application in High Rate Rechargeable Lithium Batteries. *Small* **2011**, *7* (3), 407–414.

(53) Largeot, C.; Portet, C.; Chmiola, J.; Taberna, P.; Gogotsi, Y.; Simon, P. Relation between the Ion Size and Pore Size for an Electric Double-Layer Capacitor. *J. Am. Chem. Soc.* **2008**, 2730–2731.

(54) Rauda, I. E.; Augustyn, V.; Dunn, B.; Tolbert, S. H. Enhancing Pseudocapacitive Charge Storage in Polymer Templated Mesoporous Materials. *Acc. Chem. Res.* **2013**, *46* (5), 1113–1124.

(55) Cook, J. B.; Kim, H. S.; Lin, T. C.; Robbennolt, S.; Detsi, E.; Dunn, B. S.; Tolbert, S. H. Tuning Porosity and Surface Area in Mesoporous Silicon for Application in Li-Ion Battery Electrodes. *ACS Appl. Mater. Interfaces* **2017**, *9* (22), 19063–19073.

(56) Fuertes, a. B.; Lota, G.; Centeno, T. a.; Frackowiak, E. Templated Mesoporous Carbons for Supercapacitor Application. *Electrochim. Acta* **2005**, *50* (14), 2799–2805.

(57) Fuertes, A. B.; Pico, F.; Rojo, J. M. Influence of Pore Structure on Electric Double-Layer Capacitance of Template Mesoporous Carbons. *J. Power Sources* **2004**, *133* (2), 329–336.

(58) Tamon, H.; Ishizaka, H.; Yamamoto, T.; Suzuki, T. Preparation of Mesoporous Carbon by Freeze Drying. *Carbon N. Y.* **1999**, *37* (12), 2049–2055.

(59) Schlörb, H.; Bungs, M.; Plieth, W. Synthesis and Electrochemical Studies of Manganese Oxides with Spinel Structure in Aqueous Electrolyte (9 M KOH). *Electrochim. Acta* **1997**,

42 (17), 2619–2625.

(60) Sudant, G.; Baudrin, E.; Dunn, B.; Tarascon, J.-M. Synthesis and Electrochemical Properties of Vanadium Oxide Aerogels Prepared by a Freeze-Drying Process. *J. Electrochem. Soc.* **2004**, *151* (5), A666.

(61) R., H. S. J. Gregg, K. S. W. Sing: Adsorption, Surface Area and Porosity. 2. Auflage, Academic Press, London 1982. 303 Seiten, Preis: $ 49.50. *Berichte der Bunsengesellschaft für Phys. Chemie* **2018**, *86* (10), 957.

(62) Thommes, M.; Kaneko, K.; Neimark, A. V.; Olivier, J. P.; Rodriguez-Reinoso, F.; Rouquerol, J.; Sing, K. S. W. Physisorption of Gases, with Special Reference to the Evaluation of Surface Area and Pore Size Distribution (IUPAC Technical Report). *Pure Appl. Chem.* **2015**, *87* (9–10), 1051–1069.

(63) Moroni, D.; Ten Wolde, P. R.; Bolhuis, P. G. Interplay between Structure and Size in a Critical Crystal Nucleus. *Phys. Rev. Lett.* **2005**, *94* (23), 1–4.

(64) Koziej, D.; Rossell, M. D.; Ludi, B.; Hintennach, A.; Novák, P.; Grunwaldt, J. D.; Niederberger, M. Interplay between Size and Crystal Structure of Molybdenum Dioxide Nanoparticlesâ-Synthesis, Growth Mechanism, and Electrochemical Performance. *Small* **2011**, *7* (3), 377–387.

(65) Yao, Y.; McDowell, M. T.; Ryu, I.; Wu, H.; Liu, N.; Hu, L.; Nix, W. D.; Cui, Y. Interconnected Silicon Hollow Nanospheres for Lithium-Ion Battery Anodes with Long Cycle Life. *Nano Lett.* **2011**, *11* (7), 2949–2954.

(66) Wang, X.; Kajiyama, S.; Iinuma, H.; Hosono, E.; Oro, S.; Moriguchi, I.; Okubo, M.; Yamada, A. Pseudocapacitance of MXene Nanosheets for High-Power Sodium-Ion Hybrid Capacitors. *Nat. Commun.* **2015**, *6*, 6544.

(67) Lindström, H.; Södergren, S.; Solbrand, A.; Rensmo, H.; Hjelm, J.; Hagfeldt, A.; Lindquist, S.-E. Li+ Ion Insertion in TiO_2 (Anatase). 2. Voltammetry on Nanoporous Films. *J. Phys. Chem. B* **1997**, *101* (39), 7717–7722.

(68) Cho, W.; Song, J. H.; Kim, J.-H.; Jeong, G.; Lee, E. Y.; Kim, Y.-J. Electrochemical Characteristics of Nano-Sized MoO_2/C Composite Anode Materials for Lithium-Ion Batteries. *J. Appl. Electrochem.* **2012**, *42* (11), 909–915.

(69) Wang, T.; Sel, O.; Djerdj, I.; Smarsly, B. Preparation of a Large Mesoporous CeO2 with Crystalline Walls Using PMMA Colloidal Crystal Templates. *Colloid Polym. Sci.* **2006**, *285* (1), 1–9.

(70) Zou, D.; Ma, S.; Guan, R.; Park, M.; Sun, L.; Aklonis, J. J.; Salovey, R. Model Filled Polymers. V. Synthesis of Crosslinked Monodisperse Polymethacrylate Beads. *J. Polym. Sci. Part A Polym. Chem.* **1992**, *30* (1), 137–144.

(71) He, G.; Pan, Q.; Rempel, G. L. Synthesis of Poly(methyl Methacrylate) Nanosize Particles by Differential Microemulsion Polymerization. *Macromol. Rapid Commun.* **2003**, *24* (9), 585–588.

CHAPTER 5

Increasing the Capacity of Nano-Structured $LiMn_2O_4$ Pseudocapacitors by Selective Crystallization of Dissolution Resistant Surface Facets

5.1 Introduction

In a typical lithium ion battery, charge and discharge times are kinetically limited by long Li-ion solid state diffusion through micron-length-scale powders in the cathode material. Because of the boom in battery operated mobile electronics such as phones and electric vehicles, however, we are experiencing an ever increasing demand for faster recharge times without greatly diminishing energy density. To answer this call, pseudocapacitive electrode materials capable of overcoming the slow solid state limitations of their predecessors have been studied in recent years.[1-5] These materials undergo the same kind of redox processes experienced in typical batteries, but can operate at power densities at least an order of magnitude greater than those currently used in most commercial electrodes thanks to shorter Li-ion diffusion distances.[1-5] Currently, carbon-based double layer supercapacitors are used in most high power applications, but these materials have significantly lower energy densities than lithium ion batteries.[6-9] Pseudocapacitors, by contrast, maintain the same order of magnitude energy density as lithium ion batteries, while still having the capability to deliver high power densities. The fast kinetic abilities observed in pseudocapacitive materials is due to fast solid state diffusion processes, which arise when the diffusion length in the solid state is short compared to the diffusion coefficient of the material.[1-5] Although some materials have innately high diffusion coefficients, pseudocapacitance can be achieved in a broader range of systems by nanostructuring conventional materials such that solid

state diffusion lengths are short. [3,5,10-25] We find that ideal pseudocapacitive nanomaterials are created by making materials with interconnected particles arranged in a porous network, so as to facilitate both electrolyte diffusion through the material and electrical connectivity between the grains. [3,5,10-25] To date, many pseudocapacitive nanomaterials have been identified such as MoO_3, MoS_2, *T*-Nb_2O_5, $LiMn_2O_4$ among others. [3,5,10-25] Of the many materials studied for pseudocapacitive kinetics, $LiMn_2O_4$ has a high enough voltage to be particularly interesting as a cathode in lithium ion pseudocapacitors.[13,18] $LiMn_2O_4$ is indeed an exciting candidate for fast charging cathodes, as nanostructuring it is relatively easy due to its low crystallization temperature. $LiMn_2O_4$ is also attractive as a cathode since it is cheaper and less toxic than other common cathode materials such as $LiCoO_2$, $LiNi_{0.8}Co_{0.15}Al_{0.05}O_2$, $LiNi_xCo_{2-x-y}Mn_yO_2$ and the like.[13-18,24,26] It should be noted that although $LiMn_2O_4$ was originally rejected as a viable commercial cathode material due to poor cyclability in bulk, much more promising behavior is observed in nanostructured material with crystalline sizes below 40 nm.[13-18]

Although fast charge/discharge kinetic and good cycling stability are observed in nanostructured $LiMn_2O_4$, materials with crystallite sizes below 40 nm also show capacity reduction which worsens with decreasing crystallite size and increasing surface area.[13-18] This reduction in capacity compared to bulk is partially due to an inactive surface which contains Mn^{2+} in 8a tetrahedral sites, which is the site where active Li^+ sits in the bulk.[27,28] While these inactive surface sites are the most discussed reason for low capacity in nanostructured $LiMn_2O_4$, additional capacity loss arises from surface dissolution of Mn during the first charge, before the solid electrolyte interphase forms to protect the surface.[13,27-30] In our previous work, we attempted to find the crystallite size that gave the best balance of fast kinetics and reasonable capacities.**Error! Bookmark not defined.** A better option, however, is to address the fundamental capacity loss mechanism,

so that capacity can be improved without increasing crystallite size, thus retaining the ideal kinetics found in smaller domain size materials. Although coating $LiMn_2O_4$ with ALD and other external modifications can be effective in stabilizing the surface and preventing dissolution, these coatings add weight to high surface area nanomaterials, which can reduce the overall capacity of the system.[31-34] As it turns out, however, although all surfaces of $LiMn_2O_4$ are susceptible to Mn^{2+} rearrangement, the (111) surface has been shown to be resistant to dissolution in common Li-ion electrolytes.[29,30,35,36] Therefore, synthesizing nanostructured $LiMn_2O_4$ with selectively more (111) surface sites should result in higher capacity for the resulting material.

Previous reports have in fact managed to fabricate high capacity nanostructured $LiMn_2O_4$ by having dominantly (111) surfaces along the length of nanowires or rods.[37,38] To form these structures, however, first a manganese oxide was formed with the desired nanostructure and then converted into $LiMn_2O_4$ by a solid state conversion using lithium salts.[37,38] This two-step route is used to fabricate nearly all highly nanostructured $LiMn_2O_4$ structures since the manganese oxide precursors are far easier to solution process into impressive nanostructures via inorganic (hard) or polymer (soft) templating than their lithiated counterpart.[13-18,37-41] Hard or soft templating is particularly common in nanostructuring materials for pseudocapacitance as they tend to form good electrolyte pathways and keep interconnectivity between grains for electrical connectivity as mentioned previously. [3,5,10-25,39-41] Although templating is relatively easy to scale, the two-step route is less than ideal compared to a single step method for industrial applications.

One alternative to this two-step process is to use a polymer template directly with lithium and manganese salts in a sol-gel type synthesis to form nanostructured $LiMn_2O_4$ in a single crystallization step without the manganese oxide intermediate. Although sol-gel polymer templating of $LiMn_2O_4$ has been done, it typically requires the use of environmentally harmful

additives such as resorcinol and has no selectivity with regard to surface structure.[42] In other sol-gel systems, however, the anion in salt precursors has been extensively used to obtain preferential surface faceting.[43-45] By combining the concept of selective surface faceting with a one pot sol-gel polymer templating method, a cheap method of producing (111) surface site dominant nanostructured $LiMn_2O_4$ should be possible. This (111) surface dominated structure should show all the benefits of nanostructuring $LiMn_2O_4$ including fast rate kinetics and improved cycle life-time while being more resistant to dissolution and therefore retain more capacity than a structure without the (111) surface selectivity.

Herein we thus report an environmentally benign polymer templated, aqueous sol-gel synthesis where we form nanoporous $LiMn_2O_4$ materials with and without dominant (111) surface faceting for use as cathode materials for lithium ion batteries. The nanostructured $LiMn_2O_4$ powders produced using acetate salt precursors showed no faceting and had a rounded morphology (R-LMO) with no dominant facets. The nanostructured $LiMn_2O_4$ powder produced using nitrate salt precursors formed needle-like morphology (N-LMO) with (111) dominant faceting along the length of the needles. The structural and electrochemical properties of both R-LMO and N-LMO are examined using a combination of high angle X-ray diffraction (XRD), scanning electron microscopy (SEM), N_2 porosimetry, high resolution transmission electronic microscopy (HR-TEM), and a range of electrochemical studies including the use of X-ray photoelectron spectroscopy (XPS) to look at dissolved lithium plated on the counter electrode. The results show that both nanostructured $LiMn_2O_4$ materials have comparable kinetics but that the N-LMO displays higher capacity than the R-LMO.

5.2 Results and Discussion

5.2.1 Structural characterization

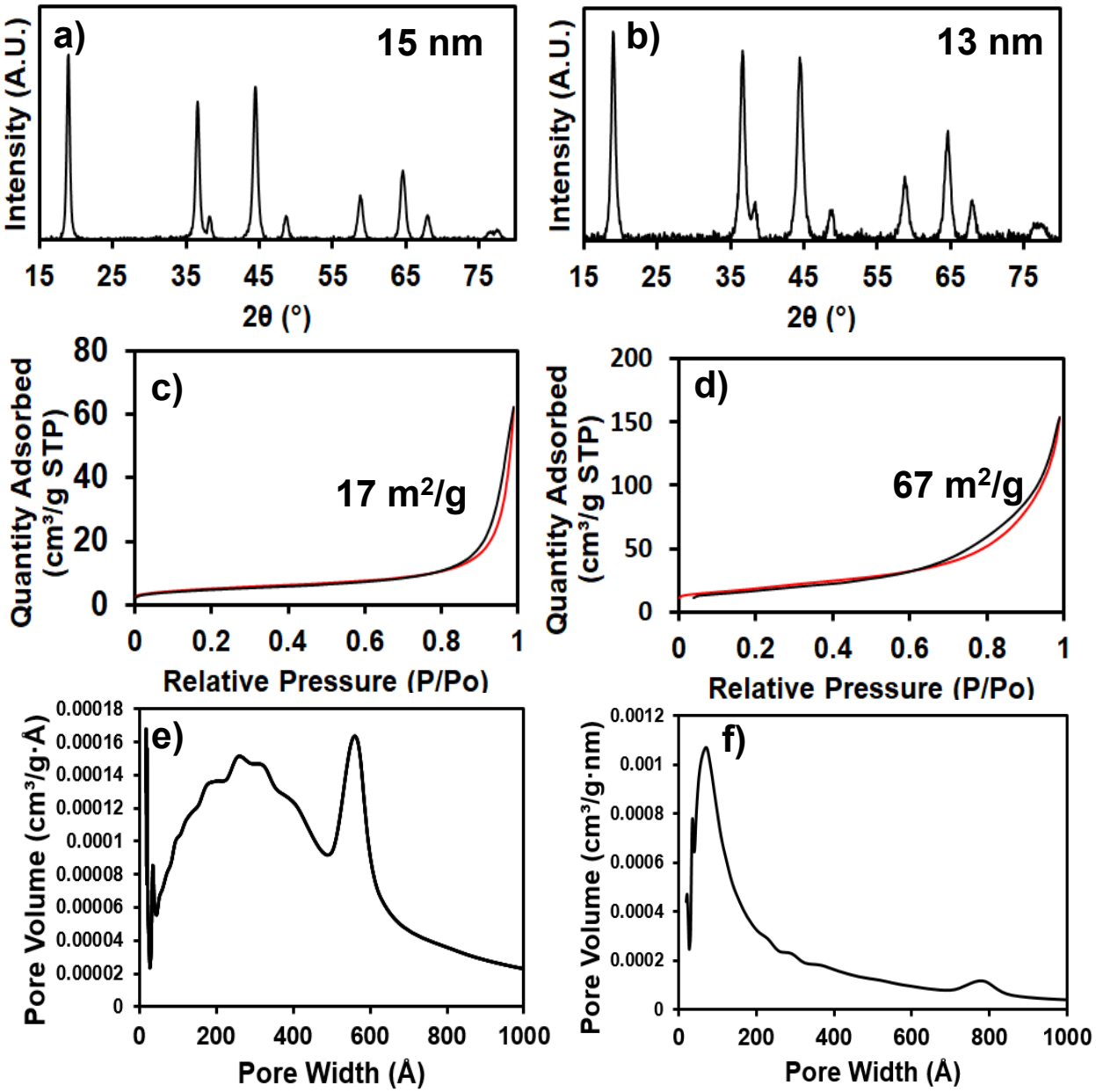

Figure 5.1. XRD of a) R-LMO and b) N-LMO with average Scherrer widths calculated to be 15 nm and 13 nm, respectively; N_2 porosimetry of c) R-LMO and d) N-LMO with surface areas of 17 m^2/g and 67 m^2/g, respectively; Adsorption pore size distribution for e) R-LMO and f) N-LMO, respectively. Note that red lines represent adsorption and black represent desorption.

Fabrication of R- and N-LMO made use of a sol-gel reaction where either acetate or nitrate Li and Mn(II) salts, respectively in a molar ratio 1.1 to 2 were mixed with colloidal poly(methyl methacrylate) spheres of 70 nm average diameter in water and heated at 95 °C for 30 minutes to

evaporate water until the solution became viscous. The resulting solution was poured into a glass petri dish and allowed to sit for several hours to evaporate the remaining water before heating to 550 °C with a ramp of 50 °C/hour and soaking for 1 or 10 hours for R- or N-LMO, respectively. Figure 5.1 shows the resulting XRD patterns, adsorption/desorption isotherms from N_2 porosimetry and resulting BJH pore size distributions for the two nanostructured powders. All peaks in both XRD patterns index to pure $Li_{1.1}Mn_2O_4$ (JCPDS: 00-035-0782) with Fd3m space group. Scherrer widths calculated for both patterns gave similar average crystallite sizes of 15 nm and 13 nm for R- and N-LMO, respectively. N_2 porosimetry shows BET surface areas on the same order of magnitude for both R- and N-LMO of 17 m^2/g and 67 m^2/g, respectively. The disparity in surface area can be understood from the BJH adsorption and desorption pore size distributions. Note that although the vocabulary of porosimetry analysis terms measured values as 'pores' and 'porosity' that it in fact measures all free space within a material, pore or not. Although the space between the nano-needles of N-LMO may not be considered 'pores' they are none the less included in total porosity. Unlike R-LMO which demonstrates a range of pore sizes from 1-100 nm, N-LMO demonstrates a fairly uniform adsorption distribution from 10-50 nm representing the spaces between the needles and a unimodal distribution for pores between the interconnected needle clusters from 50-70 nm. The disparity in surface area and pores size distribution between the two samples originates from the differing nanostructures of the two $LiMn_2O_4$ systems which can be seen from SEM in Figure 5.2(a) and (b). R-LMO seems to show fused, rounded particles with pores formed only between the fused inorganic walls. By contrast, N-LMO exhibits more of a pom-pom like structures made of many needle-like projections which appear to have considerable space between them. This structure results in both the higher surface area and the higher pore volume of the N-LMO. Based on this data alone, we would expect the N-LMO to show lower

capacity than the R-LMO because similar domain sizes are accompanied by increased surface area that could lead to both more inactive surface sites and more Mn dissolution.

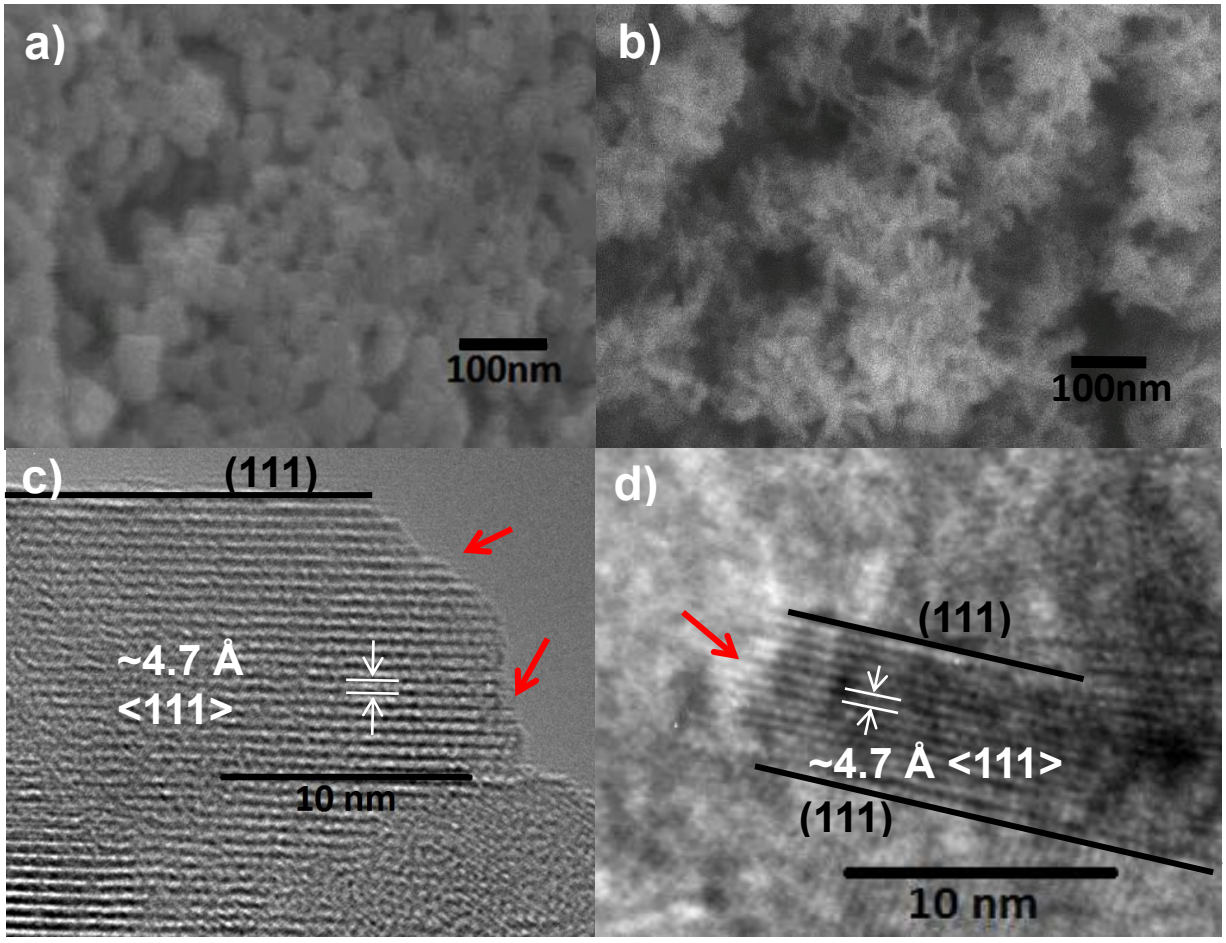

Figure 5.2: SEM of **a)** R-LMO and **b)** N-LMO showing different nanostructure; TEM of **c)** R-LMO and **d)** N-LMO showing lattice spacing of <111> $LiMn_2O_4$ and identifying the parallel (111) surface facets. Red arrows indicate dissolution susceptible surfaces of which R-LMO has more of.

A closer look at the morphology of the nanostructures, seen through HR-TEM (Figure 5.2c and 2d), shows other differences between the two materials. The R-LMO shows a somewhat curved surface with a range of surface facets. The <111> lattice plane, identified by a lattice spacing of ~4.7 Å is observed for both structures. Surfaces parallel to the <111> lattice spacing direction correspond to (111) surfaces, whereas surfaces intersecting the <111> lattice planes (red arrows) are terminated with other faces such as (110) or (001).[29,36] The TEM images show that the

needle-like structures of the N-LMO have the <111> lattice traveling parallel to the long direction, thus the surfaces all along the length of the structures correspond to (111) surfaces, with only the ends displaying non-(111) surfaces. The N-LMO thus display dominant (111) surface character, since the length is significantly longer than the radius (See SI for calculation details). In contrast, the R-LMO does not show any one dominant surface termination due to its relatively round morphology. Note that a true sphere would have less than half of its surfaces parallel to the <111> planes, but because the structure is partly faceted, this value could be a bit higher. We can still safely assume that no more than 50% of the surface is (111) terminated. Overall, we conclude that N-LMO has a higher percentage of (111) surface termini than that of R-LMO.

5.2.2 Electrochemical test

Slurry electrodes were fabricated from the N-LMO and R-LMO powders for electrochemical testing in Swagelok cells. Slurries composed of 75 % active mass, 10 % carbon black, 5 % carbon fibers and 10 % PVDF were prepared with mass loadings between 1 and 2 mg/cm^2. Electrodes were cycled versus lithium metal with $LiPF_6$ in EC:DMC 1:1 electrolyte. The resulting galvanostatic cycling can be seen in Figure 5.3, which includes charge/discharge curves, rate tests and normalized rate data of N- and R-LMO electrodes. From the charge/discharge curves cycled at a relatively slow rate of 1C in Figure 5.3(a), we can see that despite its higher surface area which should lead to reduced capacity, N-LMO achieves about 28 % higher discharge capacity (88 mAh/g) than R-LMO (69 mAh/g). Of course, differing capacity alone does not eliminate the possibility that some kinetic limitation within the R-LMO could be preventing it from achieving the same capacity as N-LMO. If indeed kinetic limitations were a large contributing factor to the capacity disparity between the R- and N-LMO, we would expect to observe poorer overall kinetics in the R-LMO at faster rates. The normalized capacity for both samples at varying C-rates (Figure

5.3c), however, is nearly identical for both R- and N-LMO, which indicates that the capacity difference of R-LMO compared to N-LMO is not related to kinetic differences between the two materials. Additional evidence of similar kinetic behavior was obtained through a kinetic analysis that uses cyclic voltammetry (CV) curves collected at different scan rates to decouple diffusion controlled or battery-like current from capacitive/ pseudocapacitive current (Figure 5.4). We find that the resulting capacitive current contributions for both samples were ~85%, further supporting the claim that kinetics aren't playing a significant role in capacity differences between the R- and N-LMO samples.

As mentioned earlier, there are two primary mechanisms contributing to capacity reduction in nanostructured $LiMn_2O_4$. The first is due to the inactive surface of $LiMn_2O_4$ which originate from the inclusion of reduced Mn^{2+} in the surface 8a tetrahedral sites which normally hold Li^+ in the bulk.[17,27,28] The absence of Li^+ in these surface tetrahedral sites reduces the number of active lithium positions, thereby decreasing the overall capacity substantially in high surface area nano-systems. Because relative surface area is inversely proportional to crystallite size, nanoscale materials with smaller domains should have higher surface area and thus more of these inactive sites. The second mechanism for capacity reduction in nanostructured $LiMn_2O_4$ is dissolution of the surface Mn^{2+} upon direct contact with the electrolyte, followed by reduction of bulk $Mn^{3+/4+}$ to form more Mn^{2+} on the freshly revealed surface.[35,36] This effect is most evident upon charge but because a solid electrolyte interphase (SEI) is formed after the first cycle, direct contact with the electrolyte ceases unless the SEI layer is somehow disturbed. Because finely nanostructured systems of $LiMn_2O_4$ have high surface areas, they are particularly vulnerable to dissolution during the first cycle. Subsequent cycles, however, show impressive reversibility, suggesting that the SEI in these systems are relatively stable.[17-22,39-42] From these results, we can gather that much of the

capacity loss in nanostructured $LiMn_2O_4$ occurs during the first cycle, and therefore having resistance to this initial dissolution could potentially allow for much higher capacity for subsequent cycles.

As discussed previously, (111) terminated surfaces in $LiMn_2O_4$ have been shown to resist dissolution in non-aqueous electrolytes in contrast to non-(111) terminated surface.[29,35,36] Because the round morphology of R-LMO displays far less (111) surfaces than N-LMO, which has (111) terminated surfaces along the length of the needles, we would expect N-LMO to suffer less from surface dissolution and thus display higher capacity than R-LMO. Indeed, the increased dissolution resistance of the N-LMO could explain why we see improved capacity in N-LMO compared to R-LMO with no substantial difference in kinetics.

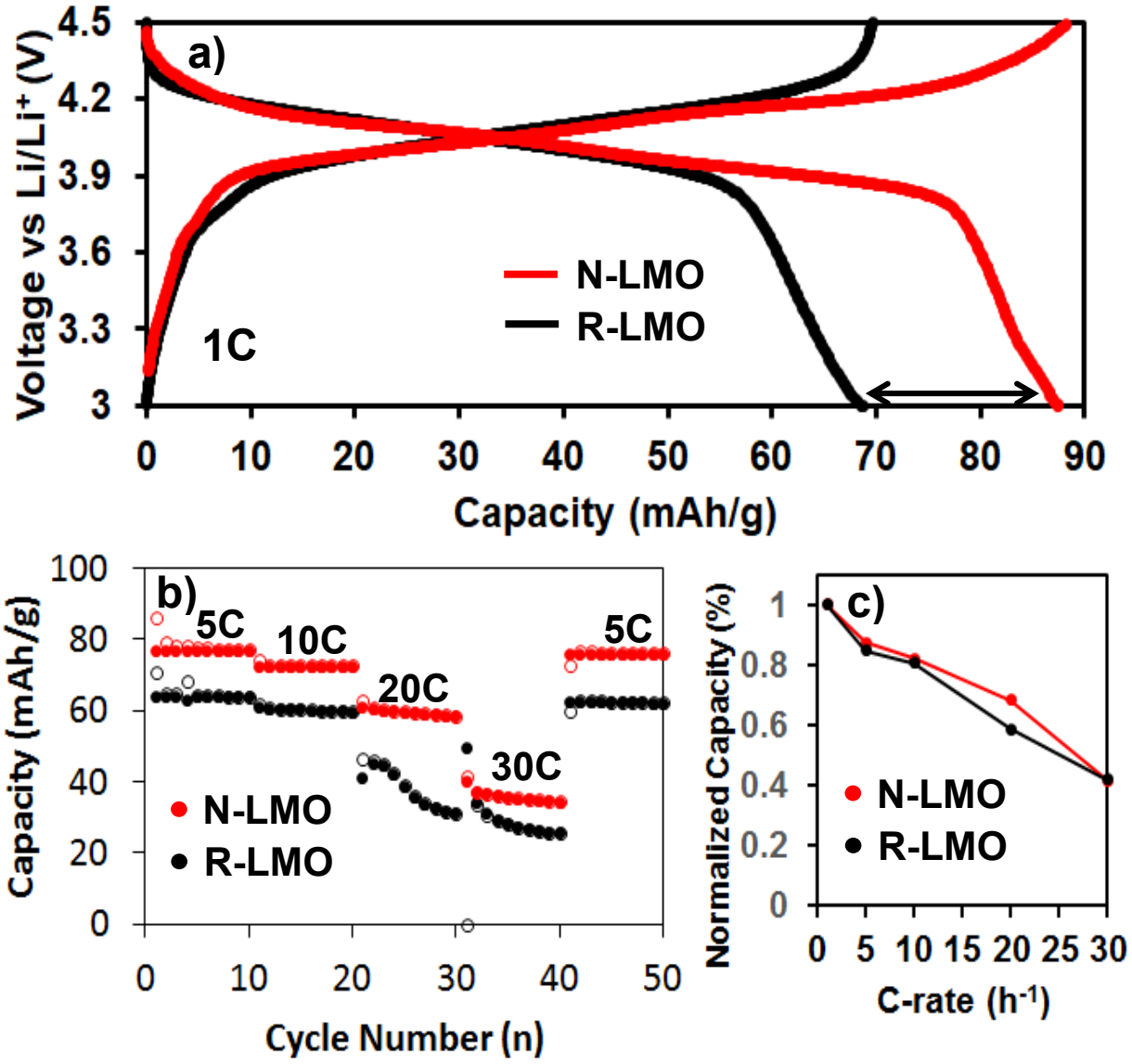

Figure 5.3: Electrochemistry of N- and R-LMO electrodes in Swagelok cells; **a)** Galvanostatic discharge at 1C showing disparity in capacity between N- and R-LMO; **b)** Galvanostatic cycling at 5, 10 and 20C rates; and **c)** Kinetic comparison with normalized capacity.

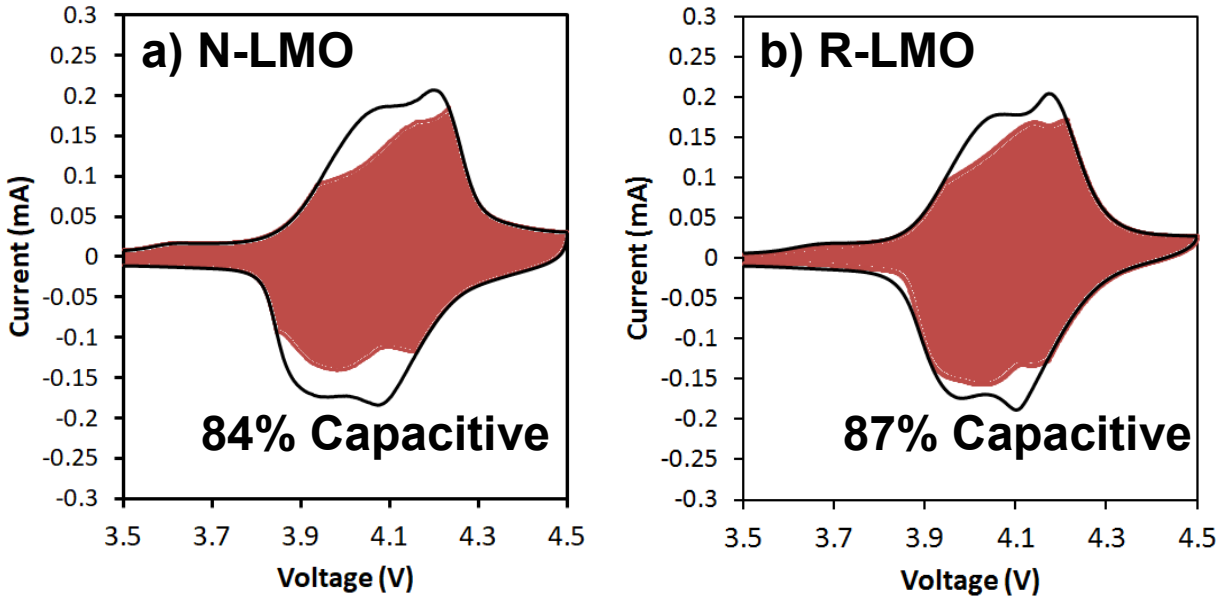

Figure 5.4: The current at any given voltage, *i[V]*, can then be divided into a capacitive component (goes by sweep rate, ν) and a diffusion controlled component (goes by square root of sweep rate, $\nu^{1/2}$) by the equation $i[V] = k_1\nu + k_2\nu^{1/2}$. By taking multiple sweep rates the k_1/k_2 values can be determined for each voltage and capacitive current separated from the diffusion controlled to give a percent capacitive contribution representing the overall kinetic viability of the material. The percentage of the current that is shaded is therefore the percent capacitive character for **a)** N-LMO and **b)** R-LMO based on 1, 0.5 and 0.2 mV/s scan rate cyclic voltammagrams and fixed onto 0.2 mV/s plots. Both systems show similar capacitive contributions, further confirming the kinetic similarity between the two materials. Capacitive character is dominant over diffusion-limited kinetics for both systems, thus confirming pseudocapacitive mechanisms.

5.2.3 Mn dissolution analysis

To support the idea of reduced dissolution in N-LMO compared to R-LMO, we examined cells after cycling for signs of dissolution. One of the most straight forward ways to do this is to look for Mn that dissolved into the electrolyte, and then was plated out on the counter electrode. The lithium metal anode from each cell was thus analyzed using X-ray photoelectron spectroscopy (XPS) for evidence of plated manganese metal. Li metal surface analysis is ideal for identifying relative amount of solvated Mn^{2+} in the electrolyte as the ions are prone to plating onto the Li metal by the spontaneous redox reaction: $2Li^0 + Mn^{2+} \rightarrow 2Li^+ + Mn^0$, $E_{cell}^\circ = -1.86$. To perform this experiment, R- and N-LMO electrodes were cycled in Swagelok cells using Li as counter electrode

at C/10 for one charge-discharge cycle. Cells were then disassembled and the Li foil was used for XPS measurements to identify the relative ratio of Mn to Li (Mn/Li+Mn)). Figure 5.5 shows the resulting Mn 2P and Li 1s XPS peaks from the Li foils from the R- and N-LMO cells. As can be observed from the XPS data, R-LMO displays much higher Mn concentration (and signal) of 1.5% compared to that of N-LMO which shows only 0.3%. The lower Mn/(Li+Mn) % seen at the surface of the Li foil counter electrode of the N-LMO suggest that despite having higher surface area, less Mn was dissolved from N-LMO than from the R-LMO after the first cycle. The lower concentration of Mn in the electrolyte of the N-LMO cell compared to the R-LMO cell after the first cycle supports the theory that N-LMO is more resistant to dissolution than R-LMO. This resistance to Mn dissolution of the N-LMO electrode corroborates the hypothesis that the higher capacity of N-LMO is due to the preservation of active material in the N-LMO sample. Perhaps more importantly, it shows that simple solution processing routes can lead to nanostructured $LiMn_2O_4$ with both a favorable nanoscale structure and favorable surfaces faceting for application in high power density Li-ion energy storage devices.

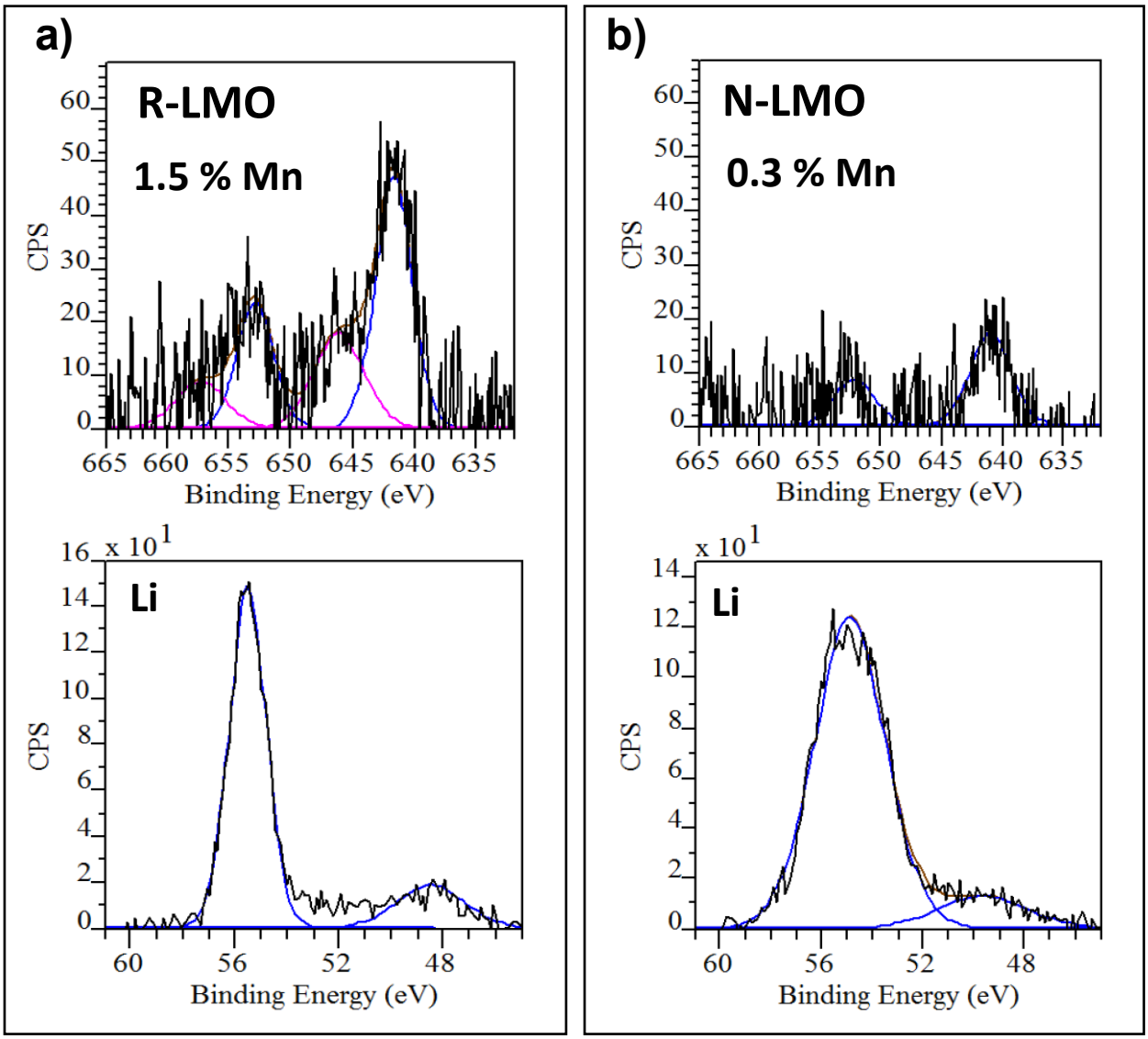

Figure 5.5. Mn 2p and Li 1s XPS of the surface of the lithium metal used as anodes during the cycling of **a)** N-LMO and **b)** R-LMO at C/5 for one cycle. Total Mn deposited onto Li anode used for R-LMO was 1.5% (Mn/(Mn+Li)) and total Mn deposited onto Li anode used for N-LMO was 0.3% (Mn/(Mn+Li)). The fivefold higher concentration of Mn deposited onto the Li from the R-LMO cell compared to the N-LMO suggests dissolution was higher for R-LMO, supporting the theory that N-LMO is comparatively less susceptible to dissolution.

5.3 Conclusion

In summary, two nanostructured $LiMn_2O_4$ powders were produced through a polymer templated sol-gel synthesis using nitrate or acetate salts in order to study their electrochemical attributes. Nanostructured powders synthesized using acetate salts produced materials with a round

grain morphology (R-LMO) which displayed the expected fast cycling kinetic and low capacity typical of small nanostructured $LiMn_2O_4$. Powders synthesized with nitrate salts produced nanostructured networks with a needle-like morphology (N-LMO) with similar cycling kinetics to the R-LMO system, but displayed higher overall capacity. The disparity in capacity between the two samples was understood by identifying that the majority of surfaces in the N-LMO were dissolution resistant (111) surfaces that run along the length of the needles. The dissolution resistance of N-LMO allows for a more intact structure after the first cycle, when Mn^{2+} dissolution often dominates, therefore allowing for higher capacity than in the R-LMO material. The ability to improve capacity without harming cycling kinetics in a well characterized, well understood system marks an exciting advance in our understanding of how to control the electrochemical properties of nanostructured $LiMn_2O_4$ systems using both nanoscale architecture and surface structure. These findings show great promise for producing scalable, cheap nanostructured $LiMn_2O_4$ with few processing steps for use as a fast charging cathode material for lithium ion batteries and pseudocapacitors.

5.4 Experimental Methods

Synthesis of 50 nm poly(methylmethacrylate) (PMMA) template: The PMMA spheres were prepared by emulsion polymerization of methyl methacrylate (Aldrich) monomer (MMA) using ammonium persulfate (APS, Alfa Aesar) as the initiator in deionized water; the method is a modified version of an established method from the literature.[46] First, 165 mL DI water were bubbled with nitrogen for 20 min under stirring to remove any oxygen. Then, 0.3 mL ammonium lauryl sulfate (Aldrich), which serves as a surfactant, and 12.55mL of MMA were added. The APS initiator solution was prepared separately by dissolving 0.075 g APS in 10 mL non-degassed water. The initiator solution was then added to the surfactant and monomer solution at 65 °C under

stirring. The solution was heated to 73 °C and reacted for 3 h. As-prepared colloidal PMMA solution has a concentration of about 50 mg/mL, and were used without further purification. The average size of the PMMA colloids was determined to be 70 nm based on SEM.

Synthesis of round morphology nanostructured $LiMn_2O_4$ (R-LMO): In this method, 2.2 mmol of lithium acetate dihydrate (Sigma) and 4.0 mmol of manganese (II) acetate (Sigma) were mixed with 7.5 mL of the 50 mg/mL aqueous solution of 50 nm PMMA colloids. The solution was then heated and stirred in a round bottom flask for 20 minutes at 90 °C in an oil bath to evaporate part of the water. The resulting viscous solution was poured into a glass petri dish and left to dry for several hours in a fume hood. The resulting solid was heated in a muffle furnace with a ramp of 50 °C/hour from room temperature to 550 °C and soaked for 1 hour. The nano-sized LMO powder was obtained by scrapping the solid from the petri dish surface.

Synthesis of needle-like nanostructured $LiMn_2O_4$ (N-LMO): This synthetic method was almost the same as the acetate salt synthesis described above, except as noted here. In this method, 2.2 mmol of lithium nitrate (Sigma) and 4.0 mmol of manganese (II) nitrate tetrahydrate (Sigma) were used and the resulting solid formed in the petri dish was heated 50 °C/hour from room temperature to 550 °C and soaked for 10 hours.

Slurry electrode and cell fabrication: Typically, 36.5 mg of nanostructured $LiMn_2O_4$ powder was ground in a mortar and pestle with 5.0 mg of carbon black (Super P) and 2.5 mg carbon fiber (Sigma) for 5 minutes. Approximately 100 mg of a 5% polyvinylidene fluoride (PVDF) solution in N-Methyl-2-pyrrolidone (NMP) was added to the homogenized powder along with 10 additional drops of NMP. The resulting slurry was doctor bladed onto a stainless steel substrate with a hight of ~0.3 mm. The slurry was then place under a heat lamp for 1 hour to dry, and then transferred to a vacuum oven heated to ~130 °C while pulling vacuum overnight. The dried slurry electrode sheet

was then punched out using a 0.71 cm^2 puncher and the electrodes transferred to Swagelock cells which were assembled with Li metal in a glove box with 1M $LiPF_6$ in 1:1 EC:DMC as the electrolyte, and a glass fiber separator.

Electrochemical Analysis: Swagelok cells were cycled using a 4-channel Bio-Logic VSP potentiostat controlled using EC-Lab version 10.4 software with $LiMn_2O_4$ as the positive electrode, Li as the negative and Li as the reference. Samples were cycled using both galvanostatic and potentiostatic methods to produce charge/discharge curves and cyclic voltammetry used in the kinetic analysis (from 0.2, 0.5 and 1 mV/s).

Characterization: X-Ray Diffraction (XRD) was taken using both Synchrotron High Angle X-ray Diffraction (XRD) carried out on beamline 11-3 at the Stanford Synchrotron Radiation Laboratory as well as in-house on a Panalytical X'Pert Pro X-ray Powder Diffractometer using a Bragg-Brentano setup. Scherrer widths were calculated and corrected using peak broadening parameters specific to the instrument setup used: Debye-Scherrer and Bragg-Brentano for synchrotron and panalytical instruments respectively. Scanning Electron Microscopy (SEM) images were obtained using a model JEOL JSM-6700F field emission electron microscope with 3 kV accelerating voltage and secondary electron detector configuration. X-ray Photoelectron Spectroscopy (XPS) was taken using a Kratos XPS Axis Ultra DLD spectrometer with a monochromatic Al (Kα) radiation source. Fitting was done using CasaXPS software with Gaussian/Lorentzian 90/10 fit used for all peaks. HRTEM micrographs were collected using an FEI Titan S/TEM operating at 300 kV in transmission mode.

5.5 References

[1] Simon P.; Gogotsi Y.; Dunn B. Where Do Batteries End and Supercapacitors Begin? *Science*, **2014**, 343, 6176, 1210-1211.

[2] Conway, B. E. Transition from ‘supercapacitor’ to ‘battery’ behavior in electrochemical energy storage. *J. Electrochem. Soc.*, **1991**, 138, 1539–1548.

[3] Conway, B. E. Electrochemical Supercapacitors: Scientific Fundamentals and Technological Applications. *Kluwer-Academic*, **1999**.

[4] Angerstein-Kozlowska, H.; Klinger, J.; Conway, B. E. Computer simulations of the kinetic behavior of surface reactions driven by a linear potential sweep. Part I: Model 1-electron reaction with a single adsorbed species. *J. Electroanal. Chem.*, **1977**, 75, 45–60.

[5] Augustyn, V.; Come, J.; Lowe, M.; Kim, J.; Taberna, P.; Tolbert, S.H.; Abruña, H.; Simon, P.; Dunn, B. High-rate electrochemical energy storage through Li+ intercalation pseudocapacitance. *Nat. Mater.,* **2013**, 12, 518-522.

[6] Saliger, R.; Fischer, U.; Herta, C.; Frickle, J. High Sruface Area Carbon Aerogels for Supercapacitors. *J. Non-Cryst. Solids*, **1998**, 225, 81-85.

[7] Pandolfo, A. G.; Hollenkamp, A. F. Carbon Properties and their Roles in Supercapacitors. *J. Power Sources*, **2006**, 1, 19, 11-27.

[8] Zhang, L. L.; Zhao, X. S. Carbon-based Materials as Supercapacitor Electrodes. *RSC*, **2009**, 38, 2520-2531.

[9] El-Kady, M. F.; Strong, V.; Dubin, S.; Kaner, R. B. Laser Scribing of High-Performance and Flexible Graphene-Based Electrochemical Capacitors. *Science*, **2012**, 335, 1326-1330.

[10] Cook, J. B.; Kim, H.-S.; Yan, Y.; Ko, J. S.; Robbennolt, S.; Dunn, B.; Tolbert, S. H. Mesoporous MoS_2 as a Transition Metal Dichalcogenide Exhibiting Pseudocapacitive Li and Na-Ion Charge Storage. *Adv. Energy Mate*r., **2016**, 6, 1501937.

[11] Kim, H.-S.; Cook, J. B.; Tolbert, S. H.; Dunn, B. The Development of Pseudocapacitive Properties in Nanosized-MoO_2. *J. Electrochem. Soc.*, **2015**, 162, 5, A5083-A5090.

[12] Muller, G. A.; Cook, J. B.; Kim H.-S.; Tolbert, S. H.; Dunn B. High Performance Pseudocapacitor Based on 2D Layered Metal Chalcogenide Nanocrystals. *Nano Lett.,* **2015**, 15, 1911−1917.

[13] Brezesinski, T.; Wang, J.; Tolbert, S.H.; Dunn, B. Ordered Mesoporous Alpha-MoO_3 with Iso-Oriented Nanocrystalline Walls for Thin-Film Pseudocapacitors. *Nat. Mater.,* **2010**, *9*, 146-151.

[14] Brezesinski, T.; Wang, J.; Polleux, J.; Dunn, B.; Tolbert, S.H. Templated Nanocrystal-Based Porous TiO_2 Films for Next-Generation Electrochemical Capacitors. *J. Am. Chem. Soc.,* **2009**, *131*, 1802-1809.

[15] Brezesinski, K.; Wang, J.; Haetge, J.; Reitz, C.; Steinmueller, S. O.; Tolbert, S. H.; Smarsly, B. M.; Dunn, B.; Brezesinski, T. Pseudocapacitive Contributions to Charge Storage in Highly Ordered Mesoporous Group v Transition Metal Oxides with Iso-Oriented Layered Nanocrystalline Domains. *J. Am. Chem. Soc.*, **2010**, 132, 20, 6982–6990.

[16] Rauda, I. E.; Augustyn, V.; Saldarriaga-Lopez, L. C.; Chen, X.; Schelhas, L. T.; Rubloff, G. W.; Dunn, B.; Tolbert, S. H. Nanostructured Pseudocapacitors Based on Atomic Layer Deposition of V_2O_5 onto Conductive Nanocrystal-based Mesoporous ITO Scaffolds. *Adv. Funct. Mater.*, **2014**, 24, 6717-6728.

[17] Lesel, B. K.; Ko, J.; Dunn, B.; Tolbert, S. H. Mesoporous $Li_xMn_2O_4$ Thin Film Cathodes for Lithium-Ion Pseudocapacitors. *ACS Nano*, **2016,** DOI: 10.1021/acsnano.6b02608.

[18] Luo, J.; Wang, Y.; Xiong, H.; Xia, Y. Ordered Mesoporous Spinel $LiMn_2O_4$ by a Soft-Chemical Process as a Cathode Material for Lithium-Ion Batteries. *Chem. Mater.,* **2007**, 19, 4791-4795.

[19] Hwang, B.; Kim, S.; Lee, Y.; Han, B.; Kim, S.; Kim, W.; Park, K. Mesoporous Spinel LiMn2O4 Nanomaterial as a Cathode for High-Performance Lithium Ion Batteries. *Int. J. Electrochem. Sci.*, **2013**, 8, 9449 – 9458.

[20] Jayaraman, S.; Aravindan, V.; Kumar, P. S.; Ling, W. C.; Ramakrishna S.; Madhavi, S. Synthesis of porous LiMn2O4 hollow nanofibers by electrospinning with extraordinary lithium storage properties. *Chem. Commun.,* **2013**, 49, 6677.

[21] Jiao, F.; Bao, J.; Hill, A. H.; Bruce, P. G. Synthesis of Ordered Mesoporous Li–Mn–O Spinel as a Positive Electrode for Rechargeable Lithium Batteries. *Angew. Chem. Int. Ed.,* **2008**, 47, 9711 –9716.

[22] Lesel, B. K.; Cook, J. B.; Yan, Y.; Lin, T.; Tolbert, S. H. Kinetic Analysis of the Pseudocapacitive Characteristics of $LiMn_2O_4$ Nanoporous Powders of Various Crystallite Sizes. Submitted, *ACS Energy Letters*. DOI: 10.1021/acsenergylett.7b00634

[23] Zhu, Y.; Peng, L.; Chen, D.; Yu, G. Intercalation Pseudocapacitance in Ultrathin VOPO4 Nanosheets: Toward High-Rate Alkali-Ion-Based Electrochemical Energy Storage. *NanoLett.,* **2016**, 16, 742−747.

[24] Okubo, M.; Hosono, E.; Kim, J.; Enomoto, M.; Kojima, N.; Kudo T.; Zhou, H.; Honma, I. Nanosize Effect on High-Rate Li-ion Intercalation in $LiCoO_2$ Electrode. *J. Am. Chem. Soc.,* **2007**, 129, 7444-7452.

[25] Kim, M.; Lee, S.; Kang, B. Fast-Rate Capable Electrode Material with Higher Energy Density than $LiFePO_4$: 4.2V $LiVPO_4F$ Synthesized by Scalable Single-Step Solid-State Reaction. *Advanced Science*, **2016**, 3, 3, 1500366. doi:10.1002/advs.201500366.

[26] Islam, M. S.; Fisher, C. A. J. Lithium and sodium battery cathode material: computational insights into voltage, diffusion and nanostructural properties. *Chem. Soc. Rev.,* **2014**, 43, 185-204.

[27] Amos, C. D.; Roldan, M. A.; Varela, M.; Goodenough, J. B.; Ferreira, P. J. Revealing the Reconstructed Surface of $LiMn_2O_4$. *Nano Lett*., **2016**, 16, 2899−2906.

[28] Tang, D.; Sun, Y.; Yang, Z.; Ben, L.; Gu, L.; Huang, X. Surface Structure Evolution of LiMn2O4 Cathode Material upon Charge/Discharge. *Chem. Mater.,* **2014**, 26, 3535−3543.

[29] Kim, S.; Aykol, M.; Wolverton C. Surface phase diagram and stability of (001) and (111) $LiMn_2O_4$ spinel oxides. *Phys. Rev. B*, 92, **2015**, 115411.

[30] Weiwei Sun, Feng Cao, Yumin Liu, Xingzhong Zhao, Xiaogang Liu and Jikang Yuan Nanoporous $LiMn_2O_4$ nanosheets with exposed {111} facets as cathodes for highly reversible lithium-ion batteries. J. Mater. Chem., 2012, 22, 20952

[31] Lu, J.; Zhan, C.; Wu, T.; Wen, J.; Lei, Y.; Kropf, A. J.; Wu, H.; Miller, D. J.; Elam, J. W.; Sun, Y.-K.; Qiu, X.; Amine, K. Effectively Suppressing Dissolution of Manganese from Spinel Lithium Manganate via a Nanoscale Surface-Doping Approach. *Nat. Commun.*, **2014**, 5, 5693.

[32] Zhao, J.; Wang, Y. Surface Modifications of Li-Ion Battery Electrodes with Various Ultrathin Amphoteric Oxide Coatings for Enhanced Cycleability. *J. Solid State Electrochem*., **2013**, 17 (4), 1049− 1058.

[33] Ouyang, C. Y.; Zeng, X. M.; Šljivancanin, Z.; Baldereschi, A. Oxidation States of Mn Atoms at Clean and Al2O3-Covered LiMn2O4(001) Surfaces. *J. Phys. Chem. C*, **2010**, 114 (10), 4756−4759

[34] Zhang, C.; Liu, X.; Su, Q.; Wu, J.; Huang, T.; Yu, A. Enhancing Electrochemical Performance of $LiMn_2O_4$ Cathode Material at Elevated Temperature by Uniform Nanosized TiO_2 Coating. *ACS Sustain. Chem. Eng.*, **2017**, *5* (1), 640–647.

[35] Kitta, M.; Kohyama M. Stability of the LiMn2O4 surface in a LiPF6-based non-aqueous electrolyte studied by in-situ atomic force microscopy. *Jpn. J. Appl. Phys.* **2016**, 55, 065801.

[36] Hirayama, M.; Ido, H.; Kim, K. S.; Cho, W.; Tamura, K.; Mizuki, J.; Kanno, R. Dynamic Structural Changes at $LiMn_2O_4$/Electrolyte Interface during Lithium Battery Reaction. *J. Am. Chem. Soc.*, **2010**, 132, 15268–15276.

[37] Lee H.; Muralidharan, P.; Ruffo, R.; Mari, C. M.; Cui, Y.; Kim, D. K. Ultrathin Spinel $LiMn_2O_4$ Nanowires as High Power Cathode Materials for Li-Ion Batteries. *Nano Lett.*, **2010**, 10, 3852–3856.

[38] Cheng, F.; Wang, H.; Zhu, Z.; Wang, Y.; Zhang, T.; Tao, Z.; Chen, J. Porous $LiMn_2O_4$ nanorods with durable high -rate capability for rechargeable Li-ion batteries. *Energy Envirn. Sci.*, **2011**, 4, 3668-3675.

[39] Jiao, F.; Bao, J.; Hill, A. H.; Bruce, P. G. Synthesis of Ordered Mesoporous Li–Mn–O Spinel as a Positive Electrode for Rechargeable Lithium Batteries. Angew. *Chem. Int. Ed.*, **2008**, 47, 9711–9716.

[40] Luo, J.; Wang, Y.; Xiong, H.; Xia, Y. Ordered Mesoporous Spinel $LiMn_2O_4$ by a Soft-Chemical Process as a Cathode Material for Lithium-Ion Batteries. *Chem. Mater.*, **2007**, 19, 4791-4795.

[41] Hwang, B.; Kim, S.; Lee, Y.; Han, B.; Kim, S.; Kim, W.; Park, K. Mesoporous Spinel $LiMn_2O_4$ Nanomaterial as a Cathode for High-Performance Lithium Ion Batteries. *Int. J. Electrochem. Sci.*, **2013**, 8, 9449 – 9458.

[42] Shaju K. M.; Bruce, P. G. A Stoichiometric Nano-$LiMn_2O_4$ Spinel Electrode Exhibiting High Power and Stable Cycling. *Chem. Mater.*, **2008**, 20, 5557–5562.

[43] Znaidi, L., Chauveau, T., Tallaire, A., Liu, F., Rahmani, M., Bockelee, V., & Doppelt, P. Textured ZnO thin films by sol–gel process: Synthesis and characterizations. *Thin Solid Films*, **2016**, *617*, 156-160.

[44] Ravichandran, K., Rajkumar, P. V., Sakthivel, B., Swaminathan, K., & Chinnappa, L. Role of precursor material and annealing ambience on the physical properties of SILAR deposited ZnO films. *Ceramics International*, **2014**, *40*(8), 12375-12382.

[45] Bacaksiz, E.; Parlak, M.; Tomakin, M.; Özçelik, A.; Karakiz, M.; Altunbaş, M. The Effects of Zinc Nitrate, Zinc Acetate and Zinc Chloride Precursors on Investigation of Structural and Optical Properties of ZnO Thin Films. *J. Alloys Compd.*, **2008**, *466* (1–2), 447–450.

[46] Wang, T.; Sel, O.; Djerdj, I.; Smarsly, B. Preparation of a Large Mesoporous CeO_2 with Crystalline Walls Using PMMA Colloidal Crystal Templates. *Colloid Polym. Sci.*, **2006**, *285* (1), 1–9.

CHAPTER 6

Exploring the Effect of Porous Structure on Thermal Conductivity of Mesoporous SiO_2 Films

6.1 Introduction

Over the last few decades, mesoporous silica has been widely studied due to its simple synthesis and easy control of the structural properties. It is often used in a wide range of applications including thermally insulating materials, low-k electrics, [1,2] MEMS,[3,4] and window insulation.[5] Mesoporous SiO_2 is typically prepared by either (1) template-free[6–10] or (2) template-assisted synthesis.[11–14] In the template-free synthesis, random porosity is created by controlled gelation of dissolved molecular precursors and subsequent removal of the solvent. For instance, silica aerogels, prepared by supercritical drying of silica sol-gel without template, can reach porosities of 99%[15] and thermal conductivity of 0.013 W/mK at room temperature and atmospheric pressure.[16] Similarly, silica ambigels can be synthesized by drying template-free SiO_2 precursors at ambient temperature and pressure. For example, Chang *et al.*[17] synthesized hydrophobic mesoporous SiO_2 by ambient drying featuring porosity of 97% and thermal conductivity of 0.034 W/m.K. However, due to high porosity and wide pore size distribution, silica aerogels and ambigels often do not have sufficient mechanical strength and/or optical transparency for a number of potential thermal barrier applications.[18] On the other hand, in the template-assisted synthesis, the pores are formed by controlled gelation of molecular precursors around a template that is subsequently removed by physical or chemical treatment. Common templates include inorganic hard templates[19,20], organic surfactants[21,22] and block copolymers.[23–26] Several studies[27,28] report a

thermal conductivity of 0.3-0.35 W/m.K at a porosity of ~30% in templated porous SiO_2. In this approach, the pore volume and the pore size are easily controlled by choosing the amount and type of template.

Mesoporous SiO_2 has significantly lower thermal conductivity than bulk SiO_2 for several reasons.[28,29] First, the reduced volume of solid phase reduces the heat conduction pathways. Second, the structural factors such as pore size and its distribution can also contribute to reduction in thermal conductivity of mesoporous silica, since the mean free path of heat carriers can be suppressed due to the boundary scattering near nanosized pores[30–33] Finally, the interfacial resistance between nanodomains can also further decrease the effective thermal conductivity. Notably, the effects of nanostructural factors on the thermal conductivity of mesoporous silica have not been well-documented to date.

Coquil *et al.*[27] reported the cross-plane thermal conductivity of highly ordered cubic and hexagonal mesoporous amorphous silica thin films synthesized by evaporation-induced self-assembly. They found the average thermal conductivity was 0.3 W/mK for the cubic SiO_2 films with 25% porosity and 0.2 W/mK for hexagonal SiO_2 films with 44% porosity. They concluded that the thermal conductivity decreases with increasing porosity and is independent of film thickness, pore diameter and wall thickness. However, the explored mesoporous silica films were all prepared using a sol-gel synthesis and porosity fell in the relatively narrow range of 20–50%. Hopkins *et al.*[28] confirmed the low thermal conductivity of evaporation-induced self-assembly SiO_2 films around 0.3 W/mK with porosity around 25% percent, using time-domain thermoreflectance technique. Fang *et al.*[34,35] compared thermal conductivity of mesoporous crystalline TiO_2 films prepared by a sol-gel synthesis and mesoporous TiO_2 films made of TiO_2 nanocrystals. They showed that the thermal conductivity of nanocrystal-based TiO_2 films was 40%

lower than that of mesoporous TiO_2 films prepared by a sol-gel synthesis. They attributed these results to the facts that (1) the nanocrystal-based films had additional microporosity between TiO_2 nanocrystals, (2) the nanocrystals had smaller size than the polycrystalline domains in the sol-gel films, and (3) the poorly connected nanocrystals caused significant phonon scattering at the interfaces between nanocrystals. These examples show that structural factors indeed play a significant role in heat transfer though mesoporous materials. Since it has recently been revealed that some heat carriers in amorphous silica have propagating feature from both delicate experiments and atomistic simulation,[36,37] the similar confinement phenomenon of heat carriers may also exist in mesoporous silica.

In this study, we further elucidate the effects of structural factors on thermal conductivity of mesoporous amorphous SiO_2 with specific emphasis on the effects of (1) porosity, (2) silica nanotexture (*i.e.*, continuous vs. discontinuous framework), and (3) pore size. A wide variety of sol-gel and nanoparticle-based mesoporous amorphous SiO_2 thin films are synthesized and characterized in terms of porosity, pore size, film thickness, and thermal conductivity. The results are analyzed and compared to effective medium approximations. Physical arguments are provided to relate the thermal conductivity of mesoporous silica to its nanoscale architecture.

6.2 Results and Discussion

6.2.1 Structural characterization

In this study, a wide variety of mesoporous silica thin films with different frameworks, porosities, and pore sizes were prepared to examine the effects of the nanoscale architecture on their thermal conductivity. The mesoporous silica thin films were prepared by evaporation induced self-assembly (Scheme 6.1) as previously described. Different porosity, pore size, and wall thickness were achieved by varying the mass ratio of triblock copolymer template to silica.

Figure 6.1 shows typical SEM images of the sol-gel and nanoparticle-based mesoporous SiO_2 films. All films had well-developed mesoporosity with pore diameter ca. 10 nm throughout the structure, and a smooth crack-free surface. Sol-gel based films display a more ordered porous structure with a continuous SiO_2 framework (Figure 6.1a). On the other hand, the nanoparticle-based films had somewhat disordered pores and visible boundaries between the SiO_2 nanoparticles (Figure 6.1b).

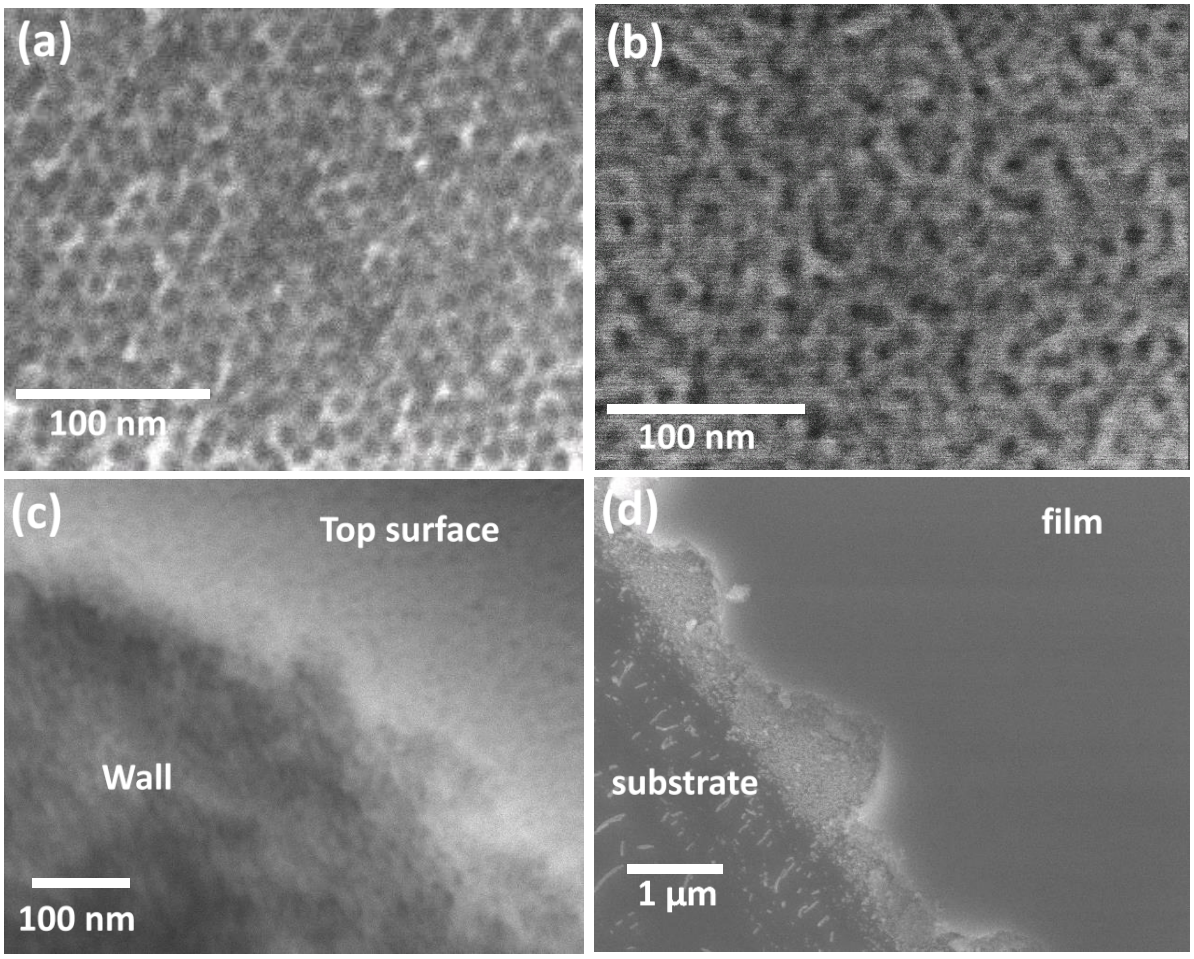

Figure 6.1: Typical scanning electron microscope images of mesoporous SiO_2 films. (a) sol-gel based and (b) nanoparticle-based mesoporous SiO_2 films. (c) zoomed in SEM of a cross-section area made by a razor blade cut in a nanoparticle-based mesoporous SiO_2 film. (d) zoomed out SEM of a representative mesoporous silica film on top of a Si substrate. SEM images show a three-dimensional porous structure and a crack-free smooth surface for both sol-gel and nanoparticle-based SiO_2 films.

Two-dimensional grazing-incidence small-angle X-ray scattering (2D-GISAXS) measurements were used to examine the mesoporous structure of the prepared films. Figure 6.2a shows a representative 2D-GISAXS pattern of mesoporous sol-gel SiO_2 thin films. The diffraction arc along the q_x- and q_y- directions indicate that the films had ordered porosity both in the plane of the substrate and in that perpendicular to it. Figure 6.2b shows the integrated spectra from the 2D-GISAXS pattern of Figure 6.2a in both the in-plane (parallel to the substrate, q_x) and out-of-plane (perpendicular to the substrate, q_y) directions. Both in-plane and out-of-plane SAXS featured a single diffraction peak indicating somewhat ordered porosity. These observations were consistent with the SEM images of the films (Figure 6.1). The in-plane diffraction peak had over twice higher intensity than the out-of-plane diffraction peak. This was due to the limited film thickness (< 800 nm), resulting in fewer scattering unit cells in the direction perpendicular to the substrate. The in-plane scattering peak was at a shorter distance q than the out-of-plane peak. Since $q = 2\pi/d$, the interplane spacing d between repeating unit cells of mesopores along the direction perpendicular to the substrate was shorter than in the direction parallel to the substrate. This indicates that during heat treatment the film shrunk more in the direction perpendicular to the substrate than in the in-plane direction, assuming that the as-synthesized film had originally uniform spacing in all directions. The in-plane diffraction peak was observed in nearly all samples, while the out-of-plane diffraction peak was missing for samples with $m_{poly}/m_{SiO2} > 2$ and $m_{poly}/m_{SiO2} < 0.4$. For $m_{poly}/m_{SiO2} > 2$, the pores along the direction perpendicular to the substrate experienced extreme shrinkage during heat treatment due to the high porosity obtained for large m_{poly}/m_{SiO2} ratios. This extreme shrinkage destroyed the order along the q_y-direction resulting in the featureless SAXS. On the other hand, for $m_{poly}/m_{SiO2} < 0.4$, the films were progressively thinner compared to the repeating distance d, resulting in broader and weaker out-of-plane diffraction peak, until its complete

disappearance. Figure 6.2c compares the in-plane interplane spacing $d_{in\text{-}plane}$ calculated from the position of the in-plane diffraction peak for F127-templated sol-gel and nanoparticle-based mesoporous SiO_2 films with different porosities. The interplane spacing $d_{in\text{-}plane}$ increased almost linearly with the porosity for both sol-gel and nanoparticle-based films, which indicates that the pores, and likely the pore walls, grew larger with the increasing porosity. On the other hand, sol-gel and nanoparticle-based mesoporous SiO_2 films displayed different values and trends in $d_{in\text{-}plane}/d_{out\text{-}of\text{-}plane}$ ratio as a function of porosity. In sol-gel based films, d_{in}/d_{out} ratio increased as porosity increases, as the films with higher porosity shrank more in the perpendicular direction to the substrate, leading to a smaller d_{out}. However, in nanoparticle-based films, d_{in}/d_{out} ratio was relatively independent of porosity, likely due to that the pre-formed nanoparticles based network underwent less shrinkage. Overall the d_{in}/d_{out} ratios at all porosities were higher in sol-gel based films than those in nanoparticle-based films due to the difference in shrinkage perpendicular to the substrate.

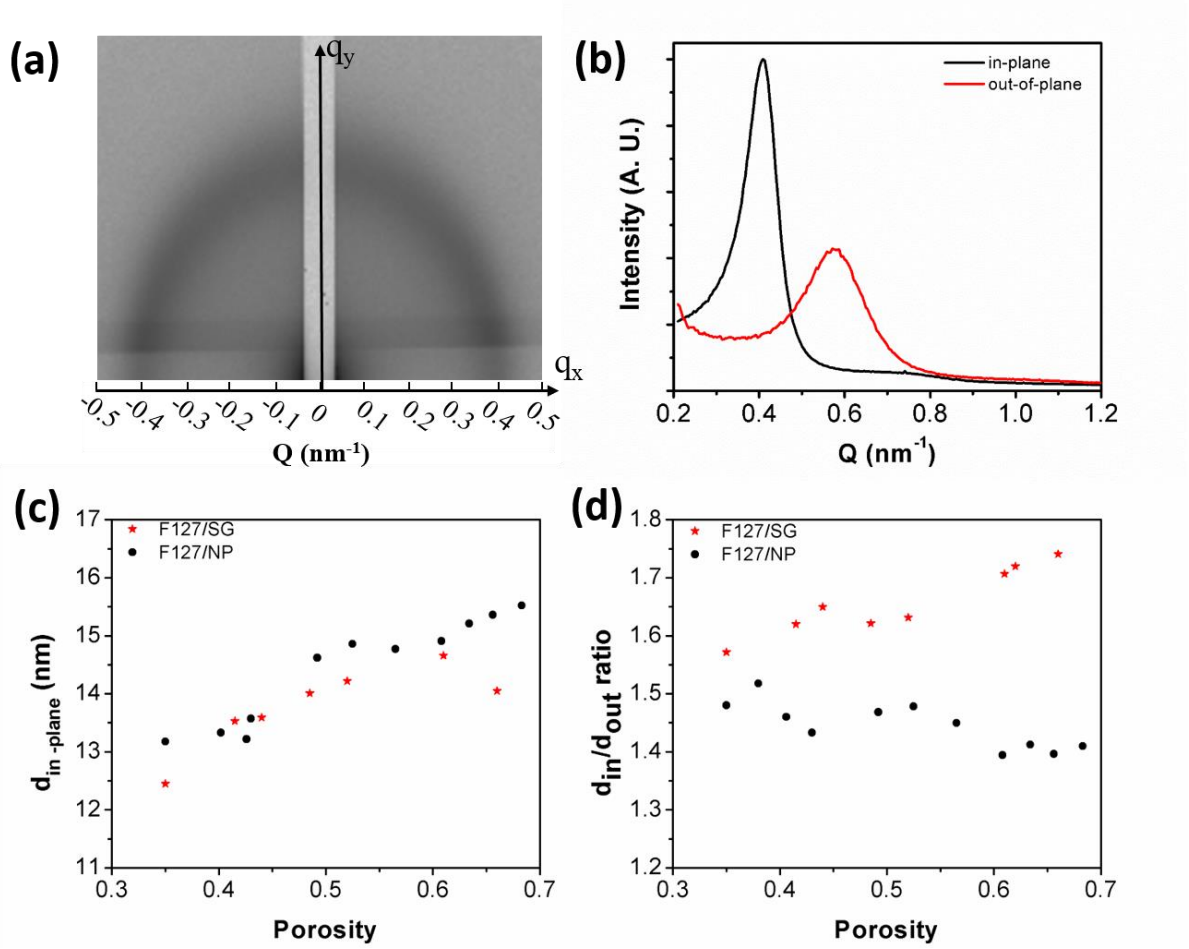

Figure 6.2: Small angle X-ray scattering of SiO_2 sol-gel and nanoparticle-based films. (a) a representative 2D-GISAXS pattern of a sol-gel based mesoporous SiO_2 film. (b) Integrated intensity spectra converted from a 2D-GISAXS pattern along the q_x- and q_y-directions corresponding to in-plane and out-of-plane scattering, respectively. (c) in-plane distance as a function of porosity and (d) ratio of in-plane distance/out-of-plane distance as a function of porosity for F127-templated sol-gel (SG) and nanoparticle-based (NP) films.

The porosity and pore size were further analyzed by ellipsometric porosimetry using toluene as an adsorbent.[38] Figure 6.3 shows adsorption/desorption isotherms and pore size distribution for (a) sol-gel and (b) nanoparticle-based SiO_2 films templated with Pluronic P123 for m_{poly}/m_{SiO2} = 1.5. Both isotherms were of type IV with H2(b) hysteresis loop according to the IUPAC classification.[39,40] Type IV isotherms demonstrate the presence of mesopores while H2(a) hysteresis loop indicates a complex pore structure with pore blocking. The steep adsorption

increase at high relative pressures, corresponding to capillary condensation in mesopores, suggests a fairly narrow pore size distribution.[41] The derivative of adsorption curve gives the size of the pores (cage) and the derivative of desorption curve reveals the size of the necks connecting the spherical pores.[26] Both films had similar porosity (≈65%) and pore size (10–14 nm for cage diameter and 7-9 nm for neck diameter). The sol-gel film displayed an isotherm step at relative pressure ≈0.15 P/P_0 that was not present in the nanoparticle-based films. The step corresponded to micropores with diameter ≈3 nm created inside the mesopore walls by the long block copolymer chains.[41,42]

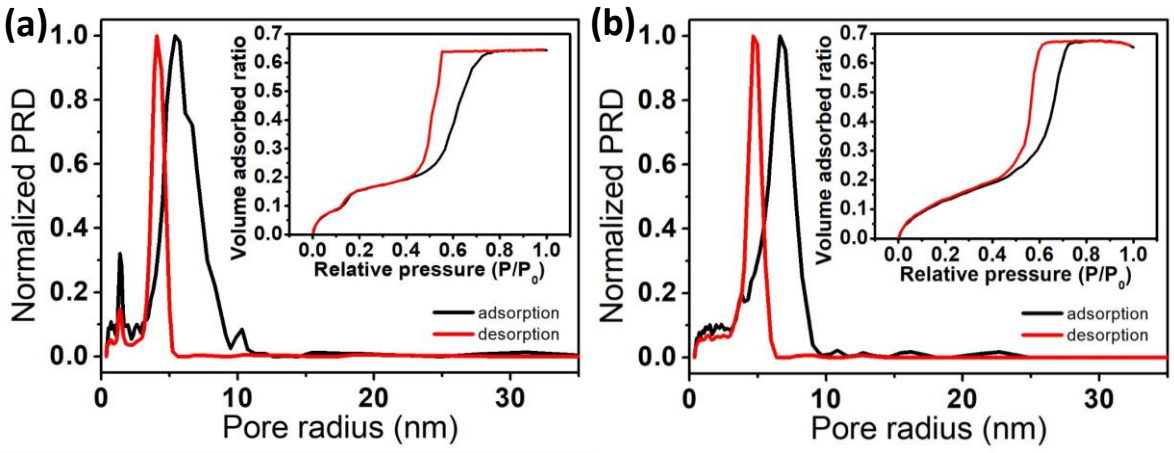

Figure 6.3: Typical isotherms and pore size distributions obtained with ellipsometric porosimetry for (a) sol-gel and (b) nanoparticle-based SiO_2 films with a 1.5 g/g P123 to SiO_2 ratio.

Figures 6.4a and 6.4b summarize the dependence of porosity on the m_{poly}/m_{SiO2} ratio in sol-gel and nanoparticle-based mesoporous SiO_2 films, respectively. The porosity in both sol-gel and nanoparticle-based films gradually increased up to 70% with increasing amount of polymer up to mass ratio $m_{polymer}/m_{SiO2} > 2$ g/g. Further increase in $m_{polymer}/m_{SiO2}$ resulted in polymer aggregation on the surface and more shrinkage during heating instead of higher porosity. The sol-gel based SiO_2 system displays a wide range of porosity from 0% to70% as any addition of polymer beyond

the critical micelle concentration results in porosity increase (until the saturation point). By contrast, the porosity of the nanoparticle-based films featured a lower limit around 35% due to the intrinsic porosity between randomly packed nanoparticles.

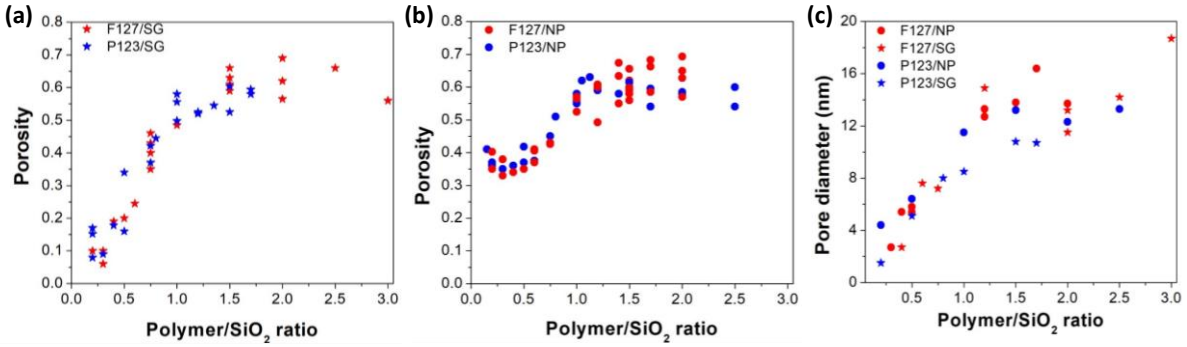

Figure 6.4: Porous structure characterized by ellipsometric porosimetry. Porosity as a function of polymer/SiO_2 ratio of (a) sol-gel (SG) and (b) nanoparticle-based (NP) mesoporous SiO_2 films. (c) Average pore diameter as a function of polymer/SiO_2 ratio in Pluronic surfactant-templated porous sol-gel and nanoparticle-based SiO_2 mesoporous films.

The average pore diameter of mesoporous SiO_2 films also increased with the increasing m_{poly}/m_{SiO2}, as shown in Figure 6.4c. This was in agreement with the increasing $d_{in\text{-}plane}$ spacing observed in the SAXS data. In addition, the average pore diameter was larger in films templated with Pluronic F127 than in those templated with Pluronic P123, for a given m_{poly}/m_{SiO2} ratio. This was due to the larger molecular weight of Pluronic F127 (M_w=12,700 Da) than Pluronic P123 (M_w=5800 Da). Interestingly, despite the fact that the porosity no longer changed for m_{poly}/m_{SiO2} > 2 g/g, the average pore size kept on increasing. Table 6.1 summarizes the porosity, pore diameter and film thickness of the various SiO_2 mesoporous thin films investigated.

6.2.2 Thermal conductivity measurements

Table 6.1 lists out the thermal conductivity measurements at room temperature and under vacuum for the various mesoporous SiO_2 films synthesized.

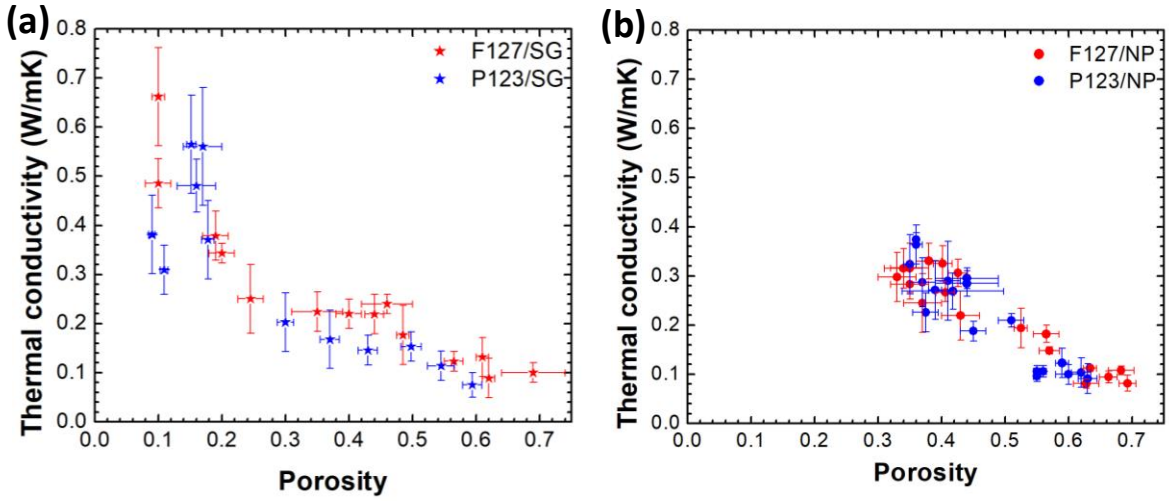

Figure 6.5: Thermal conductivity as a function of porosity for F127 and P123 template (a) SiO_2 sol-gel (SG) and (b) SiO_2 nanoparticle-based (NP) films measured in vacuum condition, showing no noticeable difference for different template at the same porosity.

Effect of porosity

Previous studies on thermal transport in mesoporous silica mostly focused on a narrow range of porosity.[27,28] Here, the thermal conductivity of mesoporous silica with a wide range of porosity was systematically studied. We also report, for the first time, the thermal conductivity of nanoparticle-based mesoporous SiO_2 films. Figure 6.5 shows the thermal conductivity as a function of porosity for both sol-gel based and nanoparticle-based mesoporous SiO_2 films: As expected, the thermal conductivity decreased with increasing porosity.[27,43] Thermal conductivity below 0.1 W/mK was achieved for porosity larger than 60% in both sol-gel and nanoparticle-based SiO_2 mesoporous films.

As the heat is carried by non-propagating vibrational modes whose coherent lengths remain much smaller than the silica wall thickness, effective medium approximations (EMAs) can be used to model the effect of porosity.[44] Figure 6.6 plots the thermal conductivity of F127 templated sol-gel based mesoporous silica together with that of dense silica,[45] hydrogen-silsesquioxane (HSQ),[44] cubic and hexagonal mesoporous silica,[27] silica xerogel,[7] silica aerogel[46] as well as predictions

from several EMAs for the effective thermal conductivity of two phase media.[47] It is interesting to note that the thermal conductivity of the present mesoporous silica follows a similar porosity dependency as those previously reported despite major differences in synthesis and nanoscale architecture.

To understand the strong porosity dependence of thermal conductivity, we first compared our data with EMAs based on classic heat conduction theory. For example, Russell's model was used for predicting the effective thermal conductivity κ_{eff} of bulk materials with spherical pores and expressed as[48]

$$\text{Russell's model} \quad \kappa_{eff} = \kappa_{SiO_2} \frac{\left(1-{\phi_p}^{2/3}\right)}{\left(1-{\phi_p}^{2/3}+\phi_p\right)} \tag{1}$$

where ϕ_p is the porosity and κ_{SiO_2} is the thermal conductivity of bulk SiO_2. However, this prediction strongly overestimated the thermal conductivity of the different mesoporous silica, likely due to the major difference in morphology. The Clausius-Mossotti (CM) model and differential-effective-medium (DEM) theory have also been applied to predict the effective thermal conductivity of porous solid with ordered arrangement of identical pores[44] and are expressed as

$$\text{CM model} \quad \kappa_{eff} = \kappa_{SiO_2} \frac{(1-\phi_p)}{(1+0.5\phi_p)} \tag{2}$$

$$\text{DEM model} \quad \kappa_{eff} = \kappa_{SiO_2}(1-\phi_p)^{1.5} \tag{3}$$

Unfortunately, both of these EMAs failed to capture the porosity dependence. Possible reasons include the fact that they ignore the pore shape, pore size, and the transport mechanisms of heat carrier in mesoporous amorphous silica. Another model, which combines the classical series model and parallel model $\kappa_{eff} = \kappa_{SiO_2}(1-\phi_p)$, called porosity weighted simple medium (PWSM) model has also been used to account for the porous structural parameters by using a fitting

parameter *x*.[46] Considering the disperse phase in the pores to be vacuum, the PWSM simplifies to[27]

$$\text{PWSM model} \quad \kappa_{eff} = \kappa_{SiO_2}(1-\phi_p)(1-{\phi_p}^{x}) \tag{4}$$

Fitting the PWSM to our experimental measurements on F127-templated sol-gel films yielded x = 0.27, which was slightly larger than the value of x = 0.17 reported by Coquil *et al.*[27] The difference was likely due to the narrower range of porosity (25-45%) compared with the present study (10-60%). Although it is difficult to physically interpret the meaning of x, this model is useful in predicting the thermal conductivity of mesoporous silica in the porosity range 10-60%.

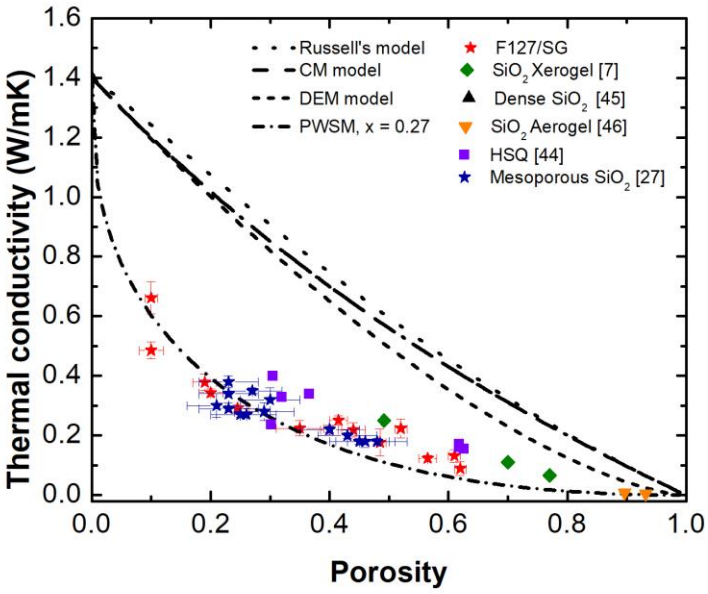

Figure 6.6: Thermal conductivity as a function of porosity for F127 Pluronic surfactant templated SiO_2 sol-gel and nanoparticle-based films measured in vacuum condition, compared with various data for mesoporous silica reported in the literature[7,27,44–46] and commonly used EMAs.

Effect of framework structure

The effects of solid framework morphology on the thermal transport in mesoporous silica were also explored by comparing the thermal conductivity of sol-gel and nanoparticle-based mesoporous

SiO_2 films. As shown in Figure 6.7, although both kinds of mesoporous films feature decreasing thermal conductivity with increasing porosity, there are still some observable difference. First, near the lower porosity limit (~35%), the thermal conductivity of nanoparticle-based silica films was about 30% higher than that of sol-gel based films. On the other hand, for porosity above 45%, the difference in thermal conductivity between these two types of mesoporous framework was negligible. The PWSM model was fitted for each type of mesoporous SiO_2 thin films yielding x = 0.27 for sol-gel and x = 0.42 for nanoparticle-based SiO_2 mesoporous films. In brief, the nanoparticle-based films offer more through-plane heat conduction pathways than the sol-gel films. In nanoparticle-based films, the size of connections between nanoparticles are determined by the diameter of each SiO_2 nanoparticle and thus porosity independent. Since the size of nanoparticles is uniform throughout the network, the heat conduction has equal probability to go along jointed nanoparticle chains, as modeled by the parallel model. On the other hand, the sol-gel mesoporous films feature thin necks whose size decreases with decreasing pore size and increasing porosity. The thin necks in sol-gel network contribute significantly to the thermal resistance resulting in low thermal conductivity in sol-gel mesoporous SiO_2 films at lower porosity.

Moreover, heat carriers confinement in the nanostructures is also likely responsible for the difference in thermal conductivity between sol-gel and nanoparticle-based SiO_2 films. Figure 6.8 shows TEM images of sol-gel and nanoparticle-based mesoporous SiO_2 films to illustrate the difference in frameworks between the two types of mesoporous materials. In the sol-gel mesoporous film, SiO_2 existed in a continuous molecular network where the wall thickness was almost uniform and determined by both the pore size and porosity. In the nanoparticle-based film, individual SiO_2 nanoparticles were connected and partially fused, with walls formed by at least one or multiple stacking of nanoparticles. As the pore size increases with porosity, in sol-gel mesoporous films, the

wall thickness decreases and can be smaller than the nanoparticle size. This, in turn, reduces the thermal conductivity of sol-gel mesoporous films due to enhanced heat carrier scattering at the wall/pore interface. Meanwhile, the number of neighboring nanoparticles for each nanoparticle in nanoparticle-based films decreases with increasing porosity. The number of nanoparticles with only one neighbor increases with rising porosity. The emergence of such dead end for heat conduction reduces the effective thermal conductivity of nanoparticle-based films. Therefore, at high porosity (>70%), the difference of thermal conductivity between so-gel based and nanoparticle-based films becomes small.

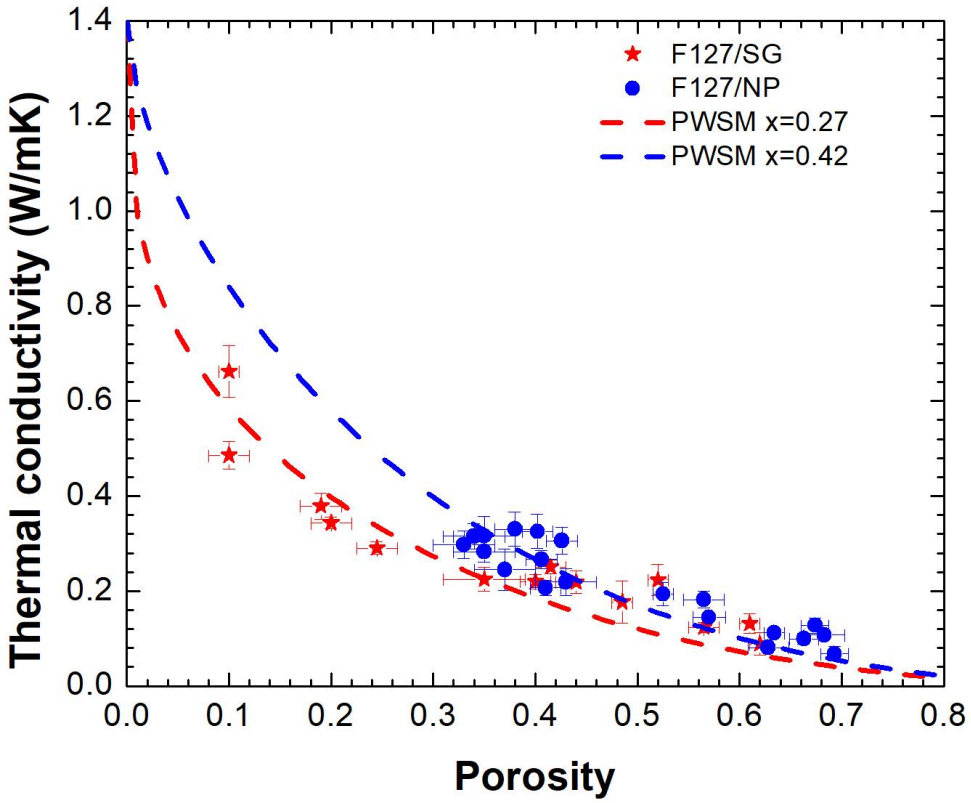

Figure 6.7: Thermal conductivity as a function of porosity for Pluronic surfactant templated SiO_2 sol-gel (SG) and nanoparticle-based (NP) films measured under vacuum with PWSM model fitting.

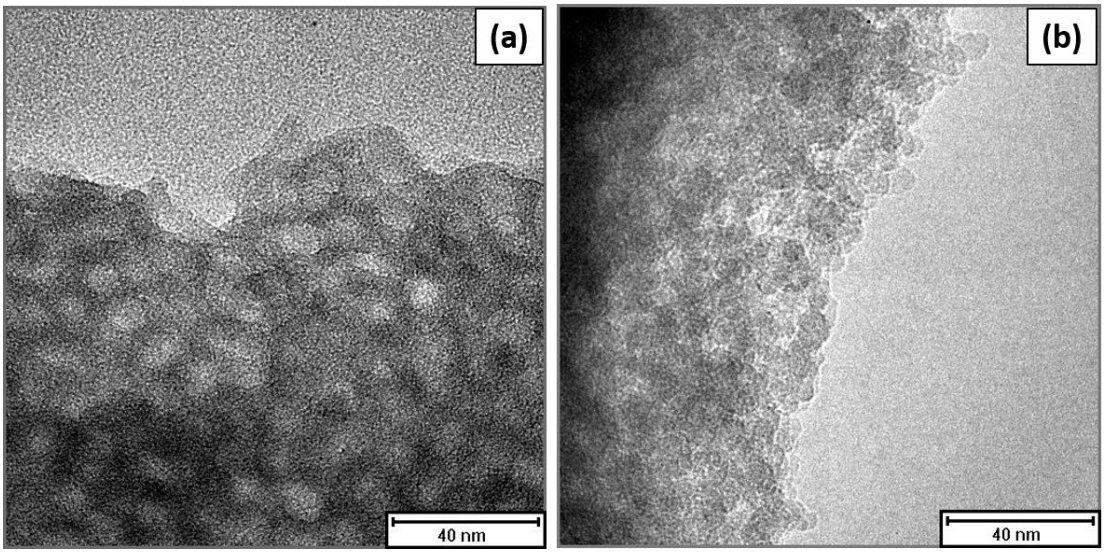

Figure 6.8: Transmission electron microscopy images of F127 templated (a) sol-gel and (b) nanoparticle-based SiO_2 mesoporous films. The images clearly show that the sol-gel network was continuously connected, while the nanoparticle-based films were composed of individual nanoparticles overlapping each other.

Effect of pore size

Figure 6.5 shows a stronger decrease in thermal conductivity with porosity in sol-gel mesoporous SiO_2 films compared with nanoparticle-based films. Indeed, Figure 6.5a indicates that Pluronic F127-templated mesoporous SiO_2 films had a larger thermal conductivity than those template with P123. Since Pluronic F127 forms bigger micelles due its larger molecular weight, it typically forms larger pores. This suggests that sol-gel based SiO_2 films with smaller pore size have lower thermal conductivity. For a given porosity, smaller pore size is associated with thinner wall and thus provides more scattering center and fewer conduction pathways for heat carriers. On the other hand, nanoparticle-based SiO_2 films showed almost no effect of pore size on the thermal conductivity. This is most likely due to the fact that in the nanoparticle-based framework, the individual nanoparticles are the dominating scattering center, and the scattering effect is not dependent on the number of nanoparticles composing the pore walls. This is consistent with the

stronger weight of the parallel model in the PWSM fitting for nanoparticle-based SiO_2 mesoporous films.

6.3. Conclusions

This paper presented synthesis, characterization, and cross-plane thermal conductivity measurements at room temperature of sol-gel and nanoparticle-based mesoporous amorphous silica thin films with various thicknesses, pore sizes, and porosities. The following conclusions could be drawn:

(1) Porosity plays a dominating role in lowering the thermal conductivity in both sol-gel and nanoparticle-based mesoporous silica films. The thermal conductivity depends nonlinearly on porosity. The average thermal conductivity of mesoporous SiO_2 films with porosity of 60% was measured as 0.1 ± 0.03 W/m.K at room temperature.

(2) The building block of the porous framework affects how thermal conductivity changes with porosity. The sol-gel network is interconnected with thin necks that account for the low thermal conductivity in sol-gel based SiO_2 films at lower porosity, while in the nanoparticle-based film, the size of connections between SiO_2 nanoparticles are porosity independent. The minimum thickness of the necks must be larger than the diameter of the nanoparticle.

(3) For a given porosity, the thermal conductivity of sol-gel mesoporous SiO_2 decreases with decreasing pore size. This was due to thinner walls associated with smaller pores, resulting in stronger scattering of heat carriers at the wall surfaces. On the other hand, the pore size had no effect on the thermal conductivity of nanoparticle-based mesoporous SiO_2 films as the mean free path of heat carriers corresponded to the nanoparticle diameter and was independent of the pore size.

Table 6.1: Porosity, Pore Size, Film Thickness and Thermal Conductivity of F127 and P123 Templated Sol-Gel and Nanoparticle-Based Mesoporous SiO_2 Films

Sample No.	Surfactant	Building block	Porosity	Pore diameter (nm)	Film thickness (nm)	thermal conductivity, vac. (W/mK)
1	F127	Sol-gel	0.69 ± 0.05	18.2	247	0.10 ± 0.02
2	F127	Sol-gel	0.64 ± 0.02	14.2	367	0.09 ± 0.02
3	F127	Sol-gel	0.61 ± 0.01		433	0.13 ± 0.02
4	F127	Sol-gel	0.60 ± 0.03	13.6	375	0.12 ± 0.01
5	F127	Sol-gel	0.49 ± 0.01		290	0.18 ± 0.04
6	F127	Sol-gel	0.46 ± 0.04	8.7	361	0.24 ± 0.04
7	F127	Sol-gel	0.44 ± 0.02	7.5	241	0.22 ± 0.02
8	F127	Sol-gel	0.4 ± 0.02	7.6	213	0.22 ± 0.02
9	F127	Sol-gel	0.35 ± 0.04	7.2	229	0.22 ± 0.03
10	F127	Sol-gel	0.27 ± 0.03		165	0.25 ± 0.04
11	F127	Sol-gel	0.2 ± 0.02		203	0.34 ± 0.01
12	F127	Sol-gel	0.19 ± 0.02	3.5	241	0.38 ± 0.03
13	F127	Sol-gel	0.1 ± 0.02		158	0.49 ± 0.03
14	F127	Sol-gel	0.1 ± 0.01		137	0.66 ± 0.05
15	P123	Sol-gel	0.59 ± 0.02	10.7	473	0.08 ± 0.02
16	P123	Sol-gel	0.55 ± 0.02	8.5	385	0.11 ± 0.01
17	P123	Sol-gel	0.50 ± 0.02		378	0.15 ± 0.02
18	P123	Sol-gel	0.43 ± 0.02	7	275	0.15 ± 0.02
19	P123	Sol-gel	0.37 ± 0.05		206	0.17 ± 0.06
20	P123	Sol-gel	0.3 ± 0.02	5.1	182	0.20 ± 0.03
21	P123	Sol-gel	0.18 ± 0.01		367	0.37 ± 0.05
22	P123	Sol-gel	0.17 ± 0.03	2.7	317	0.56 ± 0.07
23	P123	Sol-gel	0.16 ± 0.03		503	0.48 ± 0.05
24	P123	Sol-gel	0.15 ± 0.01		537	0.56 ± 0.05
25	F127	NP	0.69 ± 0.02	18.8	772	0.08 ± 0.02
26	F127	NP	0.66 ± 0.02		657	0.09 ± 0.01
27	F127	NP	0.64 ± 0.03	16.4	500	0.11 ± 0.01
28	F127	NP	0.63 ± 0.01		470	0.11 ± 0.01
29	F127	NP	0.63 ± 0.02	16.4	604	0.08 ± 0.01
30	F127	NP	0.57 ± 0.02		431	0.15 ± 0.01
31	F127	NP	0.56 ± 0.02	12.6	363	0.18 ± 0.02
32	F127	NP	0.53 ± 0.01	11.5	559	0.19 ± 0.02
33	F127	NP	0.43 ± 0.03		414	0.22 ± 0.03
34	F127	NP	0.43 ± 0.02		561	0.31 ± 0.03
35	F127	NP	0.41 ± 0.02		472	0.27 ± 0.02
36	F127	NP	0.37 ± 0.03		396	0.24 ± 0.04
37	F127	NP	0.35 ± 0.03	5.8	406	0.28 ± 0.02

38	F127	NP	0.34 ± 0.03	5.4	400	0.32 ± 0.03
39	F127	NP	0.33 ± 0.03	4.5	374	0.30 ± 0.03
40	F127	NP	0.35 ± 0.03		438	0.32 ± 0.04
41	P123	NP	0.63 ± 0.02		417	0.09 ± 0.01
42	P123	NP	0.62 ± 0.02	13.2	466	0.10 ± 0.02
43	P123	NP	0.6 ± 0.02		506	0.10 ± 0.01
44	P123	NP	0.59 ± 0.01	12.3	370	0.12 ± 0.02
45	P123	NP	0.55 ± 0.01		319	0.11 ± 0.01
46	P123	NP	0.56 ± 0.01	9.7	712	0.11 ± 0.01
47	P123	NP	0.55 ± 0.01	10.3	239	0.10 ± 0.01
48	P123	NP	0.51 ± 0.02		522	0.21 ± 0.01
49	P123	NP	0.45 ± 0.02		518	0.19 ± 0.01
50	P123	NP	0.44 ± 0.05		340	0.24 ± 0.03
51	P123	NP	0.44 ± 0.05	5.9	758	0.25 ± 0.03
52	P123	NP	0.42 ± 0.08		403	0.27 ± 0.04
53	P123	NP	0.41 ± 0.02		424	0.29 ± 0.05
54	P123	NP	0.39 ± 0.01		490	0.27 ± 0.04
55	P123	NP	0.37 ± 0.02		407	0.29 ± 0.04
56	P123	NP	0.35 ± 0.01		437	0.32 ± 0.03
57	P123	NP	0.36 ± 0.02	4.4	454	0.36 ± 0.02

6.5 Experimental Methods

6.5.1 Materials

The following materials were obtained from commercial suppliers and used without further purification: colloidal suspension of SiO_2 nanoparticles (15 wt%, Nalco 2326, ammonia-stabilized colloidal silica, d = 5 nm, Nalco Chemical Company), triblock copolymer Pluronic P123 ($EO_{20}PO_{70}EO_{20}$, M_w = 5800 Da, BASF), triblock copolymer Pluronic F127 ($EO_{100}PO_{65}EO_{100}$, M_w = 12600 Da, BASF), tetraethyl orthosilicate (98%, Acros Organics), hydrochloric acid (Certified ACS Plus, Fisher Scientific), ethanol (200 proof, Rossville Gold Shield).

6.5.2 Synthesis

Both sol-gel and nanoparticle-based mesoporous SiO_2 thin films were prepared by evaporation-induced self-assembly (Scheme 6.1). Tetraethyl orthosilicate (TEOS) was used as a

silica precursor for the sol-gel films while pre-made SiO_2 nanoparticles were used as building blocks for the nanoparticle-based films. In both instances, triblock copolymers Pluronic P123 or Pluronic F127 were used as the structure-directing agents. The solution containing the precursors and the block copolymers was spin-coated on a silicon substrate. Upon evaporation, the system self-assembled into an organic–inorganic nanocomposite. Subsequently, the organic–inorganic nanocomposite films were calcined to remove the block copolymer and develop the mesoporous structure.

Nanoparticle-based mesoporous SiO_2 films

First, a stock solution of polymer was made by dissolving 0.678 g of Pluronic P123 or Pluronic F127 in 3 mL deionized water. Second, the stock polymer solution was mixed with the colloidal suspension of SiO_2 nanoparticles to produce a solution with polymer/SiO_2 mass ratio m_{poly}/m_{SiO2} between 0.1 and 3 g/g. Then, 80 μL of the polymer-silica solution was spin-coated onto a 1" × 1" Si substrates. The film's thickness was adjusted by controlling the spin speed. The dried films were calcined in air at 350 ℃ for 30 min using 2 °C/min temperature ramp to remove the polymer. Nanoparticle-based SiO_2 powder was also synthesized from the same solutions for heat capacity measurements. Instead of spin-coating, the solutions were evaporated in a Petri dish at ambient condition for a day and collected in powdered form after calcination at 350 ℃ for 3 hour in oxygen.

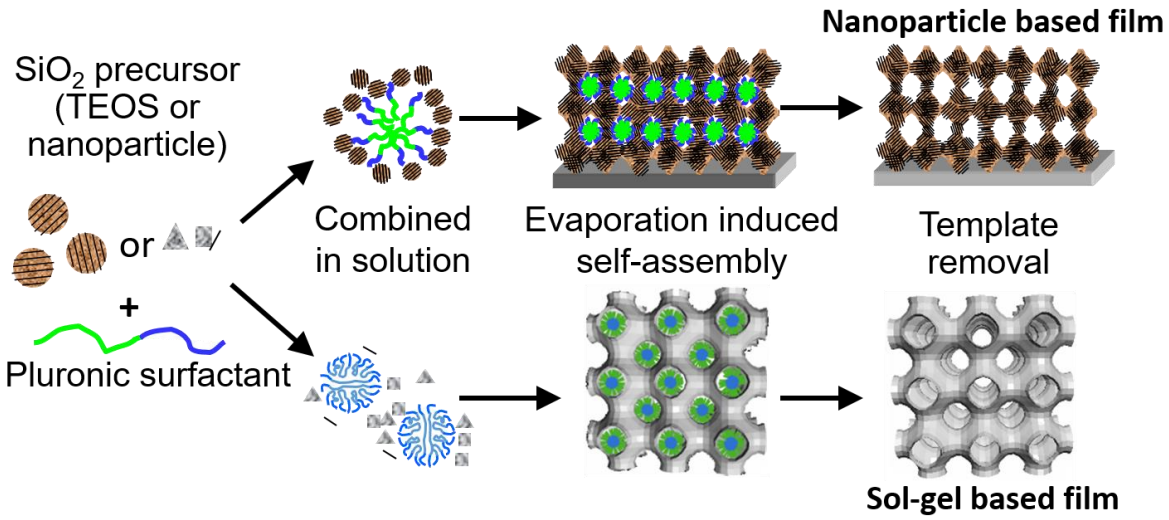

Scheme 6.1: Synthesis of SiO_2 sol-gel and nanoparticle-based films via evaporation induced self-assembly, using pluronic surfactant as template and TEOs or SiO_2 nanoparticles as precursors.

Sol-gel based mesoporous SiO_2 films

The method was adapted from the literature.[49] First, 25 mg of Pluronic F127 was dissolved in 0.6 mL of ethanol and 0.16 mL of 0.05 M HCl. A certain amount of tetraethyl orthosilicate (TEOS) was added to the mixture to achieve a polymer to SiO_2 mass ratio m_{poly}/m_{SiO2} between 0.1 and 3. Then, 80 µL of the polymer-silica solution was spin-coated onto a 1" × 1" Si substrates. The film thickness was adjusted by controlling the spin speed. The dried films were calcined in air at 350 ℃ for 30 min using 2 °C/min temperature ramp to remove the polymer. Sol-gel SiO_2 powder was made from the same solutions for heat capacity measurements. Instead of spin-coating, the solutions were evaporated in a Petri dish at ambient condition for a day and collected in powdered form after calcination at 350 ℃ for 3 hour in oxygen.

6.4.3 Structural characterization

Scanning Electron Microscopy (SEM) images were obtained using a model JEOL JSM-6700F field emission electron microscope with 5 kV accelerating voltage and secondary electron detector

configuration. Transmission Electron Microscopy (TEM) images were obtained using a Technai G^2 TF20 High-Resolution EM, CryoEM and CryoET (FEI) at an accelerating voltage 200 kV and a TIETZ F415MP 16 megapixel 4k×4k CCD detector. Two-dimensional grazing incidence small-angle x-ray scattering (2D-GISAXS) data were collected at the Stanford Synchrotron Lightsource (SSRL) using beamlines 1-5 with a wavelength of 0.1033 nm operated at an X-Ray energy of 12.002 keV and detector distance of 2.870 m using a Rayonix-165 CCD detector. The data was then calibrated and reduced using the Nika package from Igor Pro.[50] Ellipsometric porosimetry was performed on a PS-1100 instrument from Semilab using toluene as the adsorbate to quantify porosity and pore size. The instrument used a UV-visible CCD detector adapted to a grating spectrograph to analyze the signal reflected by the sample. The light source was a 75 W Hamamatsu Xenon lamp and the measurements were performed in the spectral range from 1.25–4.5 eV. Data analysis was performed using the associated Spectroscopic Ellipsometry Analyzer software assuming the pores were cylindrical. An optical reflectance based method was also used to verify the porosity. The experimental spectral normal-hemispherical reflectance $R_{exp,\lambda}$ was measured with a Shimadzu UV3101 PC UV-VIS spectrophotometer equipped with a Shimadzu ISR3000 integrating sphere. The reference intensity was measured using a high specular reflection standard mirror by Ocean Optics (NIST certified STAN-SSH). The reflectance was measured in the visible range between 400 and 800 nm with a 1 nm spectral resolution.

6.4.4 Thermal properties characterization

Since the thickness of mesoporous silica films was less than 1 μm thick, only a few thermal characterization techniques were suitable including the 3ω[27,51] and time-domain thermoreflectance (TDTR)[28,52] methods. Considering the simpler fabrication processes and previously reported success of TDTR for extremely porous silica aerogel[28], TDTR was used here for systematically

investigating thermal conductivity of the various mesoporous silica films synthesized (Scheme 6.2). The detailed working principles and experimental setup can be found elsewhere and need not be repeated.[53–56] In brief, a thin aluminum film (80 nm) was deposited by e-beam evaporation on the top surface of the samples. It served as both a transducer to convert laser energy to thermal energy and a temperature sensor. The absorbed energy from the pump beam at 400 nm wavelength led to an instantaneous temperature rise. The probe beam at 800 nm wavelength was used to continuously detect temperature decay by measuring the reflection portion using a photodiode. The delay time between pump pulse and probe pulse can be controlled with temporal resolution higher than sub-picosecond. Next, the full transient decay curve from -100 ps to 5000 ps was fitted with a thermal diffusion model to obtain the thermal conductivity k of the sample.[52] To account for potential differences in the local thermal conductivity induced by variations in the nanoscale random network of SiO_2, large laser spot size of 20 μm in diameter was used. Similarly, to correct for the macroscale inhomogeneity of the mesoporous films and to ensure the reliability of the thermal conductivity data, TDTR measurements were repeated at ten different locations on a 1 cm x 1 cm surface area of the sample. Before all TDTR measurements, the samples were dehydrated by heating on a hot plate at 150 ^{o}C for more than 12 hours. The thermal conductivity of dehydrated samples was measured in a vacuum chamber with pressure less than 1 Pa at room temperature.

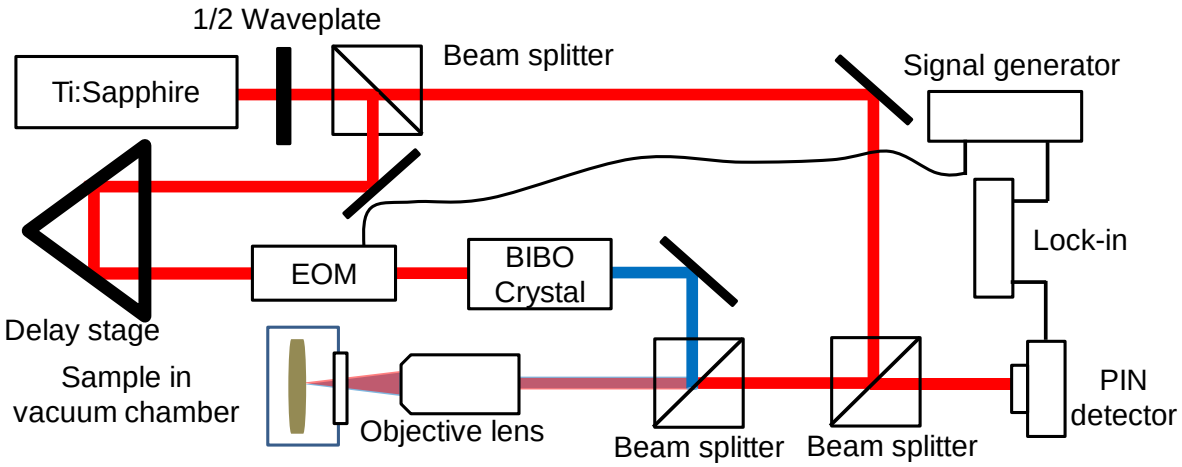

Scheme 6.2: Experimental setup of time-domain thermoreflectance (TDTR) method used for thermal conductivity measurement on mesoporous silica films on Si substrate.

The specific heat capacity of the different mesoporous power SiO_2 samples with different porosity was measured using a Perkin Elmer® DSC 8000, a dual furnace differential scanning calorimeter equipped with an IntraCooler. The method was reported elsewhere and need not be repeated.[57] In brief, the samples were prepared in Al pans with vented covers to facilitate water loss at high temperatures. The specific heat capacity of each sample was measured using a step scan isothermal method from 20 °C to 30 °C with a 5 °C/min scan and 1.5 min hold at every 1 °C intervalThey were used to retrieve the thermal conductivity from the thermal effusivity measurements obtained from TDTR.

6.5 References

(1) Maex, K.; Baklanov, M. R.; Shamiryan, D.; Lacopi, F.; Brongersma, S. H.; Yanovitskaya, Z. S. Low Dielectric Constant Materials for Microelectronics. *J. Appl. Phys.* **2003**, *93* (11), 8793–8841.

(2) Peercy, P. S. The Drive to Miniaturization. *Nature* **2000**, *406*, 1023.

(3) Veres, J.; Ogier, S. D.; Leeming, S. W.; Cupertino, D. C.; Mohialdin Khaffaf, S. Low-k

Insulators as the Choice of Dielectrics in Organic Field-effect Transistors. *Adv. Funct. Mater.* **2003**, *13* (3), 199–204.

(4) Vigliante, A.; Kasper, N.; Brechbuehl, J.; Nolot, E. Applications of X-Ray Characterization for Advanced Materials in the Electronics Industry. *Metall. Mater. Trans. A* **2010**, *41* (5), 1167–1173.

(5) Powell, M. J.; Quesada-Cabrera, R.; Taylor, A.; Teixeira, D.; Papakonstantinou, I.; Palgrave, R. G.; Sankar, G.; Parkin, I. P. Intelligent Multifunctional $VO_2/SiO_2/TiO_2$ Coatings for Self-Cleaning, Energy-Saving Window Panels. *Chem. Mater.* **2016**, *28* (5), 1369–1376.

(6) Jain, A.; Rogojevic, S.; Ponoth, S.; Gill, W. N.; Plawsky, J. L.; Simonyi, E.; Chen, S.-T.; Ho, P. S. Processing Dependent Thermal Conductivity of Nanoporous Silica Xerogel Films. *J. Appl. Phys.* **2002**, *91* (5), 3275–3281.

(7) Hu, C.; Morgen, M.; Ho, P. S.; Jain, A.; Gill, W. N.; Plawsky, J. L.; Wayner, P. C. Thermal Conductivity Study of Porous Low- *K* Dielectric Materials. *Appl. Phys. Lett.* **2000**, *77* (1), 145–147.

(8) Jin, C.; Luttmer, J. D.; Smith, D. M.; Ramos, T. A. Nanoporous Silica as an Ultralow-K Dielectric. *MRS Bull.* **1997**, *22* (10), 39–42.

(9) Koebel, M.; Rigacci, A.; Achard, P. Aerogel-Based Thermal Superinsulation: An Overview. *J. Sol-Gel Sci. Technol.* **2012**, *63* (3), 315–339.

(10) Deng, Z.; Wang, J.; Wu, A.; Shen, J.; Zhou, B. High Strength SiO_2 Aerogel Insulation. *J. Non. Cryst. Solids* **1998**, *225*, 101–104.

(11) Eggiman, B. W.; Tate, M. P.; Hillhouse, H. W. Rhombohedral Structure of Highly Ordered and Oriented Self-Assembled Nanoporous Silica Thin Films. *Chem. Mater.* **2006**, *18* (3),

723–730.

(12) Alberius, P. C. A.; Frindell, K. L.; Hayward, R. C.; Kramer, E. J.; Stucky, G. D.; Chmelka, B. F. General Predictive Syntheses of Cubic, Hexagonal, and Lamellar Silica and Titania Mesostructured Thin Films. *Chem. Mater.* **2002**, *14* (8), 3284–3294.

(13) Lu, Y.; Ganguli, R.; Drewien, C. A.; Anderson, M. T.; Brinker, C. J.; Gong, W.; Guo, Y.; Soyez, H.; Dunn, B.; Huang, M. H. Continuous Formation of Supported Cubic and Hexagonal Mesoporous Films by Sol–gel Dip-Coating. *Nature* **1997**, *389* (6649), 364.

(14) Zhao, D.; Feng, J.; Huo, Q.; Melosh, N.; Fredrickson, G.; Chmelka, B.; Stucky, G. Triblock Copolymer Syntheses of Mesoporous Silica with Periodic 50 to 300 Angstrom Pores. *Science (80-.).* **1998**, *279* (5350), 548–552.

(15) Hedrick, J. L.; Miller, R. D.; Hawker, C. J.; Carter, K. R.; Volksen, W.; Yoon, D. Y.; Trollsås, M. Templating Nanoporosity in Thin-film Dielectric Insulators. *Adv. Mater.* **1998**, *10* (13), 1049–1053.

(16) Venkateswara Rao, A.; Pajonk, G. M.; Haranath, D. Synthesis of Hydrophobic Aerogels for Transparent Window Insulation Applications. *Mater. Sci. Technol.* **2001**, *17* (3), 343–348.

(17) Wei, T.; Chang, T.; Lu, S.; Chang, Y. Preparation of Monolithic Silica Aerogel of Low Thermal Conductivity by Ambient Pressure Drying. *J. Am. Ceram. Soc.* **2007**, *90* (7), 2003–2007.

(18) Jelle, B. P.; Baetens, R.; Gustavsen, A. Aerogel Insulation for Building Applications. *Energy Build.* **2011**, No. 43, 761–769.

(19) Strubel, P.; Thieme, S.; Biemelt, T.; Helmer, A.; Oschatz, M.; Brinkner, J.; Althues, H.; Kaskel, S. ZnO Hard Templating for Synthesis of Hierarchical Porous Carbons with Tailored Porosity and High Performance in Lithium-Sulfur Battery. *Adv. Funct. Mater.*

2015, *25* (2), 287–297.

(20) Schlottig, F.; Textor, M.; Georgi, U.; Roewer, G. Template Synthesis of SiO_2 Nanostructures. *J. Mater. Sci.* **1999**, *8*, 599–601.

(21) Cai, Q.; Lin, W.-Y.; Xiao, F.-S.; Pang, W.-Q.; Chen, X.-H.; Zou, B.-S. The Preparation of Highly Ordered MCM-41 with Extremely Low Surfactant Concentration. *Microporous Mesoporous Mater.* **1999**, *32* (1–2), 1–15.

(22) Kresge, C. T.; Leonowicz, M. E.; Roth, W. J.; Vartuli, J. C.; Beck, J. S. Ordered Mesoporous Molecular Sieves Synthesized by a Liquid-Crystal Template Mechanism. *Nature* **1992**, *359* (6397), 710–712.

(23) Zhao, D.; Sun, J.; Li, Q.; Stucky, G. D. Morphological Control of Highly Ordered Mesoporous Silica SBA-15. *Chem. Mater.* **2000**, *12* (2), 275–279.

(24) Suzuki, K.; Ikari, K.; Imai, H. Synthesis of Silica Nanoparticles Having a Well-Ordered Mesostructure Using a Double Surfactant System. *J. Am. Chem. Soc.* **2004**, *126* (2), 462–463.

(25) Smarsly, B.; Grosso, D.; Brezesinski, T.; Pinna, N.; Boissière, C.; Antonietti, M.; Sanchez, C. Highly Crystalline Cubic Mesoporous TiO_2 with 10-Nm Pore Diameter Made with a New Block Copolymer Template. *Chem. Mater.* **2004**, *16* (15), 2948–2952.

(26) Rauda, I. E.; Buonsanti, R.; Saldarriaga-Lopez, L. C.; Benjauthrit, K.; Schelhas, L. T.; Stefik, M.; Augustyn, V.; Ko, J.; Dunn, B.; Wiesner, U.; et al. General Method for the Synthesis of Hierarchical Nanocrystal-Based Mesoporous Materials. *ACS Nano* **2012**, *6* (7), 6386–6399.

(27) Coquil, T.; Richman, E. K.; Hutchinson, N. J.; Tolbert, S. H.; Pilon, L. Thermal Conductivity of Cubic and Hexagonal Mesoporous Silica Thin Films. *J. Appl. Phys.* **2009**,

106 (3), 1–11.

(28) Hopkins, P. E.; Kaehr, B.; Phinney, L. M.; Koehler, T. P.; Grillet, A. M.; Dunphy, D.; Garcia, F.; Brinker, C. J. Measuring the Thermal Conductivity of Porous, Transparent SiO_2 Films With Time Domain Thermoreflectance. *J. Heat Transfer* **2011**, *133* (6), 61601.

(29) Smith, D. S.; Alzina, A.; Bourret, J.; Nait-Ali, B.; Pennec, F.; Tessier-Doyen, N.; Otsu, K.; Matsubara, H.; Elser, P.; Gonzenbach, U. T. Thermal Conductivity of Porous Materials. *J. Mater. Res.* **2013**, *28* (17), 2260–2272.

(30) Lee, J.; Lim, J.; Yang, P. Ballistic Phonon Transport in Holey Silicon. *Nano Lett.* **2015**, *15* (5), 3273–3279.

(31) Yang, L.; Yang, N.; Li, B. Extreme Low Thermal Conductivity in Nanoscale 3D Si Phononic Crystal with Spherical Pores. *Nano Lett.* **2014**, *14* (4), 1734–1738.

(32) Song, D.; Chen, G. Thermal Conductivity of Periodic Microporous Silicon Films. *Appl. Phys. Lett.* **2004**, *84* (5), 687–689.

(33) Tang, G. H.; Bi, C.; Zhao, Y.; Tao, W. Q. Thermal Transport in Nano-Porous Insulation of Aerogel: Factors, Models and Outlook. *Energy* **2015**, *90*, 701–721.

(34) Fang, J.; Reitz, C.; Brezesinski, T.; Nemanick, E. J.; Kang, C. B.; Tolbert, S. H.; Pilon, L. Thermal Conductivity of Highly-Ordered Mesoporous Titania Thin Films from 30 to 320 K. *J. Phys. Chem. C* **2011**, *115* (30), 14606–14614.

(35) Coquil, T.; Reitz, C. Thermal Conductivity of Ordered Mesoporous Titania Films Made from Nanocrystalline Building Blocks and Sol− Gel Reagents. *J. Phys. Chem. C* **2010**, No. 114, 12451–12458.

(36) Yang, L.; Zhang, Q.; Cui, Z.; Gerboth, M.; Zhao, Y.; Xu, T. T.; Walker, D. G.; Li, D. Ballistic Phonon Penetration Depth in Amorphous Silicon Dioxide. *Nano Lett.* **2017**, *17*

(12), 7218–7225.

(37) Larkin, J. M.; McGaughey, A. J. H. Thermal Conductivity Accumulation in Amorphous Silica and Amorphous Silicon. *Phys. Rev. B - Condens. Matter Mater. Phys.* **2014**, *89* (14), 1–12.

(38) Baklanov, M. R.; Mogilnikov, K. P.; Polovinkin, V. G.; Dultsev, F. N. Determination of Pore Size Distribution in Thin Films by Ellipsometric Porosimetry. *J. Vac. Sci. Technol. B Microelectron. Nanom. Struct. Process. Meas. Phenom.* **2000**, *18* (3), 1385–1391.

(39) R., H. S. J. Gregg, K. S. W. Sing: Adsorption, Surface Area and Porosity. 2. Auflage, Academic Press, London 1982. 303 Seiten, Preis: $ 49.50. *Berichte der Bunsengesellschaft für Phys. Chemie* **2018**, *86* (10), 957.

(40) Thommes, M.; Kaneko, K.; Neimark, A. V.; Olivier, J. P.; Rodriguez-Reinoso, F.; Rouquerol, J.; Sing, K. S. W. Physisorption of Gases, with Special Reference to the Evaluation of Surface Area and Pore Size Distribution (IUPAC Technical Report). *Pure Appl. Chem.* **2015**, *87* (9–10), 1051–1069.

(41) Kruk, M.; Jaroniec, M.; Ko, C. H.; Ryoo, R. Characterization of the Porous Structure of SBA-15. *Chem. Mater.* **2000**, *12* (7), 1961–1968.

(42) Ryoo, R.; Ko, C. H.; Kruk, M.; Antochshuk, V.; Jaroniec, M. Block-Copolymer-Templated Ordered Mesoporous Silica: Array of Uniform Mesopores or Mesopore−Micropore Network? *J. Phys. Chem. B* **2000**, *104* (48), 11465–11471.

(43) Tsui, B.; Yang, C. Anisotropic Thermal Conductivity of Nanoporous Silica Film. *Electron Devices, IEEE* **2004**, *51* (1), 20–27.

(44) Costescu, R. M.; Bullen, A. J.; Matamis, G.; O'Hara, K. E.; Cahill, D. G. Thermal Conductivity and Sound Velocities of Hydrogen-Silsesquioxane Low-K Dielectrics. *Phys.*

Rev. B - Condens. Matter Mater. Phys. **2002**, *65* (9), 942051–942056.

(45) Cahill, D. G. Thermal Conductivity Measurement from 30 to 750 K: The 3ω Method. *Rev. Sci. Instrum.* **1990**, *61* (2), 802–808.

(46) Fricke, J.; Lu, X.; Wang, P.; Büttner, D.; Heinemann, U. Optimization of Monolithic Silica Aerogel Insulants. *Int. J. Heat Mass Transf.* **1992**, *35* (9), 2305–2309.

(47) Pietrak, K.; Winiewski, T. S. A Review of Models for Effective Thermal Conductivity of Composite Materials. *Open Access J. J. Power Technol.* **2015**, *95* (1), 14–24.

(48) Russell, H. W. Principles of Heat Flow in Porous Insulators. *J. Am. Ceram. Soc.* **1935**, *18* (1-12), 1–5.

(49) Dunphy, D. R.; Sheth, P. H.; Garcia, F. L.; Brinker, C. J. Enlarged Pore Size in Mesoporous Silica Films Templated by Pluronic F127: Use of Poloxamer Mixtures and Increased template/SiO_2 Ratios in Materials Synthesized by Evaporation-Induced Self-Assembly. *Chem. Mater.* **2015**, *27* (1), 75–84.

(50) Ilavsky, J. Nika: Software for Two-Dimensional Data Reduction. *J. Appl. Crystallogr.* **2012**, *45* (2), 324–328.

(51) Cahill, D. G.; Goodson, K.; Majumdar, A. Thermometry and Thermal Transport in Micro/Nanoscale Solid-State Devices and Structures. *J. Heat Transfer* **2002**, *124* (2), 223.

(52) Cahill, D. G. Analysis of Heat Flow in Layered Structures for Time-Domain Thermoreflectance. *Rev. Sci. Instrum.* **2004**, *75* (12), 5119–5122.

(53) Li, M.; Kang, J. S.; Hu, Y. Anisotropic Thermal Conductivity Measurement Using a New Asymmetric-Beam Time-Domain Thermoreflectance (AB-TDTR) Method. *Rev. Sci. Instrum.* **2018**, *89* (8), 84901.

(54) Kang, J. S.; Wu, H.; Hu, Y. Thermal Properties and Phonon Spectral Characterization of

Synthetic Boron Phosphide for High Thermal Conductivity Applications. *Nano Lett.* **2017**, *17* (12), 7507–7514.

(55) Kang, J. S.; Ke, M.; Hu, Y. Ionic Intercalation in Two-Dimensional van Der Waals Materials: In Situ Characterization and Electrochemical Control of the Anisotropic Thermal Conductivity of Black Phosphorus. *Nano Lett.* **2017**, *17* (3), 1431–1438.

(56) Kang, J. S.; Li, M.; Wu, H.; Nguyen, H.; Hu, Y. Experimental Observation of High Thermal Conductivity in Boron Arsenide. *Science (80-.).* **2018**, eaat5522.

(57) Marszewski, M.; Butts, D.; Lan, E.; Yan, Y.; King, S. C.; McNeil, P. E.; Galy, T.; Dunn, B.; Tolbert, S. H.; Hu, Y.; et al. Effect of Surface Hydroxyl Groups on Heat Capacity of Mesoporous Silica. *Appl. Phys. Lett.* **2018**, *112* (20).

CHAPTER 7

Effect of Pore Size on Thermal Conductivity in Nanoparticle and Sol-gel Based mesoporous SiO_2 Films

7.1 Introduction

Thermal transport at nanoscale has been an area of intense research due to various applications of nanostructured materials including thermoelectrics,[1,2] thermally insulating materials,[3,4] and thermal interface materials.[5] Nanostructuring offers unprecedented capabilities of controlling thermal transport through tuning various structural parameters.[6] Therefore, gaining insight in the thermal transport at nanoscale is essential to design nanomaterials and nanocomposites. Many structural factors such as size, porosity, surface, interface, defect, and impurity[7–10] could have major influence on thermal conductivity in nanoscale materials. Particularly, porous structures have strong tunable size effects due to increased surface area.[11] Although the size effect in crystalline materials is quite well understood,[12,13] the size effect on the thermal conductivity of amorphous materials remains underdeveloped.

Porous amorphous SiO_2 has received significant attention due to the strong phonon boundary scattering effects resulting in significant reduction in thermal conductivity.[11,14–16] For instance, aerogels, composed of chains of amorphous silica (a-SiO_2) nanoparticles, featured extremely low thermal conductivities (0.013 W/m K) and have been used as thermal insulation in a variety of applications.[17–23] Several studies[16,24] have observed that the thermal conductivity of nonporous a-SiO_2 thin films (100-900 nm) was independent on film thickness, suggesting that any propagating modes contributing to thermal conductivity have mean-free paths (MFPs) below 100 nm.[22] In

addition, the effective thermal conductivity of mesoporous a-SiO_2 at room temperature has been shown to decreases rapidly with increasing porosity.[15,26,27] Hu *et al.*[28] proposed phenomenological ad hoc two-phase mixture models that describe the dependence of the conductivity on porosity.

However, the correlation between pore size in porous SiO_2 and thermal conductivity remains unclear. In theory, the strongest scattering would come from the smallest pores and the maximum phonon mean free path would be limited to the largest pore size.[29] Some experimental studies have suggested that the thermal conductivity of mesoporous SiO_2 (mp-SiO_2) was independent of pore size.[26,30] However, they only focused on SiO_2 aerogel or sol-gel network and sampled a limited range of pore size. Jain *et al.* showed that the thermal conductivity of xerogel films depended on the pore size distribution, with micropores in the sample with broader size distribution dominating phonon scattering.[29] However, due to the different preparation processes, these samples may have different amount of cracks, defects, and impurities that also contribute to phonon scattering, making the comparison not rigorously valid. In our previous work,[31] the effective thermal conductivity of sol-gel films featured slight dependence on pore size but it was independent of pore size in nanoparticle-based films. However, the pore size of the different films differed only by a few nanometers. Modeling studies of thermal transport also rarely consider pore size effect on its own. Pore size is typically either combined with porosity and other structural parameters as one fitting parameter in numerical models[32–34] or considered as a factor for gaseous thermal conductivity[27,35] or solid-gas coupled thermal conductivity.[36] Thus, the investigation should be extended to a broader pore size range to gain better insight into the effect of pore size on thermal conductivity of mesoporous SiO_2.

The present study discusses the effect of pore size on the effective thermal conductivity of mp-SiO_2 films considering a wide range of pore sizes and two different SiO_2 frameworks, i.e., a

continuous sol-gel matrix or discontinuous nanoparticle network. A number of sol-gel (SG) and nanoparticle (NP)-based mp-SiO_2 thin films with different pore sizes were synthesized under the same conditions to reduce the effect of impurities and defects. The effective thermal conductivity was measured with time domain thermoreflectance (TDTR) in vacuum at room temperature to eliminate the contribution of the gas phase to thermal transport. Physical explanations were provided to elucidate the effect of pore size and framework on thermal conductivity.

7.2 Results and Discussion

Nanoparticle-based Mesoporous SiO_2 films

To thoroughly examine the pore size effect on thermal conductivity, PMMA colloids with particle diameter ranging from 10-70 nm were used as the polymer template. Figure 7.1 shows SEM images of porous SiO_2 films templated with different sizes of PMMA. Although all films had a wide pore size distribution due to the polydispersity of the PMMA colloids, the pore size distribution corresponded to that of the PMMA templates. Additionally, the walls separating the pores made from larger PMMA colloids were composed of more nanoparticles than those made from smaller PMMA colloids.

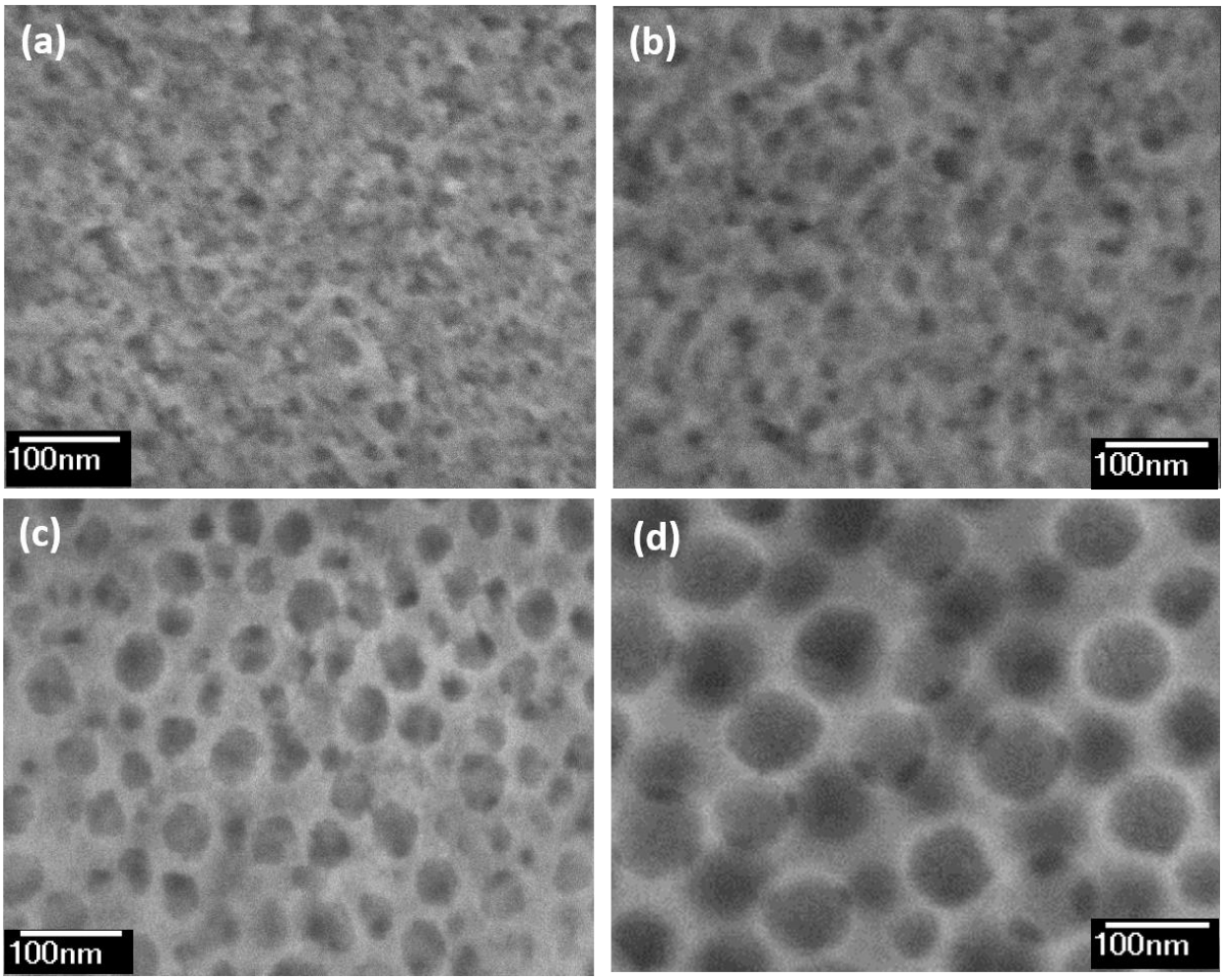

Figure 7.1. SEM images of mp-SiO_2 films templated with PMMA of different sizes at ratio m_{poly}/m_{SiO2} = 1.5 (g/g). (a) average 10 nm, (b) average 20 nm, (c) average 35 nm and (d) average 70 nm. The wall thickness increased with the increasing size of PMMA colloids used as the template.

The porosity and pore size were analyzed by ellipsometric porosimetry using toluene as an adsorbate[37] for F127-templated NP-based mp-SiO_2 films. The large pore size and the wide pore size distribution in PMMA-templated SiO_2 films were beyond the measurable range for the optical reflection based ellipsometry method, so N_2 adsorption porosimetry was conducted on the PMMA-templated mp-SiO_2 powders prepared in the same manner as their corresponding films. Figure 7.2 shows adsorption/desorption isotherms and pore size distributions for representative F127 and PMMA-templated NP-based mp-SiO_2 films. Both isotherms were of type IV with H2(b) hysteresis

loop according to the IUPAC classification,[38,39] which indicated the presence of mesopores with narrow necks connecting the pores. The slope of the adsorption isotherm as a function of relative pressure was much steeper in the F127-templated sample (Figure 7.2a) than in the PMMA-templated one (Figure 7.2b), suggesting a narrower pore size distribution.[40] The difference in the degree of polydispersity was also observed in the pore size distribution (Figures 7.2c and 7.2d). In fact, the PMMA-templated films had bimodal pores size distribution, indicated by the two different hysteresis regions at $P/P_0 = 0.45 – 0.75$ and $P/P_0 = 0.9 – 1$ (Figure 7.2b). The small pores correspond to the intrinsic gaps between the SiO_2 nanoparticles and range from 4 – 6 nm in diameter. The large pores corresponded to the voids left after removing the PMMA template and their size, 15 – 68 nm, depending on the size of the PMMA colloid used. In contrast, the pore size distribution of NP-based mp-SiO_2 films templated with Pluronic F127 showed only one peak. This can be attributed to the fact that the size distributions of the interparticle porosity and of the template-derived porosity were similar and overlapped.

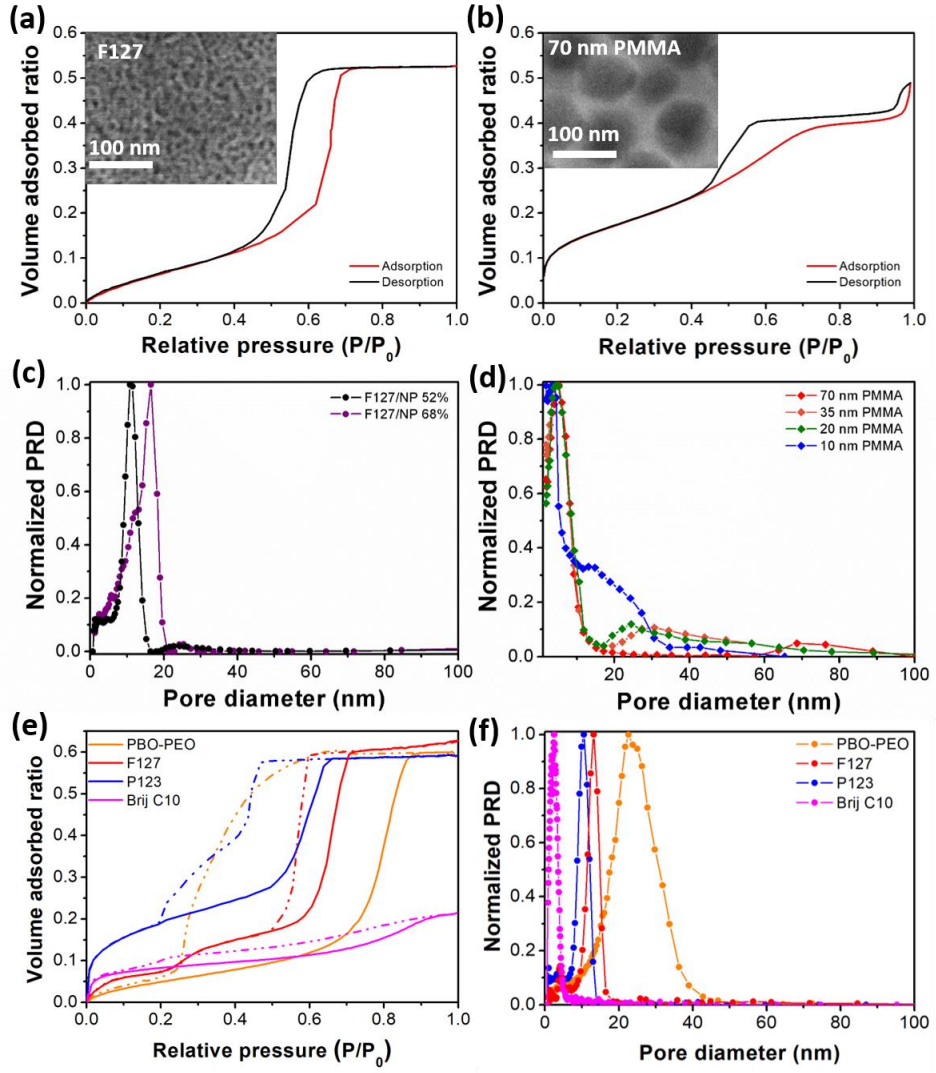

Figure 7.2. Isotherms and pore size distribution of NP-based and SG-based mp-SiO_2 films templated with various polymers and surfactants. (a) toluene adsorption/desorption isotherms for F127-templated NP-based mp-SiO_2 film at porosity of 52.5%, (b) nitrogen adsorption/desorption isotherms for 70 nm PMMA-templated NP-based mp-SiO_2 film at porosity of 49%, (c) pore size distribution for F127-templated NP-based mp-SiO_2 films, (d) pore size distrubiton for NP-based mp-SiO_2 films with different PMMA templates, (e) representative toluene adsorption/desorption isotherms for SG-based mp-SiO_2 films with different templates, (f) representative pore size distribution for SG-based mp-SiO_2 films with different templates. Insets in (a) and (b) are representative SEM images of NP-based mp-SiO_2 films templated with F127 and 70 nm PMMA, respectively. The pore diameter from porosimetry matched the observation from SEM images.

Table 7.1 summarizes the characterization of two groups of NP-based mp-SiO_2 films with similar porosity but different pore diameter. The two average pore diameter values for PMMA templated films correspond to the intrinsic gaps between the SiO_2 nanoparticles and the voids left after

removing the PMMA template respectively. The first group had porosity of 65–71% and pore diameter of 15–28 nm while the second group had porosity of 49–53% and pore diameter of 10–68 nm. The wall sizes were estimated from SEM graphs. Table 1 indicates that NP-based mp-SiO_2 films with similar porosity had similar effective thermal conductivity despite having very different average pore size. We hypothesize that this observation was due to the fact that the thermal transport in NP-based films was determined by the inter-particle phonon scattering that depends on the nanoparticle size rather than on the pore size.

Table 7.1. Structural Characterization and Thermal Conductivity of F127 and PMMA-templated NP-Based mp-SiO_2 Films

Template	Porosity (%)	Average Pore diameter (nm)	Wall thickness (nm)	Thermal conductivity (W/mK, vac)
10 nm PMMA	65	4/15	5-10	0.10±0.01
F127	68	16.5	4-6	0.10±0.01
35 nm PMMA	71	6/28	8-30	0.09±0.01
F127	52.5	10.8	4-6	0.19±0.02
10 nm PMMA	49	4/15	5-10	0.23±0.02
20 nm PMMA	50	5/24	5-15	0.21±0.02
70 nm PMMA	49	5/68	10-55	0.19±0.01

Sol-gel based mesoporous SiO_2 films

The PMMA colloids were incompatible with the solvents needed for the SG-based mp-SiO_2 film synthesis since they tend to aggregate in ethanol. Thus, instead of the PMMA colloids, a variety of ethanol stable templates were used to make SG-based films with different pore sizes. Figure 7.3 shows typical SEM images of SG-based mp-SiO_2 films synthesized with these different templates. Those templated with CTAB and Brij®C10 had very small pores - between 1 and 4 nm in diameter - as shown in the SEM images (Figure 7.3a). On the other hand, the films templated with block copolymers PBO-PEO had large pores with diameter between 15 and 25 nm (Figure 7.3d). Block

copolymer-templated samples display fairly ordered porous structure, as shown in Figures 7.3b–7.3d as well as in two-dimensional grazing incidence-small angle X-ray scattering (2D-GISAXS) data in Figure 7.4. The diffraction arc along the q_x and q_y directions indicate that the films had ordered porosity both in the plane of the substrate and in that perpendicular to it. The integrated spectra along the q_x-direction was obtained from the 2D-GISAXS pattern (Figure 7.4c). The interplane spacing d between repeating unit cells of mesopores, calculated as $d = 2\pi/q$, increased as the template size increased.

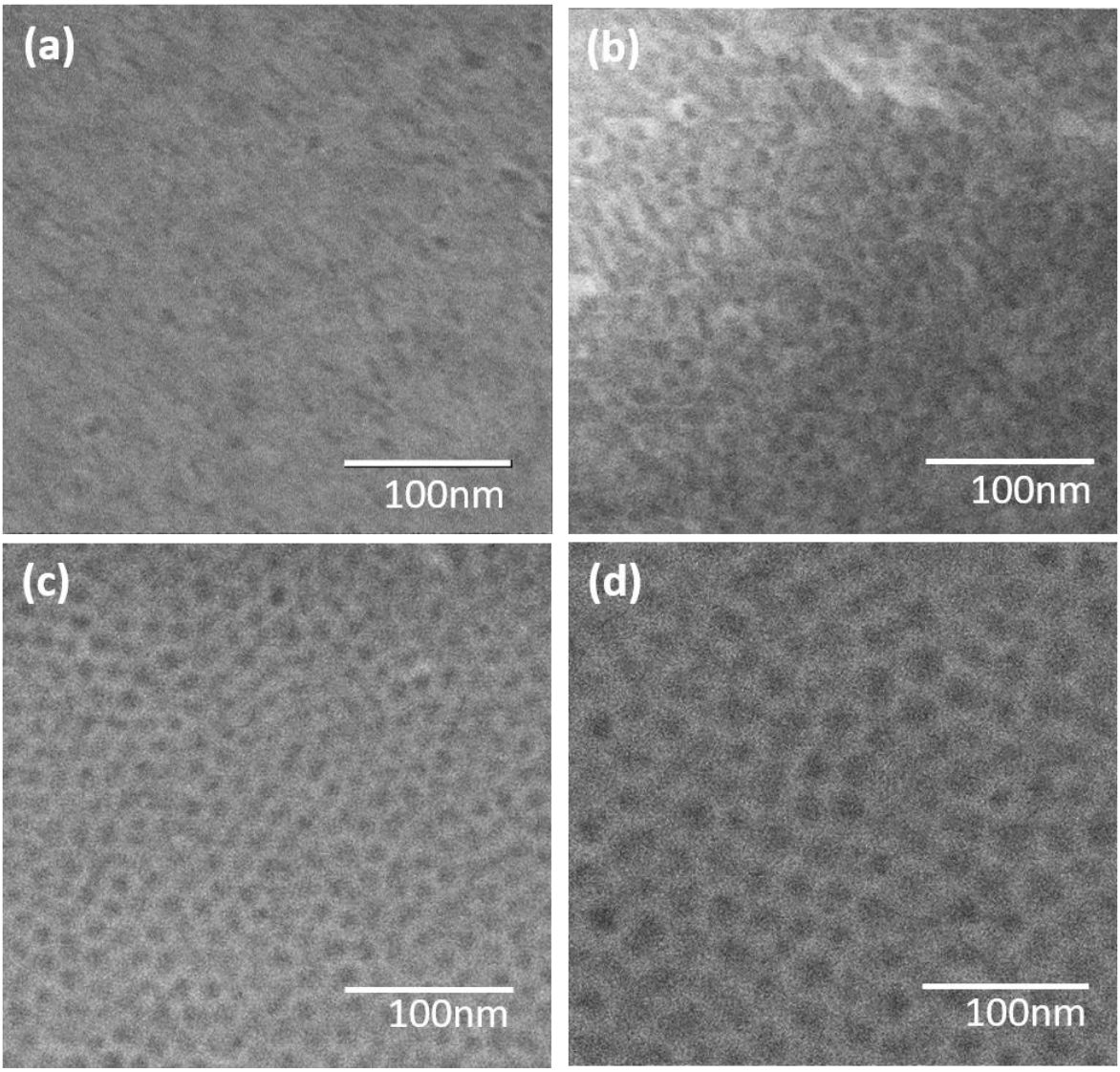

Figure 7.3. SEM images of SG-based mp-SiO_2 films templated by (a) Brij®C10, (b) Pluronic P123, (c) Pluronic F127, and (d) PBO-PEO at m_{poly}/m_{SiO2} = 1.5 (g/g). Films had increasing

The porosity and pore size of SG-based mp-SiO_2 films were measured by ellipsometric porosimetry, as previously described. Figures 7.2e–7.2f show toluene adsorption/desorption isotherms and pore size distributions for representative SG-based mp-SiO_2 films templated with Brij®C10, Pluronic P123, Pluronic F127, and PBO-PEO. Here also, the hysteresis loops in the isotherms indicated the presence of mesopores connected by narrow necks. Most of samples had a fair narrow pore size distribution. The pore sizes from porosimetry measurement were in

agreement with estimates from SEM. The wall size *w* of SG-based mp-SiO_2 films were calculated by combining pore radius *r* from ellipsometric porosimetry with interplane spacing *d* from 2D-GISAXS according to[41]

$$w = 2 \times (\frac{d}{\sqrt{3}} - r) \qquad (1)$$

In general, samples made with larger templates also displays thicker walls. For samples that lack periodicity (at low m_{poly}/m_{SiO2} ratio or templated by CTAB and Brij®C10), a range of wall thickness was measured and estimated from SEM images.

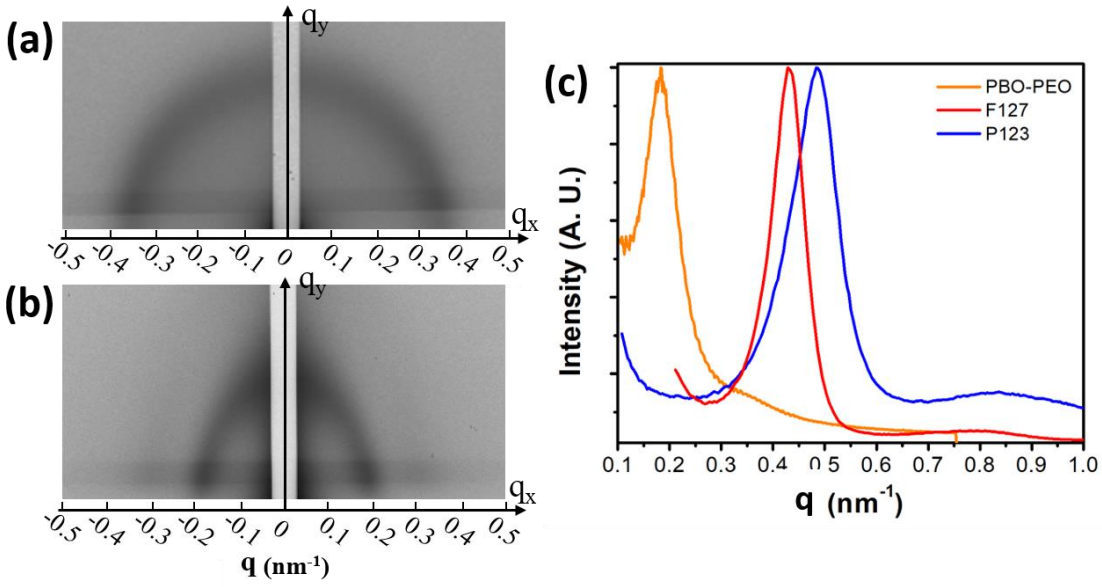

Figure 7.4. Small angle X-ray scattering of SG-based mp-SiO_2 films. (a) and (b) representative 2D-GISAXS patterns of SG-based mp-SiO_2 films template by (a) F127 and (b) PBO-PEO. (c) Integrated intensity spectra converted from a 2D-GISAXS pattern along the q_x direction corresponding to in-plane scattering for PBO-PEO, F127 and P123 templated SG-

. The first group had porosity of 59–62% and pore diameter ranging from 10 to 23 nm, the second group had porosity of 43–45% and pore diameter ranging from 5 to 15 nm, while the third group had porosity of 18–22% and pore diameter ranging from 2 to 4 nm. Table 2 indicates that SG-based mp-SiO_2 films with similar porosity but larger pore size had larger effective thermal conductivity. For a

given porosity, the SG-based mp-SiO_2 films templated with CTAB and Brij®C10 had lower thermal conductivity than films templated with Pluronic P123 templates, followed by films templated with Pluronic F127 and then PBO-PEO. This order correlated with the pore size created by these templates in SG-based mp-SiO_2 films. We hypothesize that the films with bigger pores also had thicker pore walls that provided larger heat conduction path, thus increasing the effective thermal conductivity.

Table 7.2. Structural Characterization and Thermal Conductivity of SG-based mp-SiO_2 Films Synthesized with Different Templates

Template	Porosity (%)	Pore diameter (nm)	Pore-wall repeating distance (nm)	Wall thickness (nm)*	Thermal conductivity (W/mK, vacuum)
P123	59	10.7	13	4	0.08 ± 0.02
F127	62	13.6	15	4	0.09 ± 0.02
PBO-PEO	60	22.5	32.5	15	0.18 ± 0.03
P123	45	5.9	11.2	7	0.19 ± 0.01
F127	44	7.5	13.6	8	0.22 ± 0.02
PBO-PEO	43	15	22.8	11	0.27 ± 0.04
CTAB	22	2	N/A	2-3	0.28 ± 0.02
BrijC10	21	2.2	N/A	2-3	0.27 ± 0.05
P123	18	2.8	N/A	3-5	0.37 ± 0.05
F127	20	3.5	N/A	3-6	0.39 ± 0.05

*Wall thickness calculated from GISAXS and porosimetry data. For samples without GISAXS data, a range was estimated from SEM images.

Porosity weighted simple medium (PWSM) model has been proposed to account for the porous structural parameters by using a fitting parameter *x*.[26,42] Considering the disperse phase in the pores to be vacuum, the PWSM simplifies to[26]

$$\text{PWSM model} \quad \kappa_{eff} = \kappa_{SiO_2}(1-\phi_p)(1-{\phi_p}^{x}) \tag{1}$$

Fitting the PWSM model to our experimental data yielded *x* = 0.17, 0.27 and 0.47 for small (CTAB and Brij C10), medium (P123 and F127), and large (PBO-PEO) pore sizes, respectively. Figure 4 plots the thermal conductivity measured for all SG-based mp-SiO_2 films studied along with PWSM model fitting to guide the eye. Since the wall thickness increases with increasing pore size, the necks

connecting the pores have larger cross-section and offer less thermal resistance to heat conduction. Therefore, for a given porosity, the thermal conductivity of SG-based mp-SiO_2 films increased with pore size and wall thickness.

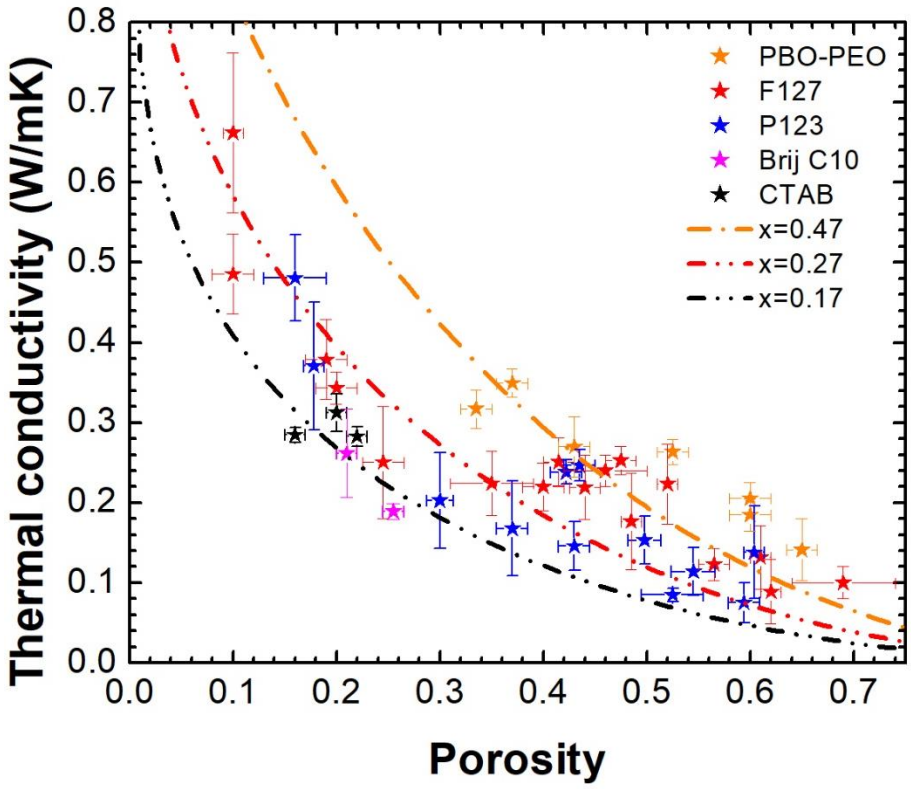

Figure 7.5. Thermal conductivity as a function of porosity for SG-based mp-SiO_2 films with different templates measured under vacuum with PWSM fitting.

Overall, the different dependence of thermal conductivity on pore size in SG-based and NP-based mp-SiO_2 films arises from differences in the framework nanoscale architecture. As revealed by transmission electron microscopy (TEM) images in Figure 7.6, the NP-based film was composed of individual, discontinuous, overlapping nanoparticles. The smallest gap for phonon scattering was the intrinsic gap between individual particles. On the other hand, the sol-gel network was composed of homogeneous, ordered pores with continuous solid network surrounding them.

The limit for phonon mean free path is associated with the wall thickness, which is affected not only by the porosity but also by the pore size.

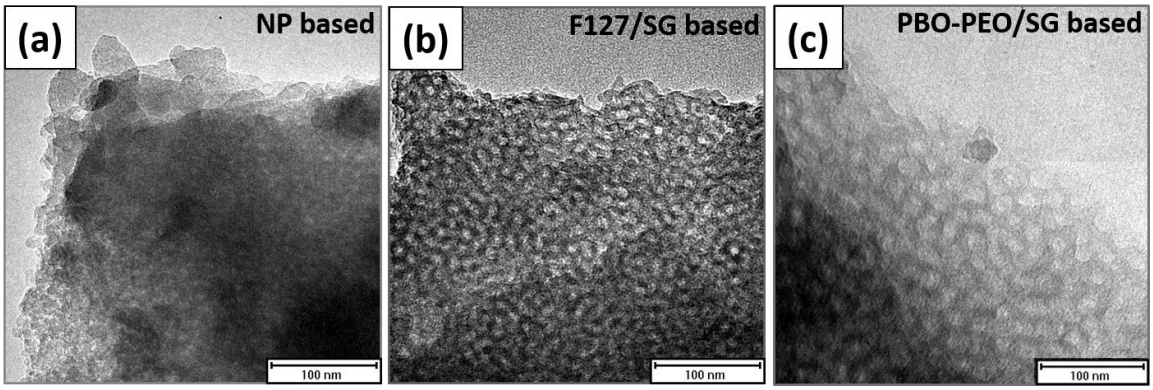

Figure 7.6. Transmission electron microscopy (TEM) images of (a) F127 templated NP-based mp-SiO_2 films (b) F127 templated SG-based mp-SiO_2 films and (c) PBO-PEO templated SG-based mp-SiO_2 films. The images clearly show that the sol-gel network was more ordered and continuous, while the nanoparticle-based films were composed of discontinuous, individual nanoparticles.

7.3 Conclusions

In conclusion, this letter presented synthesis, characterization, and cross-plane thermal conductivity measurements at room temperature under vacuum of sol-gel and nanoparticle-based mesoporous amorphous silica thin films. The effect of pore size and framework on thermal conductivity were investigated and found to be dependent on the nanoscale framework, i.e., continuous vs. aggregated nanoparticles. In continuous sol-gel network, the thermal conductivity decreased with decreasing pore size for a given porosity. This was attributed to the fact that the characteristic length for heat carrier scattering was the wall thickness, which was dependent on the pore size and porosity. On the other hand, for discontinuous nanoparticle-based framework, the thermal conductivity was independent of pore size. In this case, the heat carrier characteristic length was the size of individual pre-formed nanoparticles, and therefore was independent of pore size. This work sheds new light on the effect of pore size on thermal transport in amorphous mesoporous

materials. It can be used to tune their nanoscale architecture to achieve the desired thermal conductivity.

7.4 Experimental Methods

7.4.1. Materials

The following materials were obtained from commercial suppliers and used without further purification: colloidal suspension of SiO_2 nanoparticles (15 wt%, Nalco 2326, ammonia-stabilized colloidal silica, d = 5 nm, Nalco Chemical Company), triblock copolymer Pluronic P123 ($EO_{20}PO_{70}EO_{20}$, M_w = 5800 Da, BASF), triblock copolymer Pluronic F127 ($EO_{100}PO_{65}EO_{100}$, M_w = 12600 Da, BASF), hexadecyltrimethylammonium bromide (CTAB, M_w=364.5 g/mol, Sigma-Aldrich), Brij®C10 ($C_{16}H_{33}(OCH_2CH_2)_nOH$, n~10, M_w=683 g/mol, Sigma-Aldrich), poly-(ethylene oxide-b-butylene oxide) (PBO-PEO, M_n=11000 g/mol, EO/BO = 6:5, PDI = 1.1, Advanced Polymer Inc), tetraethyl orthosilicate (98%, Acros Organics), hydrochloric acid (Certified ACS Plus, Fisher Scientific), ethanol (200 proof, Rossville Gold Shield), Ammonium persulfate (98%, Alfa Aesar), ammonium lauryl sulfate (~30% in H_2O, Sigma Aldrich), methyl methacrylate (contains ≤30 ppm MEHQ as inhibitor, 99%, Sigma Aldrich).

7.4.2. Synthesis

Synthesis of poly(methyl methacrylate) (PMMA) colloidal templates

The method is adapted from previous literature.[42,43] Ammonium persulfate (APS) was used as the initiator and ammonium lauryl sulfate (ALS) as the surfactant. APS, ALS and deionized water were put into a three-neck round-bottom flask (250 mL) equipped with magnetic stirrer, reflux condenser and thermometer. After the temperature was raised to 75 ˚C, the monomer methyl methacrylate was added in a differential manner (continuous addition in very small drops) using a syringe pump for about 1 h. Afterwards, the reaction temperature was kept at 80–85 ˚C for an

additional hour before a cooling operation was applied. The concentration of reagents is varied to make different sizes of PMMA. For the 70 nm PMMA, syringe pump is not used. Table 7.3 gives the detailed synthesis condition.

Table 7.3. synthesis condition for PMMA colloids of different sizes

Average PMMA colloid size	APS	ALS	MMA	Water
10 nm	0.08 g	7 mL	14 mL	84 mL
20 nm	0.08 g	2.29 mL	14 mL	84 mL
35 nm	0.08 g	2.29 mL	14 mL	22.5 mL
70 nm	0.08 g	0.61 mL	12.56 mL	165 mL

Synthesis of nanoparticle-based mesoporous SiO_2 films

First, a stock solution of polymer was made by dissolving 0.678 g of Pluronic F127 in 3 mL deionized water. In the case of films templated with PMMA, the as-synthesized colloidal solutions were used without further purification. The stock polymer solution was mixed with the colloidal suspension of SiO_2 nanoparticles to produce a solution with polymer-to-SiO_2 mass ratio between 1 and 1.5 g/g. Then, 80 μL of the polymer-silica solution was spin-coated onto 1" × 1" Si substrates. The film's thickness was adjusted by controlling the spin speed. The dried films were calcined in air at 350 ℃ for 30 min using 2 °C/min temperature ramp to remove the polymer. Nanoparticle-based SiO_2 powder was also synthesized from the same solutions for heat capacity measurements. Instead of spin-coating, the solutions were evaporated in a Petri dish at ambient condition for a day and collected in powdered form after calcination at 350 ℃ for 3 hour in oxygen.

Synthesis of sol-gel based mesoporous SiO_2 films

The sol-gel synthesis was adapted from previous literature.[44] First, 25 mg of the desired surfactant was dissolved in 0.6 mL of ethanol and 0.16 mL of 0.05 M HCl. A certain amount of tetraethyl orthosilicate (TEOS) was added to the mixture to achieve a polymer-to-SiO_2 mass ratio between 0.3 and 2 g/g. Then, 80 μL of the polymer-silica solution was spin-coated onto 1" × 1" Si substrates. The film's thickness was adjusted by controlling the spin speed. The dried films were calcined in air at 350 ℃ for 30 min using 2 ℃/min temperature ramp to remove the polymer.

7.4.3. Structural characterization

Scanning Electron Microscopy (SEM) images were obtained using a model JEOL JSM-6700F field emission electron microscope with 5 kV accelerating voltage and secondary electron detector configuration. Transmission Electron Microscopy (TEM) images were obtained using a Technai G^2 TF20 High-Resolution EM, CryoEM and CryoET (FEI) at an accelerating voltage 200 kV and a TIETZ F415MP 16 megapixel 4k×4k CCD detector. Two-dimensional grazing incidence small-angle x-ray scattering (2D-GISAXS) data were collected at the Stanford Synchrotron Lightsource (SSRL) using beamlines 1-5 with a wavelength of 0.1033 nm operated at an X-Ray energy of 12.002 keV and detector distance of 2.870 m using a Rayonix-165 CCD detector. The data was then calibrated and reduced using the Nika package from Igor Pro.[45] Ellipsometric porosimetry was performed on a PS-1100 instrument from Semilab using toluene as the adsorbate to quantify porosity and pore size. The instrument used a UV-visible CCD detector adapted to a grating spectrograph to analyze the signal reflected by the sample. The light source was a 75 W Hamamatsu Xenon lamp and the measurements were performed in the spectral range from 1.25–4.5 eV. Data analysis was performed using the associated Spectroscopic Ellipsometry Analyzer software with the assumption of cylindrical pores. An optical reflectance-based method was also used to verify porosity. The experimental spectral normal-hemispherical reflectance $R_{exp,\lambda}$ was

measured with a Shimadzu UV3101 PC UV-VIS spectrophotometer, equipped with a Shimadzu ISR3000 integrating sphere. The reference intensity was measured using a high specular reflection standard mirror by Ocean Optics (NIST certified STAN-SSH). The reflectance was measured in the visible range between 400 nm to 800 nm every nm. Nitrogen porosimetry was carried out using a Micromeritics TriStar II 3020 porosimeter. The surface area was then deduced from the adsorption branch of the isotherm at low relative pressures using the Brunauer-Emmett-Teller (BET) model. The pore diameter and pore volume were also derived from the adsorption branch of the isotherm using the Barret-Joyner-Halenda (BJH) model.

7.4.4. Thermal conductivity measurements

The thermal conductivity measurements on mesoporous SiO_2 films were performed using time-domain thermoreflectance (TDTR) method. The detailed working principles and experimental setup can be found somewhere else.[46–49] Briefly speaking, a thin aluminum film (80 nm) was deposited by e-beam evaporation on the top surface of the samples, serving as both transducer to convert laser energy to thermal energy and temperature sensor. The absorbed energy from pump beam with wavelength of 400 nm led to an instantaneous temperature rise. The probe beam with wavelength of 800 nm was used to continuously detect temperature decay by measuring the reflection portion using a photo diode. The delay time between pump pulse and probe pulse can be controlled with temporal resolution higher than sub-picosecond. Next, the full transient decay curve from -100 ps to 5000 ps was fitted with thermal diffusion model to obtain the thermal conductivity k of the sample. To avoid the difference of local thermal conductivity induced by random network of SiO_2, big laser spot size with diameter of 20 μm was used to average the structure effects during measurement. To ensure the uniformity of the sample as well as the reliability of the thermal conductivity data, measurements were repeated at ten different locations

on a 1 cm x 1 cm area of the sample. Samples were dehydrated by heating on a hot plate at 150 ^{o}C for more than 12 hours. The dehydrated samples were measured in a vacuum chamber with pressure less than 1 Pa at room temperature.

7.5 References

(1) Boukai, A. I.; Bunimovich, Y.; Tahir-Kheli, J.; Yu, J.-K.; Goddard Iii, W. A.; Heath, J. R. Silicon Nanowires as Efficient Thermoelectric Materials. In *Materials For Sustainable Energy: A Collection of Peer-Reviewed Research and Review Articles from Nature Publishing Group*; World Scientific, 2011; pp 116–119.

(2) Dresselhaus, M. S.; Chen, G.; Tang, M. Y.; Yang, R. G.; Lee, H.; Wang, D. Z.; Ren, Z. F.; Fleurial, J.; Gogna, P. New Directions for Low-dimensional Thermoelectric Materials. *Adv. Mater.* **2007**, *19* (8), 1043–1053.

(3) Costescu, R. M.; Cahill, D. G.; Fabreguette, F. H.; Sechrist, Z. A.; George, S. M. Ultra-Low Thermal Conductivity in W/Al_2O_3 Nanolaminates. *Science (80-.).* **2004**, *303* (5660), 989–990.

(4) Hrubesh, L. W.; Pekala, R. W. Thermal Properties of Organic and Inorganic Aerogels. *J. Mater. Res.* **1994**, *9* (3), 731–738.

(5) Prasher, R. Thermal Interface Materials: Historical Perspective, Status, and Future Directions. *Proc. IEEE* **2006**, *94* (8), 1571–1586.

(6) Cahill, D. G.; Ford, W. K.; Goodson, K. E.; Mahan, G. D.; Majumdar, A.; Maris, H. J.; Merlin, R.; Phillpot, S. R. Nanoscale Thermal Transport. *J. Appl. Phys.* **2003**, *93* (2), 793–818.

(7) Sansoz, F. Surface Faceting Dependence of Thermal Transport in Silicon Nanowires. *Nano Lett.* **2011**, *11* (12), 5378–5382.

(8) Gu, H.; Wang, H. Effect of Strain on Thermal Conductivity of Amorphous Silicon Dioxide Thin Films: A Molecular Dynamics Study. *Comput. Mater. Sci.* **2018**, *144*, 133–138.

(9) Alam, M. T.; Raghu, A. P.; Haque, M. A.; Muratore, C.; Voevodin, A. A. Structural Size and Temperature Dependence of Solid to Air Heat Transfer. *Int. J. Therm. Sci.* **2013**, *73*, 1–7.

(10) Tian, Z.; Hu, H.; Sun, Y. A Molecular Dynamics Study of Effective Thermal Conductivity in Nanocomposites. *Int. J. Heat Mass Transf.* **2013**, *61* (1), 577–582.

(11) Hopkins, P. E.; Rakich, P. T.; Olsson, R. H.; El-Kady, I. F.; Phinney, L. M. Origin of Reduction in Phonon Thermal Conductivity of Microporous Solids. *Appl. Phys. Lett.* **2009**, *95* (16), 2007–2010.

(12) Marconnet, A. M.; Asheghi, M.; Goodson, K. E. From the Casimir Limit to Phononic Crystals: 20 Years of Phonon Transport Studies Using Silicon-on-Insulator Technology. *J. Heat Transfer* **2013**, *135* (6), 61601.

(13) Zhang, H.; Hua, C.; Ding, D.; Minnich, A. J. Length Dependent Thermal Conductivity Measurements Yield Phonon Mean Free Path Spectra in Nanostructures. *Sci. Rep.* **2015**, *5*, 9121.

(14) Deng, Z.; Wang, J.; Wu, A.; Shen, J.; Zhou, B. High Strength SiO2 Aerogel insulation1. *J. Non. Cryst. Solids* **1998**, *225*, 101–104.

(15) Hopkins, P. E.; Kaehr, B.; Phinney, L. M.; Koehler, T. P.; Grillet, A. M.; Dunphy, D.; Garcia, F.; Brinker, C. J. Measuring the Thermal Conductivity of Porous, Transparent SiO_2 Films With Time Domain Thermoreflectance. *J. Heat Transfer* **2011**, *133* (6), 61601.

(16) Larkin, J. M.; McGaughey, A. J. H. Thermal Conductivity Accumulation in Amorphous Silica and Amorphous Silicon. *Phys. Rev. B - Condens. Matter Mater. Phys.* **2014**, *89* (14),

1–12.

(17) Schmidt, M.; Schwertfeger, F. Applications for Silica Aerogel Products. *J. Non. Cryst. Solids* **1998**, *225*, 364–368.

(18) Reim, M.; Reichenauer, G.; Körner, W.; Manara, J.; Arduini-Schuster, M.; Korder, S.; Beck, A.; Fricke, J. Silica-Aerogel granulate–Structural, Optical and Thermal Properties. *J. Non. Cryst. Solids* **2004**, *350*, 358–363.

(19) Reim, M.; Körner, W.; Manara, J.; Korder, S.; Arduini-Schuster, M.; Ebert, H.-P.; Fricke, J. Silica Aerogel Granulate Material for Thermal Insulation and Daylighting. *Sol. Energy* **2005**, *79* (2), 131–139.

(20) Baetens, R.; Jelle, B. P.; Gustavsen, A. Aerogel Insulation for Building Applications: A State-of-the-Art Review. *Energy Build.* **2011**, *43* (4), 761–769.

(21) Chen, K.; Neugebauer, A.; Goutierre, T.; Tang, A.; Glicksman, L.; Gibson, L. J. Mechanical and Thermal Performance of Aerogel-Filled Sandwich Panels for Building Insulation. *Energy Build.* **2014**, *76*, 336–346.

(22) Venkateswara Rao, A.; Pajonk, G. M.; Haranath, D. Synthesis of Hydrophobic Aerogels for Transparent Window Insulation Applications. *Mater. Sci. Technol.* **2001**, *17* (3), 343–348.

(23) Wei, T.; Chang, T.; Lu, S.; Chang, Y. Preparation of Monolithic Silica Aerogel of Low Thermal Conductivity by Ambient Pressure Drying. *J. Am. Ceram. Soc.* **2007**, *90* (7), 2003–2007.

(24) Shenogin, S.; Bodapati, A.; Keblinski, P.; McGaughey, A. J. H. Predicting the Thermal Conductivity of Inorganic and Polymeric Glasses: The Role of Anharmonicity. *J. Appl. Phys.* **2009**, *105* (3).

(25) Regner, K. T.; Sellan, D. P.; Su, Z.; Amon, C. H.; McGaughey, A. J. H.; Malen, J. A.

Broadband Phonon Mean Free Path Contributions to Thermal Conductivity Measured Using Frequency Domain Thermoreflectance. *Nat. Commun.* **2013**, *4*, 1640–1647.

(26) Coquil, T.; Richman, E. K.; Hutchinson, N. J.; Tolbert, S. H.; Pilon, L. Thermal Conductivity of Cubic and Hexagonal Mesoporous Silica Thin Films. *J. Appl. Phys.* **2009**, *106* (3), 1–11.

(27) Lu, X.; Caps, R.; Fricke, J.; Alviso, C. T.; Pekala, R. W. Correlation between Structure and Thermal Conductivity of Organic Aerogels. *J. Non. Cryst. Solids* **1995**, *188* (3), 226–234.

(28) Hu, C.; Morgen, M.; Ho, P. S.; Jain, A.; Gill, W. N.; Plawsky, J. L.; Wayner, P. C. Thermal Conductivity Study of Porous Low- *K* Dielectric Materials. *Appl. Phys. Lett.* **2000**, *77* (1), 145–147.

(29) Jain, A.; Rogojevic, S.; Ponoth, S.; Gill, W. N.; Plawsky, J. L.; Simonyi, E.; Chen, S.-T.; Ho, P. S. Processing Dependent Thermal Conductivity of Nanoporous Silica Xerogel Films. *J. Appl. Phys.* **2002**, *91* (5), 3275–3281.

(30) Liu, J.; Gan, D.; Hu, C.; Kiene, M.; Ho, P. S.; Volksen, W.; Miller, R. D. Porosity Effect on the Dielectric Constant and Thermomechanical Properties of Organosilicate Films. *Appl. Phys. Lett.* **2002**, *81* (22), 4180–4182.

(31) Yan, Y.; Li, M.; King, S.; Galy, T.; Marszewski, M.; Kang, J. S.; Pilon, L.; Hu, Y.; Tolbert, S. H. Exploring the Effect of Porous Structure on Thermal Conductivity of Mesoporous SiO_2 Films. *In preparation.*

(32) Zhao, J. J.; Duan, Y. Y.; Wang, X. D.; Wang, B. X. A 3-D Numerical Heat Transfer Model for Silica Aerogels Based on the Porous Secondary Nanoparticle Aggregate Structure. *J. Non. Cryst. Solids* **2012**, *358* (10), 1287–1297.

(33) Zhao, J. J.; Duan, Y. Y.; Wang, X. D.; Wang, B. X. Experimental and Analytical Analyses

of the Thermal Conductivities and High-Temperature Characteristics of Silica Aerogels Based on Microstructures. *J. Phys. D. Appl. Phys.* **2013**, *46* (1).

(34) Sumirat, I.; Ando, Y.; Shimamura, S. Theoretical Consideration of the Effect of Porosity on Thermal Conductivity of Porous Materials. *J. Porous Mater.* **2006**, *13* (3), 439–443.

(35) He, Y. L.; Xie, T. Advances of Thermal Conductivity Models of Nanoscale Silica Aerogel Insulation Material. *Appl. Therm. Eng.* **2015**, *81*, 28–50.

(36) Zhao, J. J.; Duan, Y. Y.; Wang, X. D.; Wang, B. X. Effects of Solid-Gas Coupling and Pore and Particle Microstructures on the Effective Gaseous Thermal Conductivity in Aerogels. *J. Nanoparticle Res.* **2012**, *14* (8).

(37) Baklanov, M. R.; Mogilnikov, K. P.; Polovinkin, V. G.; Dultsev, F. N. Determination of Pore Size Distribution in Thin Films by Ellipsometric Porosimetry. *J. Vac. Sci. Technol. B Microelectron. Nanom. Struct. Process. Meas. Phenom.* **2000**, *18* (3), 1385–1391.

(38) R., H. S. J. Gregg, K. S. W. Sing: Adsorption, Surface Area and Porosity. 2. Auflage, Academic Press, London 1982. 303 Seiten, Preis: $ 49.50. *Berichte der Bunsengesellschaft für Phys. Chemie* **2018**, *86* (10), 957.

(39) Thommes, M.; Kaneko, K.; Neimark, A. V.; Olivier, J. P.; Rodriguez-Reinoso, F.; Rouquerol, J.; Sing, K. S. W. Physisorption of Gases, with Special Reference to the Evaluation of Surface Area and Pore Size Distribution (IUPAC Technical Report). *Pure Appl. Chem.* **2015**, *87* (9–10), 1051–1069.

(40) Kruk, M.; Jaroniec, M.; Ko, C. H.; Ryoo, R. Characterization of the Porous Structure of SBA-15. *Chem. Mater.* **2000**, *12* (7), 1961–1968.

(41) Smarsly, B.; Gibaud, A.; Ruland, W.; Sturmayr, D.; Brinker, C. J. Quantitative SAXS Analysis of Oriented 2D Hexagonal Cylindrical Silica Mesostructures in Thin Films

Obtained from Nonionic Surfactants. *Langmuir* **2005**, *21* (9), 3858–3866.

(42) He, G.; Pan, Q.; Rempel, G. L. Synthesis of Poly(methyl Methacrylate) Nanosize Particles by Differential Microemulsion Polymerization. *Macromol. Rapid Commun.* **2003**, *24* (9), 585–588.

(43) Zou, D.; Ma, S.; Guan, R.; Park, M.; Sun, L.; Aklonis, J. J.; Salovey, R. Model Filled Polymers. V. Synthesis of Crosslinked Monodisperse Polymethacrylate Beads. *J. Polym. Sci. Part A Polym. Chem.* **1992**, *30* (1), 137–144.

(44) Dunphy, D. R.; Sheth, P. H.; Garcia, F. L.; Brinker, C. J. Enlarged Pore Size in Mesoporous Silica Films Templated by Pluronic F127: Use of Poloxamer Mixtures and Increased template/SiO_2 Ratios in Materials Synthesized by Evaporation-Induced Self-Assembly. *Chem. Mater.* **2015**, *27* (1), 75–84.

(45) Ilavsky, J. Nika: Software for Two-Dimensional Data Reduction. *J. Appl. Crystallogr.* **2012**, *45* (2), 324–328.

(46) Li, M.; Kang, J. S.; Hu, Y. Anisotropic Thermal Conductivity Measurement Using a New Asymmetric-Beam Time-Domain Thermoreflectance (AB-TDTR) Method. *Rev. Sci. Instrum.* **2018**, *89* (8), 84901.

(47) Kang, J. S.; Wu, H.; Hu, Y. Thermal Properties and Phonon Spectral Characterization of Synthetic Boron Phosphide for High Thermal Conductivity Applications. *Nano Lett.* **2017**, *17* (12), 7507–7514.

(48) Kang, J. S.; Ke, M.; Hu, Y. Ionic Intercalation in Two-Dimensional van Der Waals Materials: In Situ Characterization and Electrochemical Control of the Anisotropic Thermal Conductivity of Black Phosphorus. *Nano Lett.* **2017**, *17* (3), 1431–1438.

(49) Kang, J. S.; Li, M.; Wu, H.; Nguyen, H.; Hu, Y. Experimental Observation of High Thermal

Conductivity in Boron Arsenide. *Science (80-.).* **2018**, eaat5522.